A TECHNIQUE TO MEASURE TURBULENT FREE CONVECTIVE HEAT TRANSFER IN A VERTICAL TALL CAVITY

by

Mohammad Ebrahim Poulad
B.A.Sc. (Materials Sciences Engineering)
Shiraz University (Iran), 1988

A thesis
presented to Ryerson University
in partial fulfillment of the degree of
Master of Applied Science
In the program of
Mechanical Engineering

Toronto, Ontario, Canada, 2009

I hereby declare that I am the sole author of this thesis.

I authorize Ryerson University to lend this thesis to other institutions or individuals for the purpose of scholarly research.

I further authorize Ryerson University to reproduce this thesis by photocopying or by other means, at the request of other institutions or individuals for the purpose of scholarly research.

BORROWER'S PAGE

Ryerson University requires the signatures of all persons using or photocopying this thesis. Please sign below, and give address and date.

A TECHNIQUE TO MEASURE TURBULENT FREE CONVECTIVE HEAT TRANSFER IN A VERTICAL TALL CAVITY

Mohammad Ebrahim Poulad
Masters of Applied Science
Department of Mechanical & Industrial Engineering
Ryerson University, Toronto, Ontario, Canada, 2009

ABSTRACT

A time-averaging technique was developed to measure the unsteady and turbulent free convection heat transfer in tall vertical enclosure using a Mach-Zehnder interferometer. The method used a digital high speed camera to obtain the time-averaged heat transfer rates.

Optical heat transfer measurements were made in a differentially heated vertical cavity with isothermal walls. The cavity widths (distance between the plates) were L = 12.7, 32.3, 40, and 56.2mm. The corresponding Rayleigh numbers were about $3x10^3$, $5x10^4$, $1x10^5$, $2.7x10^5$, respectively, and the enclosure aspect ratio ranged from A=18 to 76. The test fluid was air and the temperature differential was about 15 K for all the measurements.

Finite fringe interferograms were taken with a high speed camera. Interferograms of the fluctuating temperature field were captured for ten seconds at a frequency of 100Hz. These images were enhanced and processed using MATLAB to measure the local time-averaged heat transfer rate. This time-averaged heat flux was measured at many locations along the vertical cavity walls in order to obtain the spatial average. To validate the proposed technique, the average Nusselt number was compared to measured values and correlations from the literature. In both laminar and turbulent flow conditions, the current measurements compared well with the ElSherbiny correlation.

ACKNOWLEDGEMENTS

I would like to thank Dr. David Naylor for his direction and invaluable advice throughout this project. Without his guidance and technical help, it was impossible to finish this thesis successfully.

I would also like to thank Derek Roeleveld for his help to measure the heat flux in the laminar flow condition in the cavity using the numerical solution of FLUENT software.

I would also like to thank the Solar Buildings Research Network under the Strategic Network Grants Program of the Natural Sciences and Engineering Research Council of Canada for funding this project.

I would like to thank my friends for their support of my studying. Special thanks to Fabio Almeida for his great help during developing the MATLAB codes.

TABLE OF CONTENTS

LIST OF TABLES

LIST OF FIGURES

NOMENCLATURE

A	Aspect ratio (H/L)
H	height of the cavity and plates, (m)
c_p	specific heat of fluid, (J/kgK)
fps	frames per second (Hz)
g	gravitational acceleration, (m/s^2)
Gr	Grashof number
h	convective heat transfer coefficient, (W/m^2K)
k	thermal conductivity, (W/mK)
L	cavity spacing or distance between the plates, (m)
Nu_y	instantaneous local Nusselt number
$\overline{Nu}_y$	local time-averaged Nusselt number, $\frac{1}{t}\int_0^t Nu_{(y,t)}dt$
$\overline{Nu}_{avg}$	spatial average $\overline{Nu}_y$, $\frac{1}{tH}\int_0^H\int_0^t Nu_{(y,t)}\,dtdy$
p	fluid pressure, (Pa)
Pr	Prandtl number
q''_y	instantaneous local heat flux, (W/m^2)
$\overline{q''_y}$	local time-averaged heat flux, (W/m^2), $\frac{1}{t}\int_0^t q_{(y,t)}\,dt$
$\overline{q''_{avg}}$	spatial average of $\overline{q''_y}$, (W/m^2), $\frac{1}{tH}\int_0^H\int_0^t q_{(y,t)}\,dtdy$
Ra	Rayleigh number related to each experiment
Ra_m	mean Ra related to all experiments with the same size (i.e. same L)
SD	standard deviation of heat flux, (W/m^2)
t	time, (s)
T	temperature, (K)
ΔT	temperature difference between cold and hot walls (K)
w	width of the cavity, (m)

x, y, z	Cartesian coordinate system, (m)

Greek Symbols

α	thermal diffusivity, $\alpha = \frac{k_f}{\rho cp}$, ($m^2/s$)
β	thermal expansion coefficient of fluid, (1/K)
λ	laser wavelength, (m)
μ	dynamic viscosity of fluid, (Ns/m^2)
ν	kinematic viscosity of fluid, (m^2/s)
ρ	density of fluid, (kg/m^3)

Subscripts

avg	spatial average
c	cold wall
corr	corrected value
f	film or fluid
h	hot wall
ref	reference
s	plate (wall) surface
y	local height value
∞	ambient

CHAPTER 1: GENERAL REVIEW

1.1 Introduction

Laser interferometry has been applied to measure and visualize the temperature fields for a wide variety of engineering applications. Classical interferometry, using a Mach-Zehnder interferometer (MZI) or similar instruments, and holographic interferometry have been used in most studies so far.

A review of the recent literature (Naylor (2008)) shows that interferometry (both classical and holographic) are currently in wide use in the heat transfer field. In recent years, there has been a renaissance of interest in interferometry, in part because of the rapid developments in computer modeling of heat transfer. Complex numerical models require validation by careful experimentation. In many cases, interferometry is able to provide temperature field visualization and in-depth local heat transfer distributions that are ideal for the verification of numerical predictions.

Interferometry has several features that make it well suited for validation purposes. Compared to other heat transfer measurement techniques, interferometry is non-intrusive, providing measurements with no disturbance of the temperature or flow field. Also, since the measurements are made using laser light, the optically measured temperature is free from thermal inertia. So, real-time measurements can be made of transient phenomena (e.g., turbulent flow).

In the past, interferometry has been mainly applied to laminar steady heat transfer problems using still photography. Each snapshot recorded on a film represents the instantaneous temperature field in the test model. Individual images can be processed to

calculate the convective heat transfer rates (e.g., Nusselt number and convective heat transfer coefficients). Only a few studies have considered turbulent conditions. For example, a study by Lockett and Collins (1986a) investigated turbulent forced convection on a hot plate. They used high speed cinematography (i.e., film) to capture the rapid near-wall temperature fluctuations. Kuehn and Goldstein (1978) used still photography with long exposure times to average the temperature field and to visualize a turbulent free convective flow. Nowadays, with the rapid developments in high speed digital cameras (and image processing software), it should be much easier to perform the time-averaging of interferograms in turbulent flows. Also, with digital imaging, it is much easier to control key parameters, such as frame rate and exposure time.

In the current work, an experimental technique was developed to investigate turbulent free convection heat transfer. This technique combines classical interferometry with a high speed digital camera. This method will be validated using well-accepted experimental data for free convection in a tall cavity, available in the open literature. Hence, the following literature review covers three main topics: i) free convection in tall vertical cavities, with an emphasis on experimental studies, ii) high speed digital cinematography, and iii) digital image processing.

1.2 Literature Review

This thesis employed a high speed digital camera to measure the time-averaged local heat transfer rate in a tall cavity. Digital images, which captured by the camera were automatically processed using a computer program to analyze the interference fringes.

Therefore, in this section the following topics are reviewed: First, the literature related to free convection measurements in vertical cavities is reviewed. Second, some applications of high speed digital cinematography in heat transfer field are discussed. And finally, studies related to digital image processing of interference fringes are reviewed.

1.2.1 Free Convection in a Tall Vertical Cavity

Natural convection and the flow regimes in tall cavities have been thoroughly studied over the last century. Most of the studies of convection in rectangular enclosures can be classified in three main groups: (i) cavities where the flow is due to internal heat generation (e.g., the experiment by Almeida et al. (2008)), (ii) cavities heated from below (e.g. Ganzorolli et al. (1995), Atul et al. (2004), Holland et al. (1975)) and (iii) those heated from the sides. The last group is under consideration in this study, as shown in Figure 1.1. In this configuration, one wall of the enclosure is heated to temperature T_h and other wall is cooled to temperature T_c. The enclosure is of height H, with wall spacing L. The differential heating produces buoyancy driven flow within the enclosure.

Nusselt was the first to study natural convection in a tall, air-filled, vertical cavity in 1909. Since then it has been studied with great interest because of its relative simplicity and great practical importance. Several hundred relevant articles treating different aspects of this problem can be found in the literature, which is proof of its engineering interest. Batchelor (1954) was one of the first to characterize the key parameters that are involved in free convection. He found that the flow conditions can be

described in terms of the average Nusselt number (Nu), Rayleigh number (Ra), Prandtl number (Pr), and aspect ratio (A=H/L).

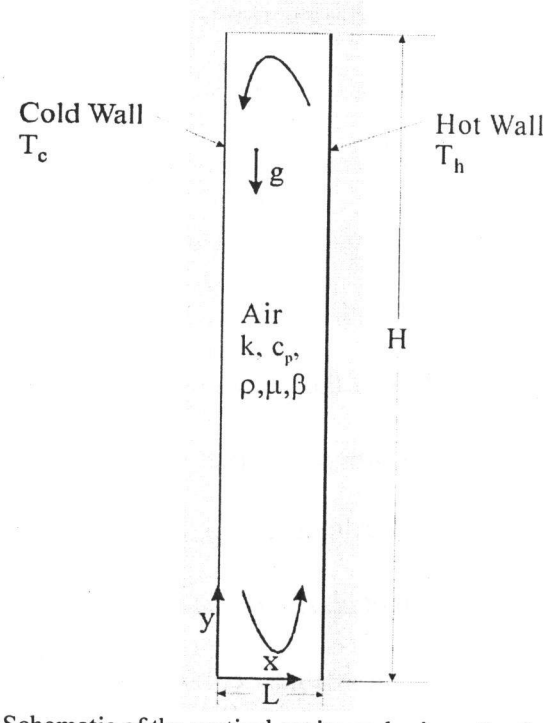

Figure 1.1 Schematic of the vertical cavity under investigation.

The convective heat flux from the hot wall to the cold wall, q'' can be expressed in a dimensionless form as a Nusselt number:

$$Nu = \frac{hL}{k} = \frac{q''L}{k(T_h - T_c)} \tag{1.1}$$

The Nusselt number is a function of the Rayleigh number Ra, the aspect ratio of cavity A, and the Prandtl number Pr of the fluid:

$$Nu = f(Ra, Pr, A) \tag{1.2}$$

where,

$$Ra = \frac{\rho^2 L^3 g C_p \Delta T \beta}{\mu k} = \frac{g \beta \Delta T L^3}{\nu \alpha} \tag{1.3}$$

$$A = H/L \tag{1.4}$$

$$Pr = \mu C_p / k \tag{1.5}$$

where ρ is the fluid density in kg/m^3, g is the acceleration of gravity in m/s^2, C_p is the fluid specific heat in J/kgK, μ is the fluid viscosity in Ns/m^2, ν is kinematic viscosity μ/ρ, k is the fluid thermal conductivity in W/mK, α is thermal diffusivity k/βC_p, and β = $1/T_f$ is the coefficient of thermal expansion in K^{-1}. T_f is mean temperature of the filled fluid (i.e., air) in K.

The natural convective mode of heat transfer is of interested to engineers and is widely applicable in many fields. In the electronics industry, free convection is often used to cool confined components. Electronic components have to be thermally controlled within a specified temperature range to ensure reliable operation. Free convection is also an important mechanism in the passive cooling of nuclear reactors, in the insulation of ship hulls, and in a wide variety of renewable energy applications (Bairi (2008)).

One application of relevance to this thesis is the application to fenestration design. For typical window fill gases (e.g., air, argon, krypton), the Prandtl number does not change appreciably. It has a value of about Pr=0.71. A review of past studies (Wright (1996)) shows that the Nusselt (Nu) is independent of aspect ratio (A) in tall cavities, provided A>20. Therefore, in tall enclosures the Nusselt is only a function of Rayleigh number i.e., $Nu = f(Ra)$.

For an enclosure, the Nusselt number starts at a value of one when the Rayleigh number is zero. This condition is called the conduction regime, which exists even when

the buoyancy driven flow is weak. Convective motion starts as soon as there is a temperature difference ($\Delta T \neq 0$) between the cavity walls. The Nusselt number increases as Rayleigh number increases and the flow strengthens. The experimental results of ElSherbiny (1980) are shown in Figure 1.2. This figure shows that, with increasing Ra, the Nusselt number departs from pure conduction at a Rayleigh number of about 6000. Initially, in the laminar regime, the Nusselt number curve has a slope of about ¼, i.e., $Nu \sim Ra^{1/4}$. In this regime, the flow is unicellular, steady, and laminar. At higher Rayleigh number, a critical value is reached (Ra_c), and the two-dimensional flow becomes multicellular. At higher Ra, the flow becomes increasingly unsteady, chaotic, and eventually fully turbulent. As shown in Figure 1.2, in the turbulent regime, the Nusselt number curve has a slope of about 1/3, i.e. $Nu \sim Ra^{1/3}$. This critical Ra condition has been predicted by numerical simulation (e.g., Lee and Korpela (1983), Korpela et al. (1982)), theoretical analyses (e.g., Bergholz (1978)), and verified by experiments (e.g., Wright et al. (2006)).

For enclosures with high aspect ratio, the Nusselt number depends weakly upon aspect ratio. This can be seen in Figure 1.2. In the range of $5000<Ra<2x10^4$, ElSherbiny's experimental results for A = 80 and A=110 are very similar. This is in agreement with the theory of Raithby et al. (1977) which predicts aspect ratio independency of Nu for high aspect ratio.

As mentioned above, there is a critical Rayleigh for the onset of multicellular flow. Korpela et al. (1982) used the stability analysis of Bergholz (1978) to develop a simple criterion for the critical Grashof number:

$$Gr_c = 8000(1 + 5/A) \tag{1.6}$$

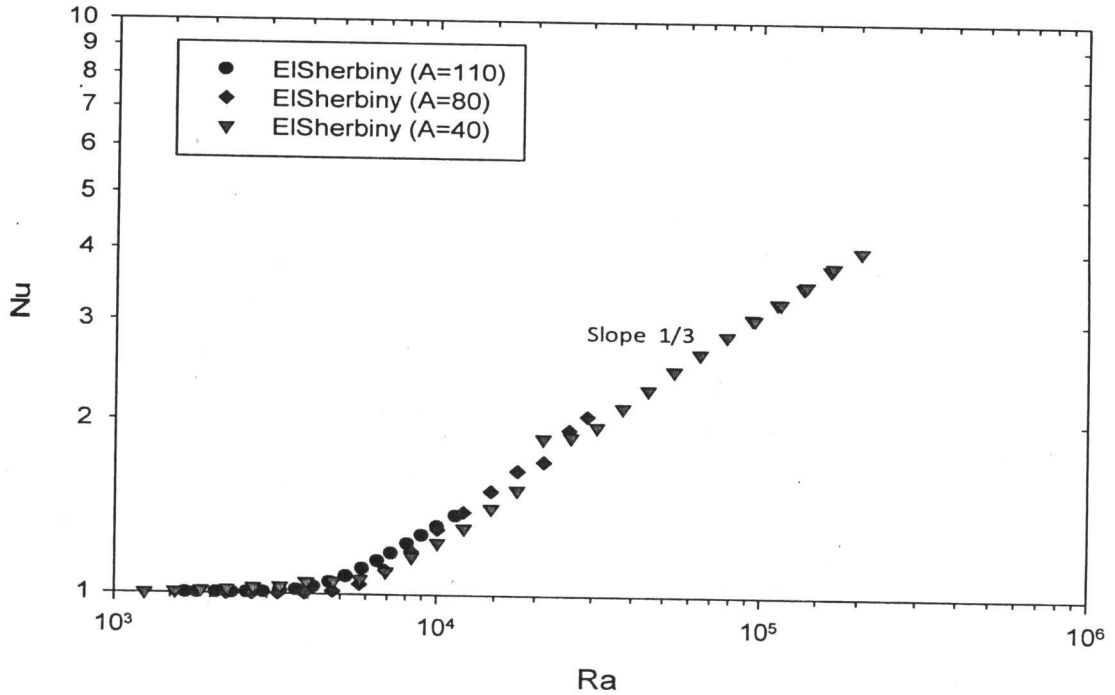

Figure 1.2 Experimental data of ElSherbiny (1980) for free convection in a tall vertical enclosure.

Using Pr=0.71 for gasses, we can express Eq. (1.6) in terms of the Rayleigh number:

$$Ra_c = 5680(1 + 5/A) \tag{1.7}$$

Convective heat transfer in a cavity has been studied extensively, and almost all the features of the flow and heat transfer are now well understood. The flow is driven by buoyancy forces. The fluid flows upward near the high temperature wall and downward near the low temperature wall. At the bottom of the cavity, the cold fluid turns and starts its ascent. Similarly, the hot rising air turns downward at the top of the cavity and circulates around the enclosure.

Wright et al. (2006) studied the free convection of air in a tall vertical cavity with $A \approx 40$ using flow visualization with smoke and interferometry. Also, a Mach-Zehnder interferometer (MZI) was used for visualizing the temperature field. Their observations are summarized in table 1.1. More details can be found in Jin's (2000) thesis. In the conduction regime at low Raleigh numbers (Ra=4,850 to 6,200), Wright et al. (2006) observed the flow pattern to be a single cell. The flow was steady and laminar.

In the range Ra=6,228 to 6,819, secondary flow was observed, in pairs, in the core of the cavity. They are long in the vertical direction and narrow in the horizontal direction, and are sometimes referred to as "cat's eye" cells. They co-rotate with the primary flow and move slowly downward. For Ra = 7,300 to 8,600, the primary flow moved faster and closer to the walls. The secondary flow became stronger. The shape of secondary cells became closer to a wide ellipse or circle. For Ra = 9,600 to 10,500, the primary flow and the secondary flow became unstable. The secondary cells were moving and rotating faster and stronger. The disturbance caused the two cells in a pair of cells to move in opposite directions, toward opposite walls. The flow movement was observed to be slightly three dimensional (3-D). For Ra = 11,600 to 12,600, the cell movements frequently were 3-*D*. The three dimensionality of the flow increases with increasing Rayleigh number. The layer of primary flow close to the walls became thinner. The strongly rotating cells motions often disordered the primary flow. Most cells were moving randomly without any specific direction, although generally the trend was downward. The flow becomes 3-*D* and its magnitude along the width of the plate in the cavity is still small compared to the flow movement in the 2-*D* plane. For Ra = 13,600 to 17,100, the flow became more chaotic and the magnitude of the 3-*D* fluctuations increased with the increase of Rayleigh

number. Randomly moving co-rotating cells are everywhere. The shape and dimension of cells are different from those in the stable secondary flow regime. The scale of the largest cells is as large as the cavity spacing. For Ra = 18,100 to 25,100, the flow inside the cavity was moving faster and more vigorously chaotic and turbulent than before. The flow is totally dominated by the 3-*D* movement of co-rotating cells with different length scales. For Ra = 29,500 to 54,800, the cavity was filled with the turbulent eddies and rotating cells. Compared to those in the secondary flow regime, some cells had a moderate size with high momentum, and dissipated at the smallest scales.

Several empirical correlations have been proposed for free convection in tall enclosures. ElSherbiny (1980) carried out experiments over a wide range of Rayleigh numbers (Ra up to 10^8) and aspect ratios (A = 5, 10, 20, 40, 80 and 110). The wide range of Rayleigh numbers was achieved by changing gas density through the variation of pressure inside the vertical rectangular cavity. Based on experiment results, ElSherbiny (1980) introduced correlations for specific values of A (i.e., A=5, 10, 20, 40, 80 and 110). He also developed a more general design correlation, including the effect of aspect ratio:

$$Nu_1 = 0.0605\, Ra^{1/3} \tag{1.8}$$

$$Nu_2 = \left(1 + \left(\frac{a}{b}\right)^3\right)^{1/3} \text{ where: } a = 0.104 Ra^{0.293} \text{ and } b = 1 + \left(\frac{6310}{Ra}\right)^{1.36} \tag{1.9}$$

$$Nu_3 = 0.242 \left(\frac{Ra}{A}\right)^{0.272} \tag{1.10}$$

$$Nu = max([Nu_1, Nu_2, Nu_3]) \tag{1.11}$$

In this correlation, the average Nusselt number is taken as the maximum of the three expressions, Eq. (1.8)-(1.10). The data from this experiment will be used to verify the present work.

Table 1.1 Flow Pattern Observations of Wright et al. (2006)

Ra	Observation	Comment
4,850 to 6,200	A unicellular flow (the primary flow) exists. This unicellular flow was slow, laminar, and stable. The flow velocity increases as Ra increases. At Ra=6200, the flow was observed to be still stable and unicellular.	Conduction Regime
$6{,}228 \pm 107$ to $6{,}819 \pm 114$	Transition to secondary flow started to appear in the core of the cavity. Eq. (1.7) predicts Ra_c=6376.	Ra_c starts
7,300 to 8,600	The secondary flow became stronger and less stable.	Secondary Flow
9,600 to 10,500	The primary flow and the secondary flow became unstable.	Unstable Flow
11,600 to 12,600	Although the flow has become 3-*D*, the magnitude of flow along the width of the plate in such a narrow cavity is still small compared to the flow movement in the 2-*D* plane.	3-*D* Flow
13,600 to 17,100	The flow became more chaotic and the magnitude of 3-*D* fluctuations increased with the increase of Rayleigh number.	Chaotic-"compound cell"
18,100 to 25,100	The flow inside the cavity was moving faster and more vigorously, 3-*D*, chaotic and turbulent than before.	More Turbulent
29,500 to 54,800	The cavity was filled with the turbulent eddies and rotating cells.	Totally Turbulent

Wright (1996) developed a new correlation for enclosure aspect ratios greater than 40. It was designed specifically for determining the average convective heat transfer coefficient in the center glass region of double-pane windows:

$$Nu = 0.0673838 Ra^{1/3} \quad \text{if } Ra > 5\times10^4 \tag{1.12}$$

$$Nu = 0.028154 Ra^{0.4134} \quad \text{if } 10^4 < Ra \le 5\times10^4 \tag{1.13}$$

$$Nu = 1 + 1.75967\times10^{-10} Ra^{2.2984755} \quad \text{if } Ra \le 10^4 \tag{1.14}$$

Shewen (1986) conducted another experiment employing a Peltier effect technique to measure natural convection heat flux in a rectangular closed cavity with A = 40, 60 and 110. He maintained a wall temperature difference of $\Delta T = 14K$ and averaged 260 measurements taken over a 40 minute period. Figure 1.5 shows a comparison of the experimental data of Shewen and ElSherbiny with the correlation of Wright (1996).

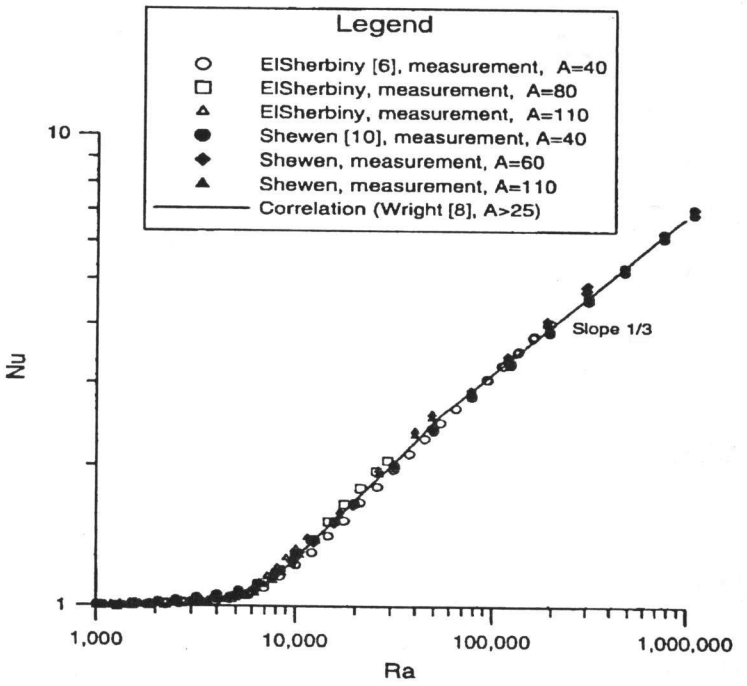

Figure 1.5 Comparison of the average Nusselt number measurements of ElSherbiny (1980) and Shewen (1986) with the correlation of Wright (1996).

Figure 1.6 shows a comparison of the correlations of ElSherbiny (1980) and Wright (1996). A=50 has been used to compute the average Nusselt number in the correlation of ElSherbiny. Wright's correlation is independent of A. As shown in Figure 1.6, Wright's correlation predicts a slightly higher value of Nu than ElSherbiny's design correlation at $Ra \geq 30{,}000$. Before that point, they are in very good agreement.

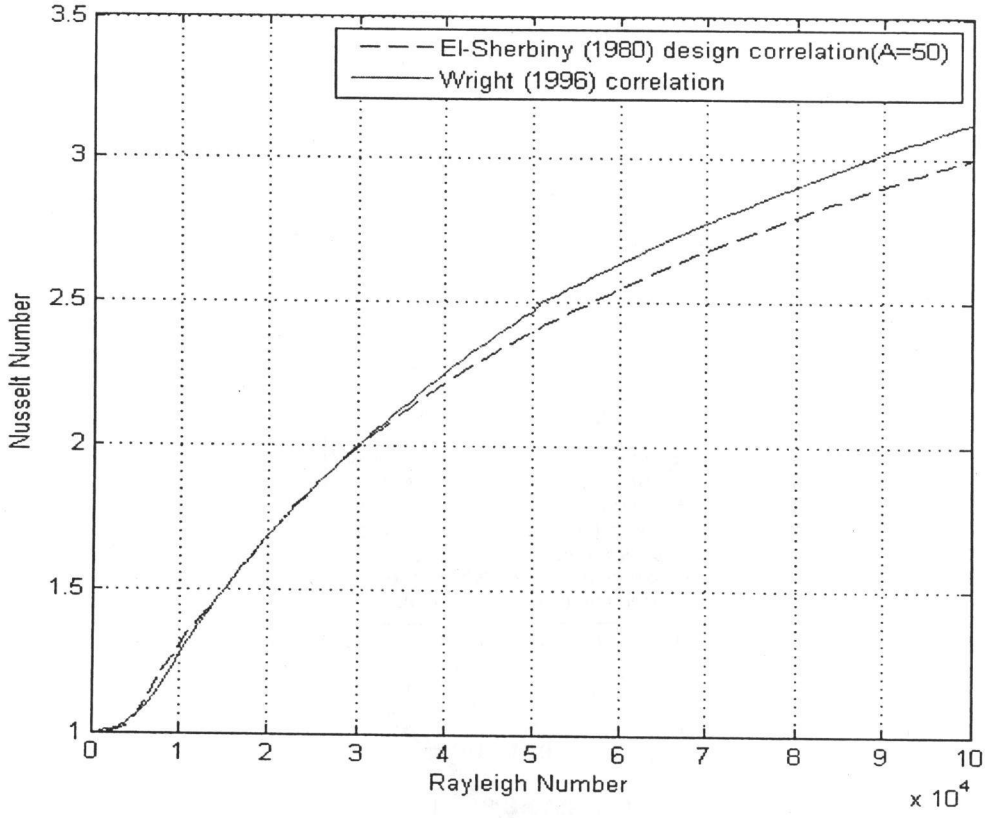

Figure 1.6 Comparison of the ElSherbiny (A=50) and Wright correlations for a tall cavity.

Beam-averaged measurements, when a standard two-dimensional analysis technique is applied, are not exact for a three-dimensional temperature field. Naylor and Machin (2001) performed an analysis to determine the error in the average fluid temperature measurement caused by temperature variations in the light beam direction. The error has been calculated for both an ideal gas and water as the test fluid. The results show that, for typical experimental conditions, the measurement error introduced by this temperature variation is less than 2%, even for the most adverse temperature distribution in the light beam direction. The results of the analysis also suggest that beam-averaged interferometric heat transfer measurements need not be restricted to isothermal surfaces.

For example, average heat transfer measurements could be made on a surface with a conjugate boundary condition, with only a slight reduction in accuracy. Trias et al. (2007) presented two- and three-dimensional direct numerical simulations of a buoyancy-driven flow in a differentially heated air-filled (Pr=0.71) cavity of aspect ratio 4 and Rayleigh numbers up to 10^{10}. It was concluded that two-dimensional simulations may be enough, as a first and cheaper approach, to capture the general features of buoyancy-driven flows in enclosed cavities at Rayleigh numbers up to 10^{10}. However, three-dimensional simulations are necessary for an accurate description of the flow, especially for turbulent statistics.

The above experimental studies are widely quoted in the literature, and represent the most important results for natural convection heat transfer in tall vertical enclosures. The data from these studies will be used in subsequent chapters to validate the new experimental technique developed in the present thesis.

1.2.2 Combination of Interferometry with High Speed Cinematography

Engineers and researchers often want to record, visualize and analyze high speed phenomena such as vibration, dynamic and transient events, e.g., turbulent flow. To get a clear image of a fast changing process, very high speed cinematography is required. For example, a capturing rate of 60,000 Hz has been reported for recording the interferogram of the explosive combustion of butane gas, done by Lockett and Collins (1986b).

In the past, researchers were often confronted with a variety of difficulties, of which some have been overcome in the last few years, thanks to the developments in

digital high speed cameras. The high speed camera was developed in 1929 (Cranz and Schardin (1929)). This type of camera has been used in fluid dynamics, ballistics and fracture mechanics. However, its application in recording dynamic interference fringe patterns started in 1969 (Riley and Dally (1969)). Today, it is extensively used in the automotive sector (Chen et al. (2003)), metrology (Sun et al. (2008), Riley and Dally (1969) and Wright (1975)) and other industrial sectors.

Combining interferometry with high-speed cinematography has expanded the application of interferometry. This combination enables the study of the temperature fields in transient and extremely fast processes, e.g., turbulent flow (Lucic et al. (2004)). For example, Herman et al. (1998) focused on the analysis of unsteady flow features, rather than on temperature measurements that have been thoroughly covered in the literature. They used Bioscan Optimas Version 4.02, a commercially available software environment. Then they used a binary threshold technique: i) to determining the position of the walls and the heated plates in the interferometric image, and ii) to define a suitable coordinate system and the lines corresponding to irradiance extrema. Optimas only keeps a record of two intensity levels (the gray level of the brightest and darkest points along the scan line on the image). Therefore, there is no need to keep the data for the entire image. This data compression allows for easier analysis of the image by eliminating unnecessary details. It also increases processing speed and reduces memory requirements.

To optimize the usage of such cameras, two parameters are to be determined: the frequency rate (frames per second or fps) and total capture time interval. As far as the author has reviewed, those two parameters are sometimes reported. But, none of the studies provide a suitable justification for their selection for a specific application. Table

2.1 introduces a brief review of high speed photography applications using laser as a light source for interferometry or illumination. None of the papers in Table 1.2 provided a well documented justification for the selected values of frame rate. Also, the author of this thesis could not find any work that has been done using the combination of high speed cinematography and interferometry for studying the free convection turbulent heat transfer in the cavity.

Table 1.2 Review of some applications of high speed photography.

fps	Application	Laser Type	reference
1000	Measuring heat transfer around steam bubbles using the holographic interferometer	He-Ne, 35 mW $\lambda = 632.8$ nm	Ju et al. (2000)
10^7	Studying the interaction of a water drop with a supersonic sphere	ruby	Dukhovski et al. (1985)
7000	Measuring the temperature field in combustion chamber using laser shearing interferometry		Liu and Feng (2006)
131580	Observing a test object from various directions	ruby	Kovalev et al. (1983)
250	Studying the effect of buoyancy on the wakes of circular and square cylinders using schlieren interferometry	He-Ne, 35 mW $\lambda = 632.8$ nm	Singh et al. (2007)
1000 to 2000	Comparing three heat transfer enhancement strategies in a grooved channel		Herman and Kang (2001)
1600	Calculating convective turbulent heat transfer on flat plate using holographic interferometry	Argon ion Laser 3 W	Lockett et al. (1985)

1.2.3 Digital Fringe Processing

In interferometry, when the reference beam and test beams recombine, they produce light (constructive) and dark (destructive) regions, which are called *interference fringes*. Images of these fringes are called *interferograms*. Figure 1.7 shows sample interferograms of the temperature field between the hot and cold walls with the interferometer: (a) in the infinite fringe mode and (b) in the finite fringe mode. During

recombination, it is possible to adjust the angle between test beam and the reference beam. If the angle is zero, the fringes are in the infinite mode. Otherwise, the mode is finite. The infinite fringe images are good to visualize the temperature field, as each fringe represents an isotherm. As shown in Figure 1.7 (b), the finite fringes bend upward on the hot wall (right plate on the image) and bend down on the cold wall (left plate on the image). Infinite fringe mode is sensitive to vibrations. This mode is not only easier to set, up but is also more accurate than the infinite fringe mode. Thus, in the present work, the finite fringe mode was used for heat transfer analysis.

To measure the heat flux on each wall of the cavity, the fringe spacing close to the isothermal wall needs to be measured. The accuracy of the heat flux measurement depends highly on the accuracy of fringe spacing measurement. To measure the fringe order as accurately as possible, researchers have used several different methods. Lockett et al. (1985) introduced a technique to analyze the fringes automatically. They used linear regression to reduce the noise of the images. Then the images were analyzed to calculate the Nusselt number on the heated smooth plate. They reported an oscillation frequency of 55Hz in the outer wall fringes when the Reynolds number was about 4670 in forced convective condition. They concluded that single shots and standard video photography are unable to reproduce any continuity of the turbulence.

Hunter and Collins (1987) developed an automatic analysis procedure for fringe analysis using a "Binary Fringe-system" and a "Grey-scale Fringe-system". The ultimate aim of their work was to produce quantitative results from experimental data for comparison with data produced theoretically using large-eddy simulation (LES).

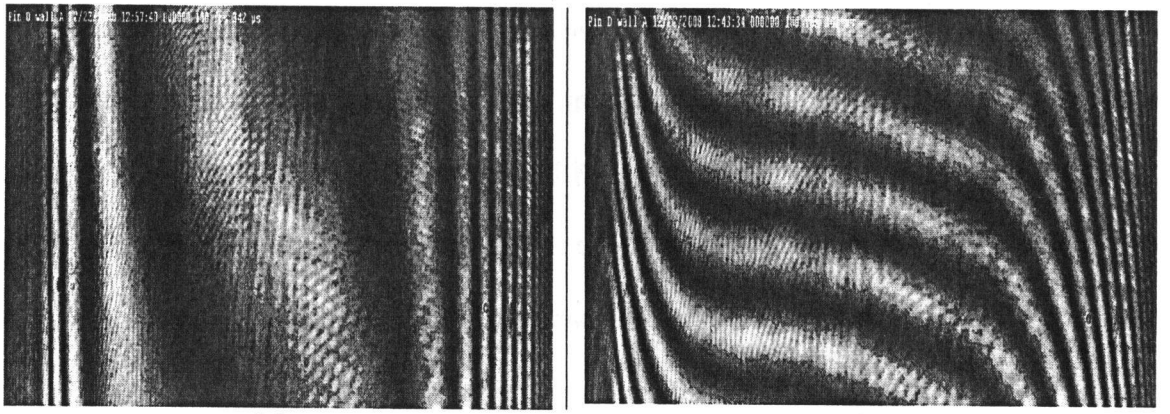

(a) (b)

Figure 1.7 Interferograms of the temperature field between the hot and cold walls, near the centre region of the enclosure in the: (a) infinite fringe mode, and (b) finite fringe mode.

Snyder (1980) developed a fast digital technique. He assumed the interference signal as follows:

$$F(x,\Theta) = (I_\Theta + \alpha x)[1 + \cos(x + \Theta)] \tag{1.15}$$

where x may be either a space or a time coordinate, Θ is the phase of the fringe pattern at the origin, I_Θ is amplitude of the fringe pattern, and α is the slope of the envelope. To check the uncertainty of the proposed equation, he analyzed the computer generated fringes.

Schemm and Vest (1983) reported a method that uses all information available in the irradiance measurements to smooth and interpolate the phase of the fringe accurately. They used nonlinear regression analysis to fit a function I(x) to the full irradiance field using least squares error criteria. The following function was used:

$$I(x) = B(x) + E(x)\cos\,[P(x)] \tag{1.16}$$

where B(x), E(x) and P(x) are low-order polynomials.

Another digital fringe analysis method was presented by Slepicka and Cha (1995). They defined a function, I(x), for the intensity of digitized interferogram as follows:

$$I(x) = B(x) + A(x)\cos\,[P(x)] \tag{1.17}$$

where B(x), A(x), and P(x) represented background intensity, modulation amplitude, and modulation phase, respectively. Then a nonlinear regression technique was used to approximate the variation of measured values with the proposed model. The algebraic model (Eq. 1.17) is nonlinear with respect to the parameters that must be found for the best fit (i.e., B(x), A(x), and P(x)). To find the parameters, an iterative independent estimation of each parameter was used. They concluded that this regression demonstrates good accuracy and stable convergence even for the cases with few fringes and high noise level. This technique, with slight modifications, was used in the present work to analyze the digital fringes on the interferogram.

Some authors (e.g., Nugent (1985), and Yatagai et al. (1982)) introduced techniques for fitting two dimensional fringe patterns. This technique is beyond the scope of this thesis.

During the measurement of turbulent heat transfer in a channel, Liou et al. (1993) found that the time-averaged analysis of the temperature profile, calculated from 50 instantaneous interferograms, provided better accuracy than a single instantaneous interferogram. The temperature profile calculated by this time-averaged technique was about 6% different than the numerical results, calculated using the k- ε-A PDM (preferential dissipation modification) model. In comparison, the instantaneous temperature profile measured by holographic interferometry revealed a deviation as high as 25%. This was the motivation for the researchers to use a time-averaged technique. It enabled a more accurate measurement of free convection turbulent heat transfer.

Statistically, the more the number of samples, the closer the time-averaged value will be to the actual value. On the other hand, the number of samples must be finite,

because of time and memory limitations. Also, at some point, other sources of error will become dominant. A time-averaged technique was used in the present work. The strategy used to select the number of images for analysis will be discussed in Chapter 3.

1.2.4 Summary of Literature Review

The time-averaging technique has been recently used to measure turbulent convection heat transfer. Still photography and standard video-based cinematography are not used any longer for these types of measurements. Comprehensive research has been done to study convective heat transfer in tall cavities. Amongst them, some researchers have reported a few anomalous results in their heat transfer measurements (e.g., Almeida et al., 2008). A closer look at these data shows the problem may be related to turbulent flow conditions. Perhaps, if time averaged heat transfer measurements had been made, instead of analyzing snapshots, they would have not faced such irregularities. Studying the temperature field in turbulent flow needs an instrument that can take pictures of the test model as fast as the flow changes with time. To the best of the author's knowledge, a time-averaged technique has not yet been used to measure turbulent convection heat transfer in a vertical cavity.

1.3 Scope of the Current Thesis

The main object of the present thesis is to develop a time-averaging interferometric technique to measure turbulent free convective heat transfer. Measurements will be made in a tall vertical cavity heated and cooled from the sides. A combination of high speed digital cinematography and laser interferometry will be used to measure the instantaneous temperature field. The instantaneous interference patterns will be analyzed using automated digital image processing to obtain the instantaneous and time averaged local heat flux. This will require the development of several custom programs, using the MATLAB Image Processing Toolbox. The effect of various experimental parameters on the accuracy of the measurements, such as the frame capture rate and the total exposure time, will be examined. Results will be presented for both laminar and turbulent flow conditions. Comparisons will be made with published heat transfer results for free convection in a tall vertical cavity, which are available in the open literature. Although a tall vertical cavity will be used for this study, this new technique is expected to be useful for many other heat transfer geometries.

CHAPTER 2: EXPERIMENTAL APPARATUS

2.1 Introduction

Many optical techniques have been used in the measurement of temperature. Among them the "index of refraction method" is used frequently in heat transfer. In this way, the index of refraction or the spatial derivative of index of refraction is measured using an interferogram. The reader is referred to the literature (Naylor and Duarte (1999), Goldstein (1970), Naylor (2003) and Naylor (2008)) for an in-depth explanation and mathematical description of interferometry and holography.

A Mach-Zehnder interferometer (MZI), as shown in Figure 2.1, was used in the current experiment to obtain interferograms. It was constructed by Dr. Naylor at Ryerson University in 1994, based on Tarasuk's design (Tarasuk (1968)). The MZI has some advantages and disadvantages. The main advantages of the MZI are as follows:

- high quality and accurate interference because of large displacement of the test beam from the reference beam
- full field temperature measurement that is non-intrusive
- real time measurement and temperature field visualization (no thermal inertia)

Some limitations of the MZI are:

- expensive and delicate optics require proper set up and careful handling
- working environment must be clean and low vibration
- test fluid has to be transparent to laser light

- difficult to measure turbulent flow temperature field, because of spatial averaging of temperature along the laser beam path

In the present work, a high speed camera was used to measure the time-averaged temperature field of free convection in a tall vertical enclosure. This approach gives better accuracy when applying interferometry to turbulent flows, compared to the conventional method (using snapshots to measure the temperature field).

Experiments were done with various frame rates, using the high speed digital camera. The results (to be presented later in this thesis) show that a frame rate of 100 Hz (fps) gives acceptable accuracy. Also, the total capture time required to obtain a stationary time-averaged heat flux measurement was found to be ten seconds.

This chapter describes the interferometer, the experimental model, the high speed camera setup and other associated instrumentation. The associated instrumentation includes the barometer, and different temperature measurement equipment.

2.2 Interferometer

Figure 2.1 shows the plan view of the Mach-Zehnder Interferometer (MZI), which was used in this research. It was set up on an optical bench (364 kg) manufactured by Newport Corporation with ¼-20 NC tapped holes spaced equally center-to-center of 1" (25.4 mm). The various optics and laser were mounted to these holes. The bench (size of about 1.3mx3.0m) rested on eight air bags, equally spaced beneath the table, to reduce the transmission of external vibrations. A Helium-Neon laser (10 mW He-Ne laser with wavelength of $\lambda = 6.328 \times 10^{-7}$ m), equipped with spatial filter and beam expander, was

used as the source of monochromatic light to produce the interferograms. The expanded and collimated beam was separated into two equal beams after passing the beam splitter (item #3 in Fig. 2.1). These beams have the same phase because they are produced from same origin. One beam passes through ambient air while the other beam passes through the experimental model (cavity). The temperature of the experimental domain, which is different from ambient, changes the air density. This causes a change in the index of refraction. The change of index of refraction relative to the ambient beam creates a phase shift. This phase shift appears as constructive and destruction fringes when the two beams recombine at the second beam splitter (item #6 in Fig. 2.1). For the MZI shown in Figure 2.1, the final recombined beam is focused in order to be photographed by the digital camera (item #9), usually at a 100 frame rate. The output, which is called an *interferogram*, was captured digitally. To overcome the relatively low resolution of the high speed camera, the camera was focused on a small area in the near-wall region of the model, with dimensions 15mm x 20mm. The images from this small "window" were transferred for image processing to obtain the time-dependent local heat transfer rate. The distance between the small mirror (item #8) and camera sensor was adjusted from 46 cm to 66 cm. This distance was adjusted in order to get sufficient resolution to measure fine fringes, while still having reasonable image intensity.

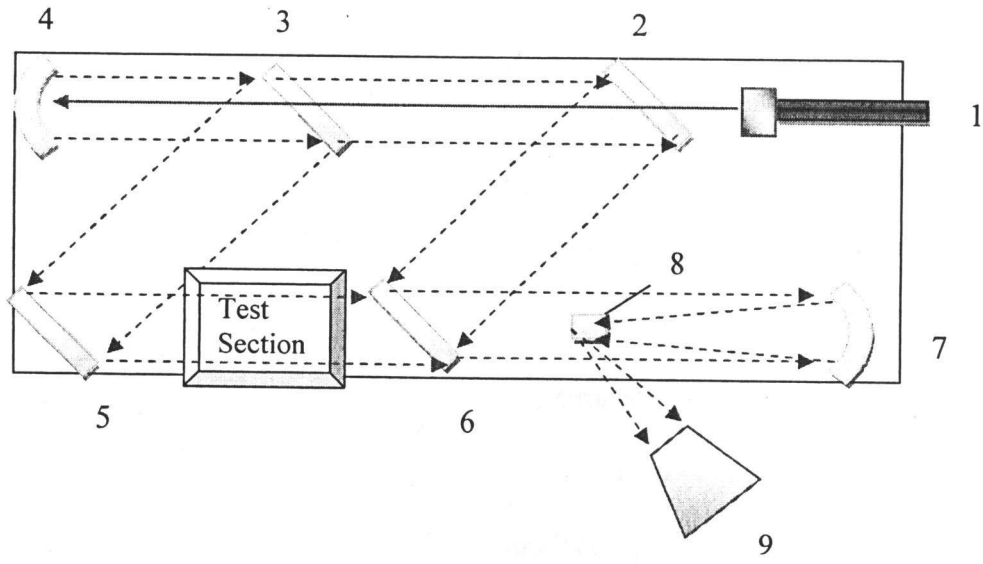

Figure 2.1 Plan view of a Mach-Zehnder interferometer consisting of: 1. He-Ne laser (10mW, λ=632.8nm), 2&5. First surface mirror (flatness $\lambda/10$), 3&6. Beam splitter (50/50, parallelism 1 arc second, flatness $\lambda/10$), 4. Parabolic mirror (fl 64"), 7. Spherical mirror (fl 24"), 8. Small flat mirror (9x9 mm^2), 9. High speed digital camera

2.3 High Speed Camera

The high speed camera (model: MotionPro X3) was made by Integrated Design Inc., USA. Figure 2.2 shows a photograph of the camera. To get the maximum possible intensity, the lens was removed from camera and images were exposed directly on the camera sensors. In this way, in a single session the camera was able to capture a maximum area of approximately Δy = 20 mm by Δx = 18 mm on the experimental model. To view the entire model, the camera's "window" was moved within the interferometer beam.

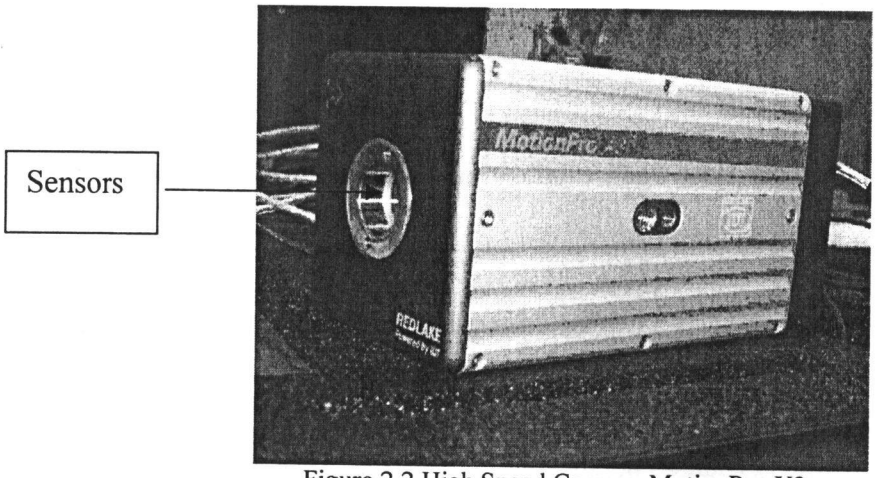

Figure 2.2 High Speed Camera, MotionPro X3.

The single exposure was used to capture the images, as shown in Figure 2.3. Exposure and data readout are performed in parallel. The frame rate may be configured in the software. The sensor works continuously and the camera may capture the next image while it is still reading out the previous frame. For a given vertical region of interest (ROI), the configured period T (the reciprocal of frames per second or fps) cannot be smaller than the read out time (Tro).

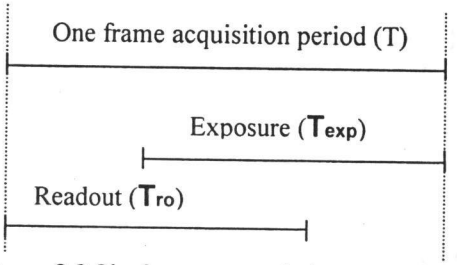

Figure 2.3 Single exposure timings.

The formula to compute readout is given by camera manufacturer as:

$$Tro = 2 \times Tdel + Trcc \times (Nrows + Ner) / Fclk \quad (2.1)$$

where:

Fclk (Internal clock): is the camera's/sensor's internal operating clock. For the current camera F_{clk} = 90.00 MHz

Ner (Extra rows): is the read out time that includes the reading of some extra rows. For the current camera **Ner = 1**

Trcc (Row Clocks Count): is the number of internal clock cycles that the sensor needs to read one row of data. For the current camera **Trcc = 84**

Tdel (Delay clocks): is the delay (pause) between read outs. The delay (in nanoseconds) depends on the internal clock frequency and may be easily computed. For the current camera

Tdel [ns] = 8 x 1,000,000,000 / Fclk = 88.9 ~ 89 ns

The relationship between period, read out and exposure are as followings:

Acquisition period T: **T > Tro**

Exposure Time Texp: **0 < Texp < T**

The maximum frame rate (fps) is achieved when the period is equal to the read out time and the exposure is equal or lower than the read out time (see Figure 2.3). The maximum frame rate at full resolution for current camera is shown in the table below.

Table 2.1 The camera specifications (MotionPro X3).

Sensor array	Pixel size	Memory	Lens Mount	Max. Rate (fps)	Image Bit Depth
1280x1024	12 µm	4 GB	C and F	1040	8 Bit Mono

Putting the current camera values into Equation (2.1), Equation 2.2 can be derived specifically for this camera:

$$T_{ro} = 0.178 + 0.93(N_{rwos} + 1) \quad (2.2)$$

Recalling fps = 1/T, the maximum frame rate can be calculated. The real maximum frame rate is slightly lower than the value computed with the formula above. Table 2.2 shows the maximum frame rate calculated using Equation 2.2 for different values of N_{rows}. For the maximum size of image (N_{rows} = 1024), the maximum rate would be 1049, which is the specification of the camera as mentioned in the above table. Clearly, to get the highest frame rate, it is advisable to use the lowest possible of number of rows (i.e., smallest image). This also allows for a longer total capture time, since the memory required for each image is lower. The full image resolution is 1280x1024. This corresponds to a file size at each time step of approximately 1.3 Mb. Since the on-board RAM is 4GB, the number of full size images that can be taken is $4x10^9/1310720 = 3052$.

Table 2.2 Relationship between number of rows in the image and the maximum frequency (fps).

N_{rows}	T_{ro} in µs	Max fps
10	10	95744
15	15	66176
20	20	50562
25	24	40909
30	29	34351
35	34	29605
40	38	26012
50	48	20930
100	94	10588
150	141	7087
200	188	5325
250	234	4265
300	281	3557
350	328	3051
400	374	2671
450	421	2375
1000	934	1070
1024	957	1045

The camera's RAM (i.e., 4 GB) controls the maximum interval of capturing images. In the other words, the number of images is equal to the time interval in seconds multiplied by the frame rate in fps. Another limitation for having the maximum fps is the exposure time. As Figure 2.3 implies, exposure time cannot be greater than the period (T = 1/fps). Maximum fps means minimum period, which limits the exposure time. Therefore, the higher capture rates required more light intensity in order for the camera sensor to give an acceptable image (see Fig. 2.2).

2.4 Vertical Isothermal Plate Enclosure

The enclosure used in the present experiments was assembled by Almeida (2008) at the Ryerson Thermofluids Research lab during the summer. It consisted of two aluminum alloy plates. Each plate had a height of 994mm, a width of 540mm, and a thickness of 19mm. On each plate some locating pins were mounted, as shown in Fig. 2.4. These pins were used to locate the elevation (y) of the captured image. Also, these pins were used to align the interferometer's test beam to the enclosure.

There is a tradeoff between the width of the plate (in the light beam direction) and refraction errors. Smaller model widths produce a lower number of fringes. However, if the plate width is too small, then end effects (e.g. three dimensional flows) can become important. If the plate width is too large, then refraction errors can be significant. The selected width (W=547 mm) gives 11.7 fringes (or 1.3 °K per fringes) across the cavity for a wall-to-wall temperature difference of $\Delta T = 15°K$. Seven millimeters were added to

the width plate (540 mm) because of the sealing layers that are added to the both sides of the plates.

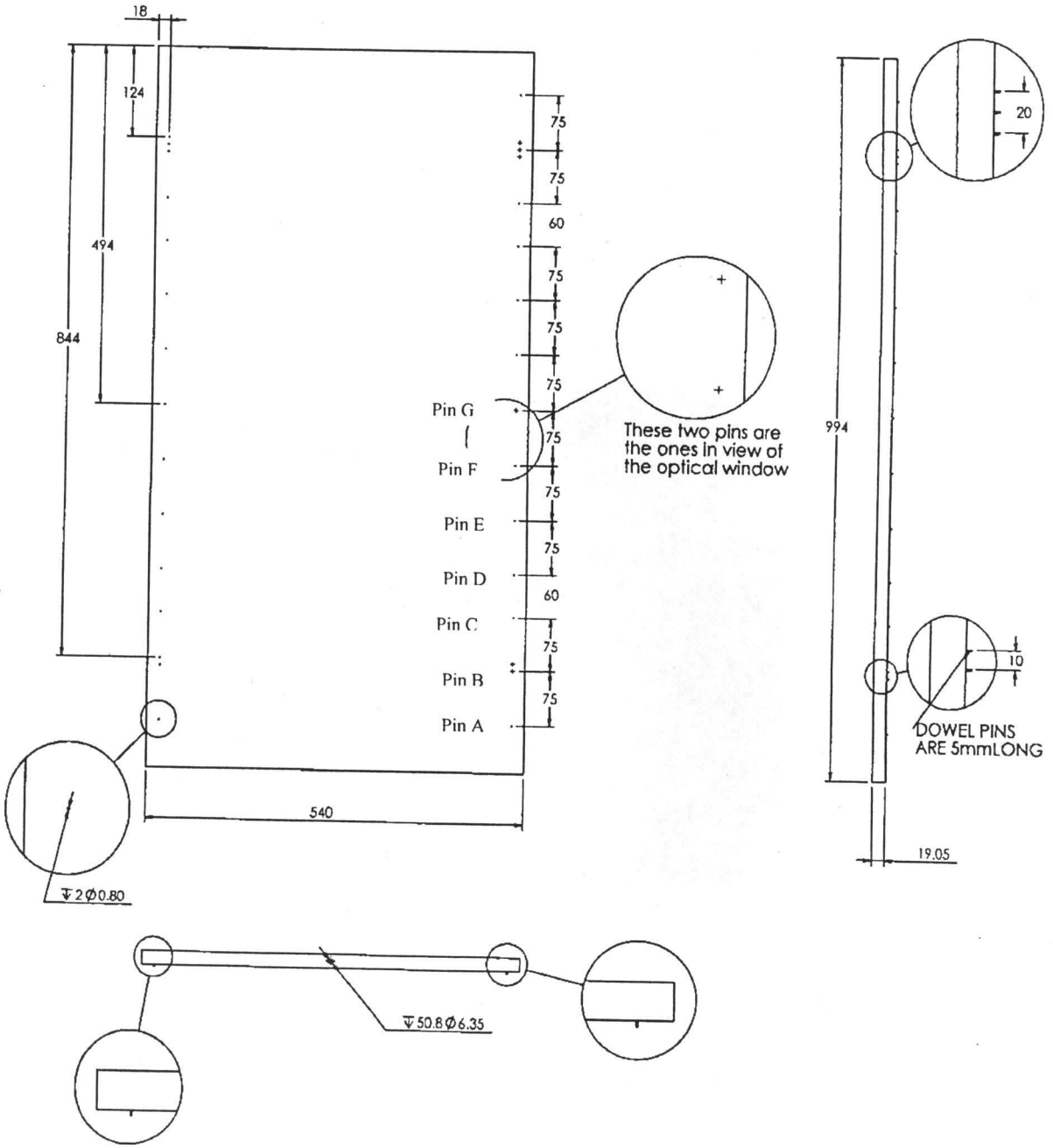

Figure 2.4 Plate drawings with the locating pins on it. All dimensions are in millimeters.

As shown in Fig. 2.5, the entire structure was placed on a movable scissors jack to allow vertical translation of the assembly. The apparatus was lifted to allow optical access to the desired y location. (The y is shown in Fig. 1.1. Measurements were made in the bottom half of the enclosure over the interval $0 \leq y \leq H/2$). To stabilize the experimental model, the entire structure (lifter and assembled enclosure) was supported by four legs. Legs were also used to level the enclosure, by adjusting the height of the screws. To make the legs turn more easily, there were Teflon pieces between floor and leveling screws.

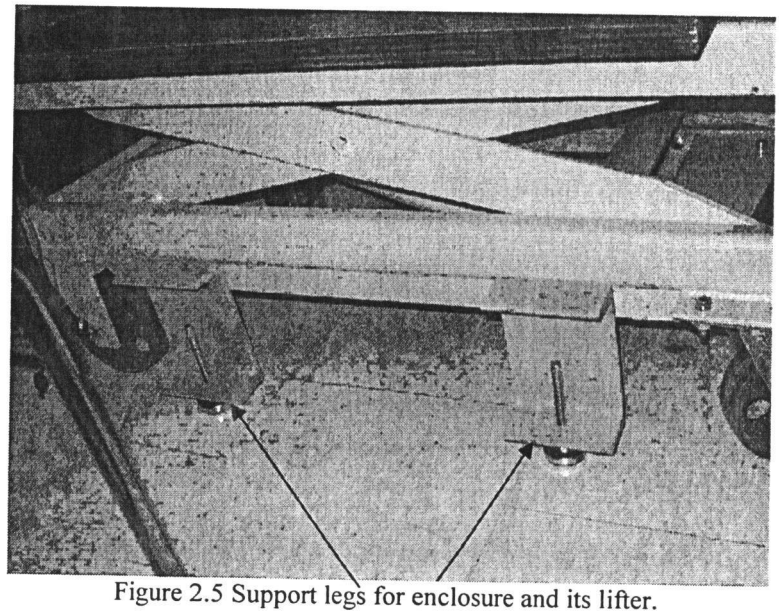

Figure 2.5 Support legs for enclosure and its lifter.

Reference can be made to Sections 2.4 and 2.5 of the Master's thesis by Almeida (2008) for details about the enclosure assembly. These details will not be reproduced here.

2.5 Barometer

The absolute room pressure was measured by a mercury barometer with a measurement resolution of 0.1 mmHg. The pressure reading (P) was corrected for two factors: (i) the change in local gravitational acceleration with global latitude, based on the location of Toronto and (ii) thermal expansion of mercury, based on the room temperature. The MATLAB routine for the pressure correction (Pressure.m) is given in Appendix A. The corrected pressure (P_{corr}) was used in all further heat transfer calculations.

2.6. Length Calibrator

In order to relate the number of pixels between fringes to actual fringe spacing, a length calibrator was needed. This calibrator was made by using two steel pins. The two pins were inserted (and fixed by epoxy) into a small stand, as shown in Figure 2.6. The distance between the tips of the pins was measured using optical microscope with an x-y travelling stage. The micrometers on the stage had a resolution of one micron. The distance between the tips of the pins was measured to be 0.006935 m. This value was used later on to calculate the scale factor of the captured images (in m/pixel).

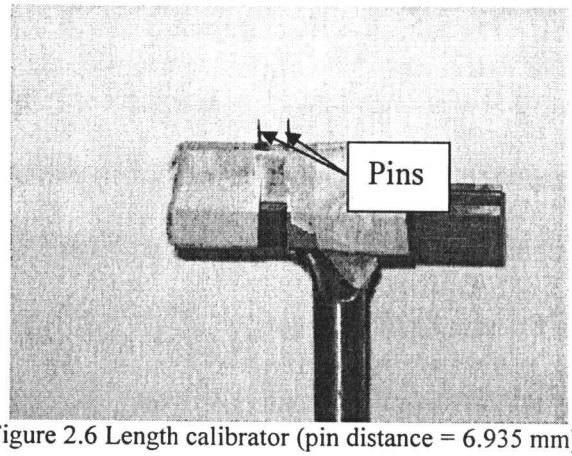

Figure 2.6 Length calibrator (pin distance = 6.935 mm).

2.7 Temperature Measurements

Temperatures were measured with three different types of instruments: i) A high accuracy platinum resistance thermometer was used to measure the temperature difference between hot and cold walls, ii) Copper-constantan thermocouples were used to measure the uniformity of the aluminum plates (walls), and iii) A glass calibration thermometer was used to measure the room temperature.

2.7.1 Digital Platinum Resistance Thermometer

Two Platinum resistance thermometers were operated in differential mode to provide an accurate $\Delta T=T_H-T_C$. It should be noted that the plate temperatures measured by the Platinum resistance thermometers differed from the nominal readings on the constant temperature baths. The temperature of the constant temperature bath was iteratively adjusted until the desired plate-to-plate temperature difference was achieved within ±0.02 K. With the apparatus and optics prepared, the model was heated to the

desired temperature setting. Care was taken to bring the plate to the desired temperature due to the high thermal mass of the plates. Once steady state was reached (approximately 35 minutes), all parameters from the data acquisition system, constant temperature baths, and ambient air properties were recorded. The temperatures of cold and hot walls were measured using the Platinum resistance thermometer, which has a resolution of 0.01 K. The platinum resistance thermometer is shown in Fig. 2.7.

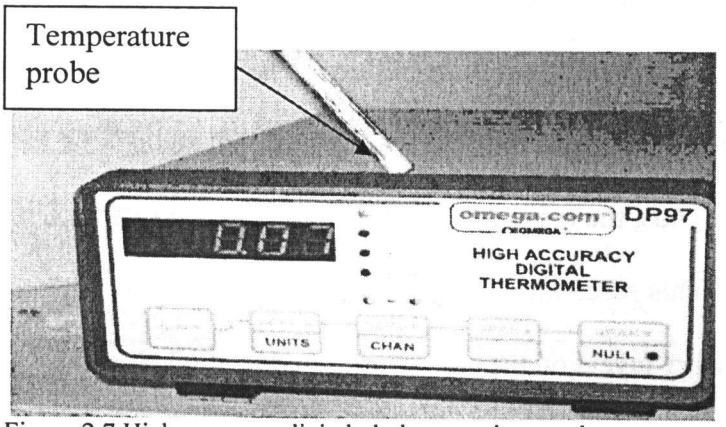

Figure 2.7 High accuracy digital platinum resistance thermometer.

2.7.2 Thermocouples

Copper-Constantan thermocouples were used to check the temperature uniformity of the hot and cold plates. The thermocouples were made with 24 gauge wire (AWG = 24) using a Type T connector. The thermocouples were calibrated with a constant temperature bath using a high precision glass calibration thermometer. They were placed in nine holes (almost equally spaced) on the back of each plate to record the local temperature of the plates. The largest deviation in temperature along the plate was found to be within 0.85°K.

2.7.3 Glass Thermometer

The ambient air temperature was recorded using the high precision glass calibration thermometer. The measurement resolution was 0.1 K. This thermometer was used as calibrator for calibrating the thermocouples and for checking the heat bath temperature readers. However, ambient temperature was not required for the heat transfer calculations. The main reason for recording the value of the ambient temperature was to establish the desired hot and cold wall temperatures. The hot wall was heated about 7.5K above the ambient temperature and the cold wall was cooled about 7.5K below the ambient temperature. Thus, the mean temperature of the optical windows was close to the ambient temperature. This precaution reduces the optical error caused by the formation of free convective boundary layers on the outside of the optical windows.

CHAPTER 3: EXPERIMENTAL PROCEDURE AND COMPUTER CODES

3.1 Introduction

In this chapter, the theory used to process the interferograms for calculating the convective heat transfer rates are described. Also, the experimental procedure, and the image processing algorithm are described. The effects of different median-filtering and nonlinear regression on the final results, along with image capturing parameters (i.e., frame rate and capturing interval), are also discussed.

3.2 Interferograms

Referring to description of the MZI in Section 2.2., the destructive/constructive interference pattern of the interferogram is created when the reference beam and test beam recombine at the second beam splitter. In the infinite fringe mode, the two beams are parallel when they recombine. When the two beams are purposely misaligned by adjusting the micrometer on the second beam splitter, the interferometer is in the finite fringe mode. In this mode, the fringe pattern was adjusted to be a series of horizontal lines when the plates were at room temperature. Infinite fringe mode was not ideal for temperature measurement purposes because:

- the fringes are more sensitive to vibrations and it is difficult to get measurements in low temperature gradient regions.

- it is harder to set up than the finite fringe mode.

Thus, in this thesis, the finite fringe mode was always used for analysis purposes.

3.3 Interferogram Analysis

When a laser (monochromatic electromagnetic wave) propagates in the z direction, its amplitude can be represented at any time, t, as:

$$A = A_0 sin\left(\frac{2\pi ct}{\lambda}\right) \tag{3.1}$$

where A_0 is the maximum amplitude, c the speed of light and λ the wavelength. The beam splitter separates the laser into two beams with equal intensity. One half is the reference beam that recombines with the other half (test beam), which passes through the test model. When the light beam is separated (as reference beam and test beam) and then recombines, the total amplitude (A_t) can be expressed as (Naylor (2008)):

$$A_t = A_0\left(sin\left(\frac{2\pi ct}{\lambda}\right) + sin\left(\frac{2\pi ct}{\lambda} - \theta\right)\right) = 2A_0 sin\left(\frac{2\pi ct}{\lambda} - \frac{\theta}{2}\right)\cos\left(\frac{\theta}{2}\right) \tag{3.2}$$

where θ is the phase shift between the two waves, caused by the change in refractive index of the fluid in the test model. So, if the cosine argument ($\theta/2$) is an integer product of π (i.e., θ is an integer product of 2π), the condition is called constructive, and a bright area is seen on the interferogram image. This bright line is called a constructive fringe. If θ is an odd product of π, the condition would be destructive ($A_t = 0$), and a dark area is seen on the image. This dark line is called a destructive fringe (see Fig. 3.8). The phase shift between the reference and test beams is related to the difference in the number of waves in the two beams, and is related to fringe shift order, ε, as follows:

$$\varepsilon = \frac{\theta}{2\pi} = \int_{ref} \frac{dz}{\lambda} - \int_{test} \frac{dz}{\lambda} \tag{3.3}$$

The refractive index (n) of a medium is defined as the ratio of the speed of light in a vacuum (c_0) to the speed of light in the medium (c):

$$n = c_0/c = f\lambda_0/f\lambda = \lambda_0/\lambda \tag{3.4}$$

where f_0 and λ_0 are the frequency and wavelength of light in a vacuum, respectively. Substituting λ from above equation into Eq. (3.3) gives:

$$\varepsilon = \frac{1}{\lambda_0}\left[\int_{ref} ndz - \int_{test} ndz\right] = \frac{1}{\lambda_0}\int_0^w (n_{ref} - n)dz \tag{3.5}$$

where w is the length of the test model in the light beam direction. So, fringe shift order also can be defined as optical path difference between the test and the reference beam, divided by vacuum wavelength. The refractive index of air at room temperature (reference), n_{ref}, is constant, but the refractive index of the fluid in the model is a function of position and time, n(x,y, z,t). Neglecting refraction effects, and assuming that the test fluid is an ideal gas, the Gladstone-Dale equation is applicable (Goldstein (1970)):

$$n = 1 + \rho G = 1 + \frac{PG}{RT} \tag{3.6}$$

As a result, the instantaneous fringe shift, $\varepsilon(x,y,t)$, is related to the temperature field, T(x,y,z,t), as follows:

$$\varepsilon(x,y,t) = \frac{1}{\lambda_o}\int_0^w [n_{ref} - n(x,y,z,t)]dz = \frac{PG}{R\lambda_o}\int_0^w \left(\frac{1}{T_{ref}} - \frac{1}{T(x,y,z,t)}\right)dz \tag{3.7}$$

where P is the absolute pressure, G is the Gladstone-Dale constant, R is the gas constant, and λ_o is the vacuum wavelength of the laser light source. Rather than using the ambient temperature, it is usually more convenient to measure the fringe shift order relative to a surface with a known temperature, T_{ref}. In practice, T_{ref} can be taken as either the hot or

cold wall temperature. By definition, in Eq. (3.7) a positive fringe shift is in the direction of increasing fluid temperature.

The beam-averaged temperature gradient normal to the measurement surface is needed to calculate the local convective heat flux. This can be obtained by differentiating Eq.(3.7) with respect to x, to give:

$$\frac{\partial \varepsilon}{\partial x} = \frac{\partial}{\partial x}\left\{\frac{PG}{R\lambda_o}\int_0^w \left(\frac{1}{T_{ref}} - \frac{1}{T}\right) dz\right\} = \frac{PG}{R\lambda_o}\int_0^w \frac{\partial}{\partial x}\left(\frac{1}{T_{ref}} - \frac{1}{T}\right) dz$$

$$= \frac{PG}{R\lambda_o}\int_0^w \left(0 - \frac{\partial}{\partial x}T^{-1}\right) dz = \frac{PG}{R\lambda_o}\int_0^w \frac{1}{T^2}\frac{\partial T}{\partial x} dz \qquad (3.8)$$

Applying Eq. (3.8) at the surface:

$$\left.\frac{\partial \varepsilon}{\partial x}\right|_{x=0} = \frac{PG}{R\lambda_o}\int_0^w \left.\frac{1}{T_s^2}\frac{\partial T}{\partial x}\right|_{x=0} dz \qquad (3.9)$$

where T_s is temperature distribution along the measurement surface in the light beam direction (z). For measurements on an isothermal surface (as in the present experiment), the surface temperature is a constant, and Eq. (3.9) can be solved for the beam-averaged surface temperature gradient:

$$\frac{1}{w}\int_0^w \left.\frac{\partial T}{\partial x}\right|_{x=0} dz = \frac{R\lambda_o T_s^2}{wPG}\left.\frac{\partial \varepsilon}{\partial x}\right|_{x=0} \qquad (3.10)$$

Because of the no slip and impermeability conditions at the surface, the heat transfer at x=0 occurs by pure conduction. So, the instantaneous local convective heat flux from the surface at any y-location can be expressed as:

$$q_y'' = -k_s \left.\overline{\frac{\partial T}{\partial x}}\right|_{x=0} = -\frac{k_s}{w}\int_0^w \left.\frac{\partial T}{\partial x}\right|_{x=0} dz = -\frac{k_s R \lambda_o T_s^2}{wPG}\left.\frac{\partial \varepsilon}{\partial x}\right|_{x=0} \qquad (3.11)$$

where k_s is the fluid thermal conductivity, evaluated at the surface temperature. Eq. (3.11) has been used to evaluate the instantaneous local heat flux at each time step, using the surface fringe shift gradient measured in each interferogram. The surface fringe

gradient normal to the measurement surface is obtained using an automated image processing method, which is described in Section 3.3. The temperature increases from the cold wall to the hot wall cold wall, so $\frac{\partial T}{\partial x}\Big|_{x=0}$ is greater than zero on the cold wall. Algebraically, the heat transfer rate and Nusselt number are negative on the cold wall and positive on the hot wall. In this thesis, absolute values of heat transfer rate and Nusselt number are reported unless otherwise specified.

Measurements made using Eq. (3.11) will be referred to as instantaneous "local" values, even though they are beam-averaged. In a three dimensional turbulent flow, the laser averages the variations of convective heat transfer in the beam direction. So, the heat flux expressed by Eq. (3.11) is local with respect to the y-coordinate, but beam-averaged in the z-direction.

In an unsteady or turbulent flow, the instantaneous heat flux values can be time-averaged as follows:

$$\overline{q_y^{"}} = \frac{1}{t}\int_0^t q_y^{"}\, dt \tag{3.12}$$

Using, Eq. (3.11) and Eq. (3.12), we can define the instantaneous local Nusselt number and time-averaged local Nusselt number for the enclosure:

$$Nu_y = \frac{h_y L}{k_f} = \frac{q_y^{"} L}{k_f\,(T_h - T_c)}\ , \quad \overline{Nu_y} = \frac{\overline{h_y} L}{k_f} = \frac{\overline{q_y^{"}} L}{k_f\,(T_h - T_c)} \tag{3.13}$$

where k_f is the conductivity of the test fluid (air) at film temperature, i.e. $(T_h + T_c)/2$. The time-averaged Nusselt number for the entire enclosure is often of most interest for design purposes and is calculated by integrating the local values over the height of the enclosure. The time and spatially average Nusselt number and heat transfer rate are defined as:

$$\overline{Nu}_{avg} = \frac{1}{H}\int_0^H \overline{Nu_y}\, dy \quad \& \quad \overline{q_{avg}^{"}} = \frac{1}{H}\int_0^H \overline{q_y^{"}} dy \tag{3.14}$$

The trapezoid rule was used to find the approximate values of these integrals.

3.4 Experimental Set up and Procedure

To put the theoretical knowledge into practice, a set of experiments was designed. Figure 3.1 shows the steps that were followed for each experiment chronologically. First, the interferometer optics and the experimental model were set up using instruction A.3.1 (given in Appendix A). Second, if the camera had been moved since the last calibration, it was calibrated again, using the instructions written in Section 3.4.2. Third, the y-value of the measurement location was measured using the instructions written in Section 3.4.3. Fourth, the capturing of images was started. In this process, the camera manual was followed to adjust exposure time, number of images, frame rate (Hz) and to select the region of interest (ROI). It is important to review the images before transferring them for processing, because sometimes the image quality was poor. If this review revealed that images were acceptable, they were transferred to the MATLAB directory for image processing. Otherwise, the source of problem was rectified (e.g., by adjusting the size of image or exposure time) and the images capture was repeated. At the end of image processing, the images and the results from the analysis were backed up.

In the experiments, the temperature difference between the hot and cold plates was maintained at $\Delta T=15 \pm 0.5$ K. This temperature difference was obtained by heating the hot wall 7.5K above room temperature and cooling the cold wall 7.5K below room temperature. This approach was taken in order to reduce the formation of free convective boundary layers on the outward facing surfaces of both optical windows. In this way, the

laser beam will be subjected less to phase shift disturbance as it travels into and out of the test cavity.

A slight change in temperature (±0.5K) causes small change in the Rayleigh number. Therefore, in this thesis, the mean value of the Rayleigh number from all experiments for each spacing (Ra_m) is reported as representative of that spacing.

As discussed in the literature review, the conditions for transition to unsteady flow for free convection in a tall enclosure are well known. When the Rayleigh number (Ra) is lower than a critical value (Ra_c), the flow is expected to be laminar. The critical Rayleigh number for various aspect ratios can be calculated using Eq. (1.7), Korpela et al. (1982). Using this equation, the spacing of the cavity was designed in the way that the Rayleigh number was less than 75% of Ra_c. This criterion gave a cavity spacing of L=12.7mm and the Rayleigh number would be 2,860.

Also, using Eq. (1.7) for A = H/L = 960/12.7 = 75.6, $Ra_c = 5680(1 + 5/A) = 6{,}056$.

So, the design value of the Rayleigh number is about 53% of critical value. Experiment showed that the maximum Ra was 3139 (Experiments 28 and 29), and still it is much less than the critical value.

Before heating the test model, the temperature of both isothermal plates was equal to room temperature. At this moment, the finite fringes were set to be horizontal as shown in Figure 3.1 (a). At the end of the experiments, i.e., when the test model has cooled down to the room temperature again, the fringes should return to the horizontal position, as shown in Figure 3.1 (b). In practice, the fringes were not perfectly horizontal at the end of the experiment. This represented a small source of experimental uncertainty, which is discussed in Appendix B. Each point on the images has a coordinate set, (x,y),

as numbered along x and y axes. X is counted from left to right, and y is counted from top to bottom, i.e., O(0,0) is the coordinate of a the point at the top left corner of the images.

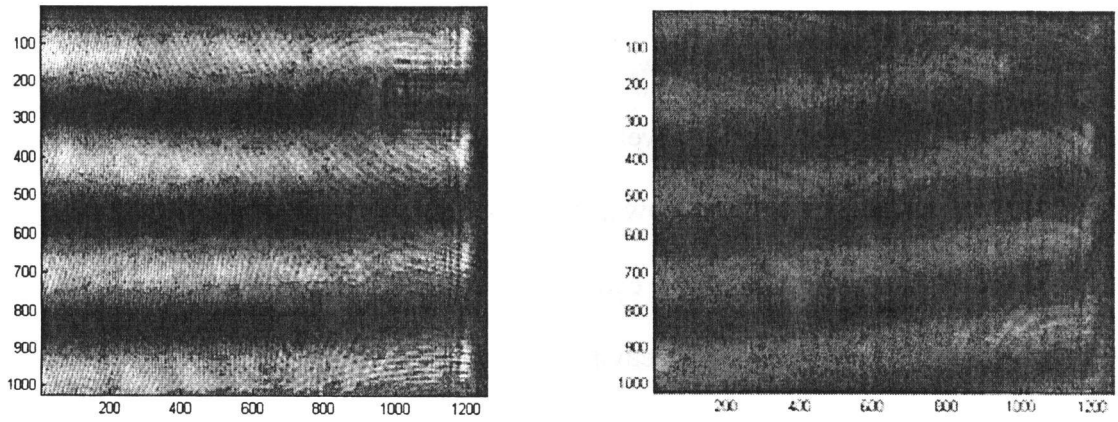

(a) (b)

Figure 3.1 Finite fringes (a) before heating the model and (b) after cooling down the test model back to room temperature.

Measurements were made only in the lower half of the cavity, because of space limitations. So, to calculate the spatial-average Nusselt number for the entire enclosure, the temperature field was assumed to be "diagonally symmetric". That is, the local convective heat transfer distribution on the lower half of the hot wall is the same as the local convective heat transfer distribution on the upper half of the cold wall. Neglecting small differences due to the temperature dependence of the fluid properties, this is expected to be a good approximation (Gebhart et al. (1988)). Using this approach, the heat flux measured on both walls in the bottom half of the enclosure was used to represent the heat flux over the full height of the enclosure.

3.4.1 Experimental Process Map

The experiment parameters (e.g., temperature, pressure, wavelength, etc.) for all the experiments were entered into an input file called ExperimentData. As shown in Figure 3.3, the image processing routine accessed this file and automatically read the appropriate parameters, when the user entered the experiment number. This input data was combined with the images from the camera in order to perform the image processing.

Image processing (step 7 in Figure 3.2) was done by successively running the files, as shown in Figure 3.4. The names inside the boxes shown in Figure 3.4 are the names of the MATLAB routines written by the author. These files all have extension ".m". The full computer code for each routine is given in Appendix A. Once the results were tabulated, they were viewed using various types of plots.

Amongst the routines shown in Figure 3.4, "iteration.m" is the most important, since this code extracts the fringe gradient from each image. The steps in its operation are shown in Figure 3.5. These steps are explained comprehensively in subsequent sections.

Table 3.1 shows a typical content of the HTResult output matrix (experiment 86) from two sample time steps (image 4 and 226). Each table is an array of 1x4 data. The first column is the fringe spacing in number of pixels, the second column is the instantaneous local heat transfer rate ($q_y^{"}$) in W/m^2, the third column is the convective heat transfer coefficient (h_y) in W/m^2K, and the last column is the instantaneous local Nusselt number (Nu_y). To see the content of this table, one should go inside the experiment directory (86), and then click on picture number directory (4 or 226 in this

example). The convective heat transfer coefficient (h) is not discussed in this thesis, but it is calculated and saved.

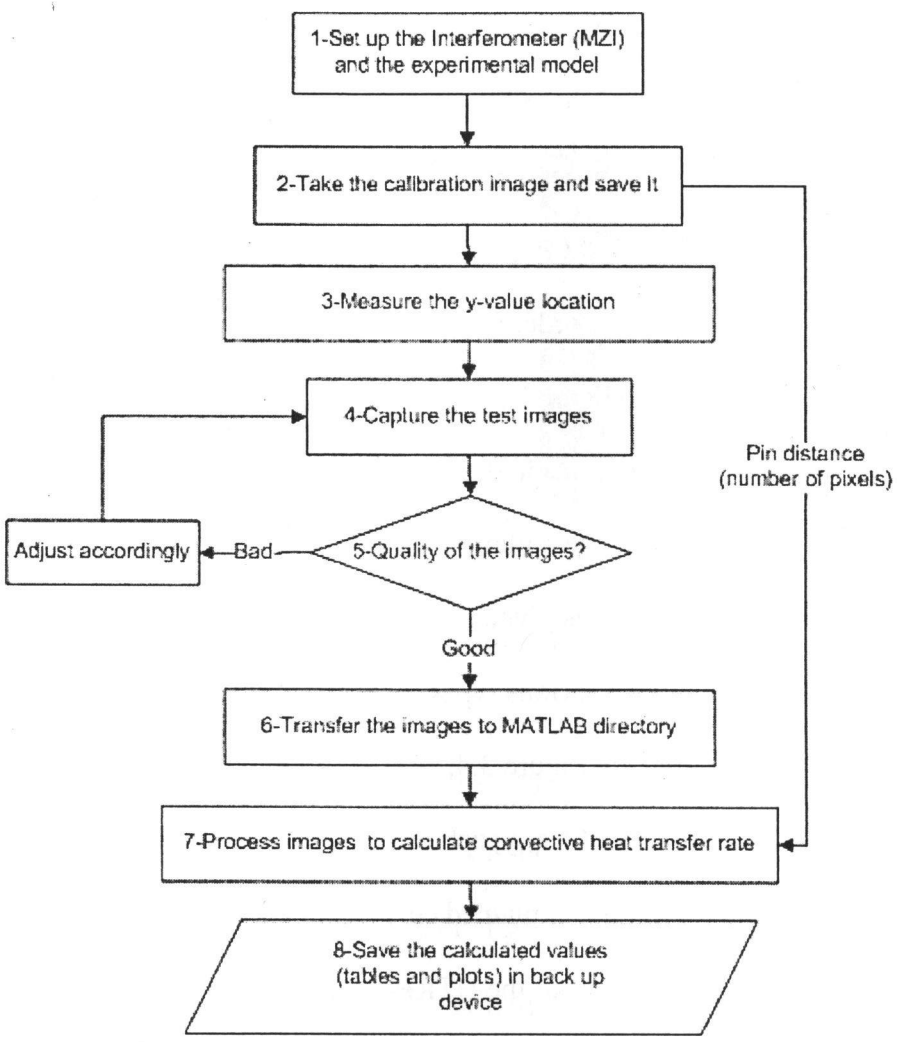

Figure 3.2 Steps in the current experiment.

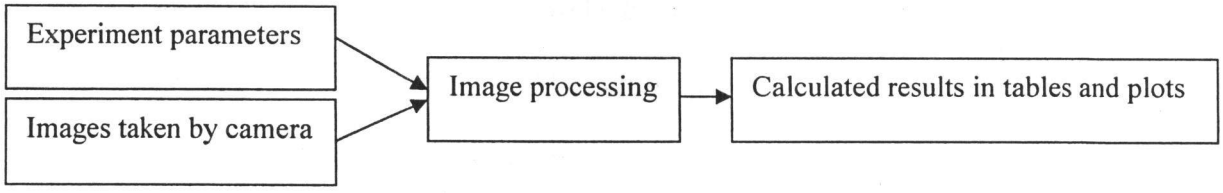

Figure 3.3 Steps in the image processing.

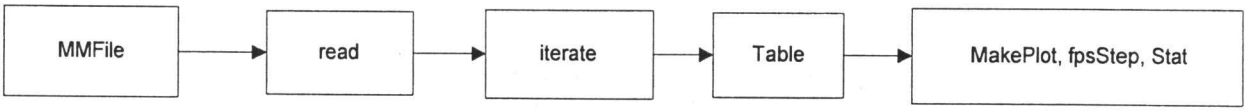

Figure 3.4 Steps used by the code to calculate the time-averaged convective heat transfer.

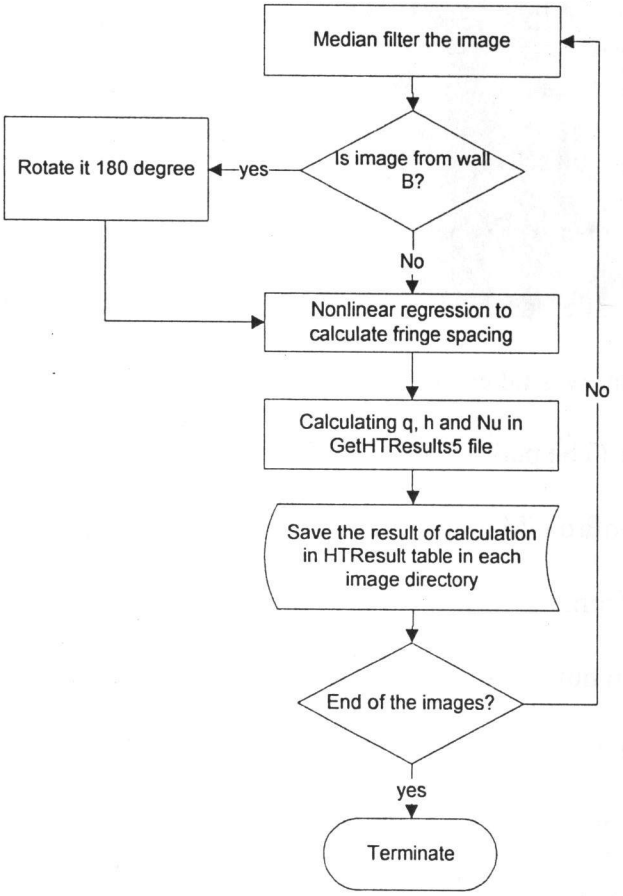

Figure 3.5 The steps followed by the routine iterate.m.

Table 3.1 Content of the HTResult matrix for two different images. The shaded area is not part of the output file.

Image number	Fringe Spacing	q''_y	h_y	Nu_y
4	43.04	56.04	3.71	5.73
226	42.79	56.37	3.73	5.77

3.4.2 Capturing Calibration Image

All length measurements in image processing were in number of pixels. To convert them to distance in meters, each length measured via image processing was multiplied by a scale factor (in m/pixel). For this reason, an image of the length calibrator was taken as soon as the camera was fixed and ready to capture the test images. To get a sharp image of the pins, only one beam (either the reference or test) was used. The calibrator was aligned such that the pin surface was perpendicular to beam travel direction. The calibrator was placed just after last beam splitter (item 6 in Figure 2.1). Figure 3.6 shows the image of calibrator that was taken as a snapshot using the MATLAB code supplied by the camera manufacturer. (The path to this file is: ProgramFiles/IDT/MotionProX/Matlab/SnapEx.m. This code is useful, since a snapshot cannot be taken directly from the MotionProX software.) The coordinates of the tips of the pins were measured in number of pixels. The difference between the x-values of the points was entered into the ExperimentData file (row 8 of the related experiment). The actual distance between the pin tips was measured in meters using a microscope with a precision x-y sliding stage, to an accuracy of one micrometer. The pin tip distance was 6.935 mm. Whenever the camera was moved, a new scale factor was calculated.

3.4.3 Determining the y-Value of the Measurement Location

As shown in the Figure 1.1, the y coordinate starts from zero at the bottom of the cavity. The elevation of the captured level was measured by placing a small plastic arrow

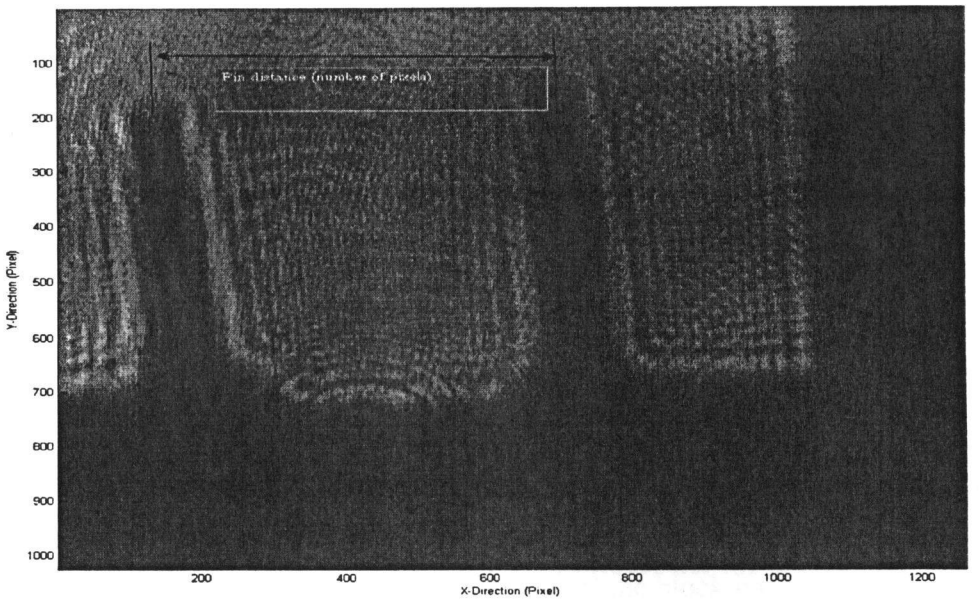

Figure 3.6 Image of the calibrating pins (Exp. 101).

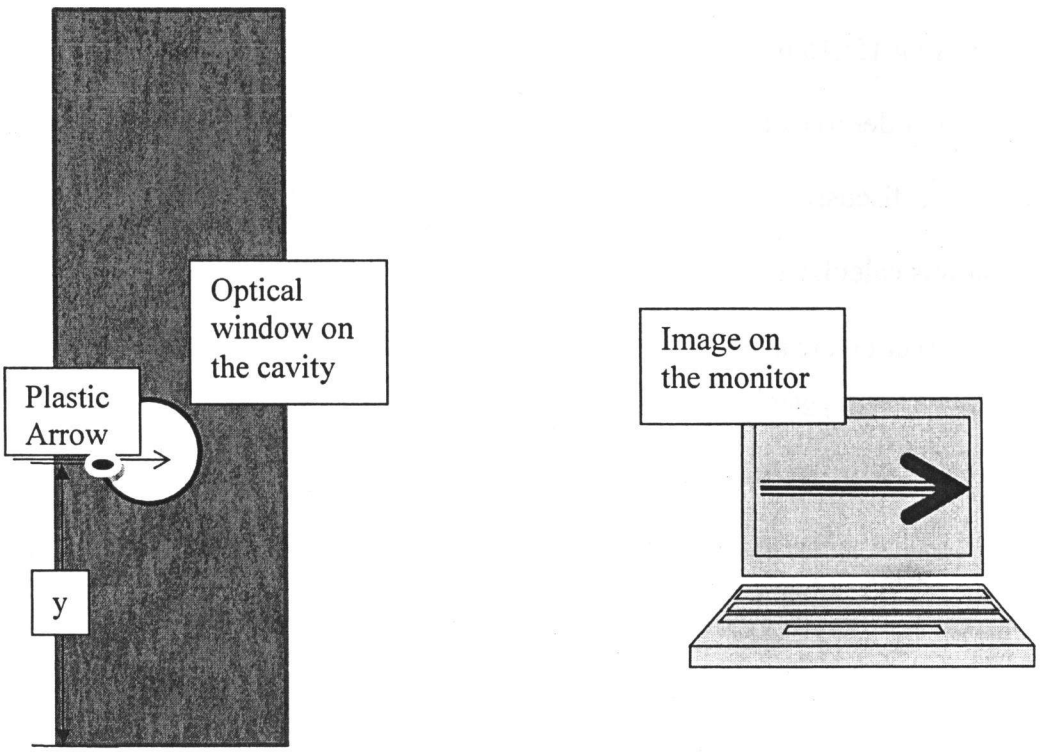

Figure 3.7 Measuring y-value of each level of captured image.

on the optical window, as shown in Figure 3.7. This arrow moved up and down along the window until it could be seen in the middle of the image. At this moment, the side of the cavity was marked at the same level. The y-value of the mark was measured using a ruler, and entered in to the ExperimentData file (row 14 of the related experiment).

3.5 Image Processing

Finite fringe interferograms were taken with the high speed camera at a frame rate of 100 frames per second for ten seconds. Prior to processing, each image was rotated slightly, if necessary, to make the measurement surface vertical. In some cases, it was also necessary to rotate the image by a full 180°, since the image processing software required that the measurement surface be on the left side of the image. This image was then enhanced using 15x15 median filter, and nonlinear regression was applied to the filtered images in order to extract the fringe gradient. The justification for these parameters will be discussed in this section. Finally, the near-wall fringe shift gradient in the x direction was calculated ($\partial\varepsilon/\partial x \mid_{x=0}$) for use in Eq. (3.11). Some information and examples in this section are adopted from the help menu of MATLAB 7.7.0 (R2008b) software.

3.5.1 Median Filter

The raw images captured by the camera contained some high frequency noise. This noise was caused by imperfections in the optical components, diffraction fringes,

dust on the optics, noise in the laser light source, etc. To reduce this noise, a median filter was first applied to each image. The median filter block replaces the central intensity-value of an m-by-n neighborhood with its median value. If the neighborhood has a center element, the block places the median value in the centre, as illustrated in the Figure 3.8.

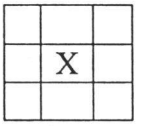

Figure 3.8 Illustration of a 3x3 median filter. The pixel intensity at pixel X is replaced by median value of the 9 surrounding pixels.

If the neighborhood does not have an exact center, the block has a tendency toward the upper-left corner and places the median value there, as illustrated in the Figure 3.9.

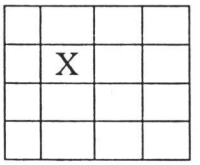

Figure 3.9 Illustration of a 4x4 median filter. The pixel intensity at pixel X is replaced by median value of the 16 surrounding pixels.

Median filtering is a nonlinear operation often used in image processing to reduce "salt and pepper" noise, without significantly reducing the sharpness of the image. A median filter is effective when the goal is to reduce noise and preserve edges simultaneously. For example, the command medfilt2(I, [m n]) performs median filtering of the image matrix I in two dimensions. Each output pixel contains the median value in the m-by-n neighborhood around the corresponding pixel in the input image. MATLAB's

medfilt2 command pads the image with zeros on the edges. So, the median values for points on the edges might appear distorted.

Figure 3.10 shows the same interferogram, before (left) and after (right) applying median filter with m = n =15. The reduction in high frequency noise, which could cause problems when calculating the fringe shift gradient, can be clearly seen.

Testing was done in order to select a median filter with dimensions 15x15. Figure 3.11 shows a typical set of data from horizontal intensity profile, after several different median filters were applied to the image. It can be seen in Figure 3.11 that a 15-by15 median filter gives adequate noise reduction, without over-smoothing the intensity profile.

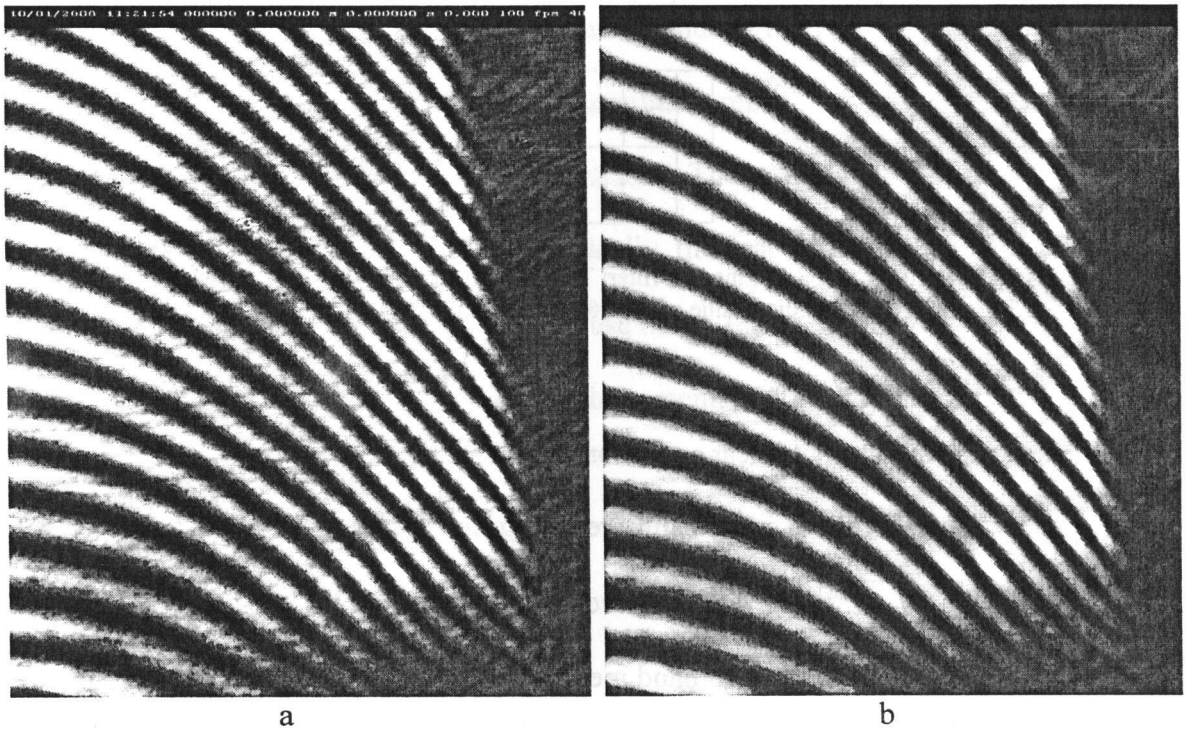

a b

Figure 3.10 Effect of 15x15 median filter: (a) the raw image, (b) the filtered image (Exp. 44).

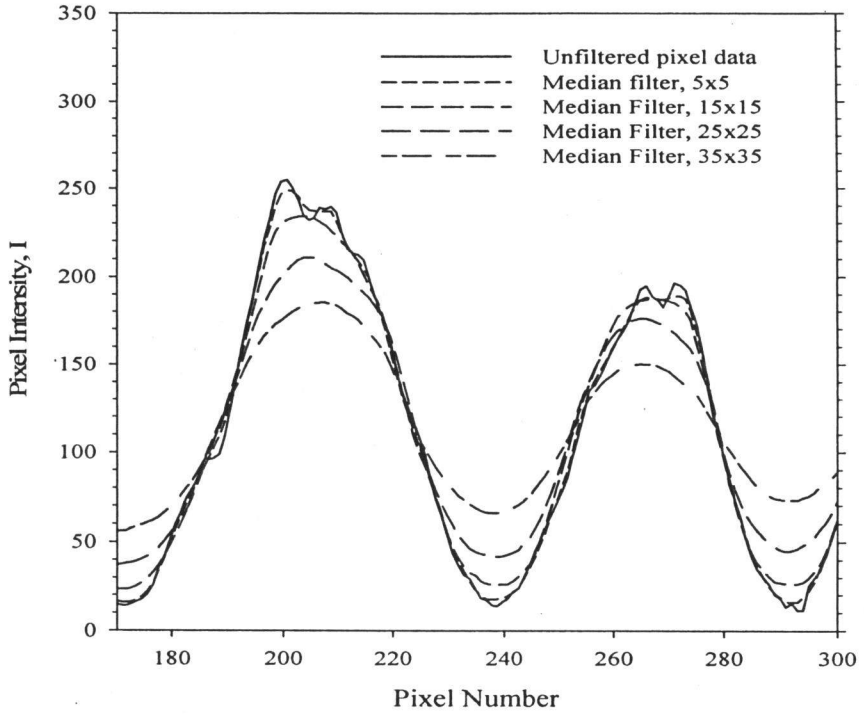

Figure 3.11 Effect of different sizes of median filter on the pixel intensity profile.

3.5.2 Image Rotation

In some cases, it was necessary to rotate the raw image prior to processing. The raw images were rotated for two different reasons:

1) The measurement surface in the captured images was not perfectly vertical in some cases. So, the image from the first time step was rotated to determine the required angular correction. This angle was then entered into the iteration file manually, if applicable. The code then automatically rotates all the images before starting fringe analysis.

2) MATLAB reads x-coordinate from left to right, i.e. the pixel line scan starts from the left and ends at the right. Therefore, in order to measure $\frac{\partial \varepsilon}{\partial x}\Big|_{x=0}$, the plate surface was

required to be on the left side of the image. Hence, images of the right plate (which was hot wall in the current experiments) had to be rotated by 180 degrees before any image processing started. This was done automatically (see the read.m file in appendix A). If zero is entered into row seven of the ExperimentData file, this computer program does not rotate the image. Otherwise, the program rotates the image. This step needs the careful attention of the experimenter to enter zero or another value that is consistent with the orientation of the wall being analyzed.

3.5.3 Inputting the Scan Line and Wall Coordinate

The computer routine needs to know the wall coordinate and start and end points of the scan line. When the code read.m was run, the wall coordinates (w1), start and end points (x1 and x2) were entered to the program. Figure 3.12(a) shows the image after median filtering and rotation by 180°. The scan line and its location are shown in this figure as well.

3.5.4 Regression

Nonlinear regression was used to extract the phase information from each pixel intensity scan. The nonlinear regression technique of Slepicka and Cha (1995), which has been slightly modified for the present application, has been used (Poulad and Naylor, 2009). If the temperature profile is linear, the fringe intensity variation will be

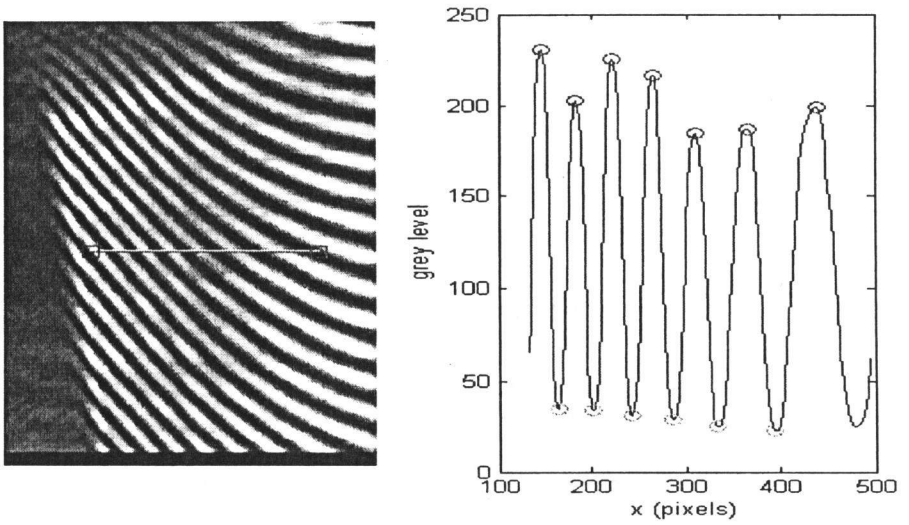

Figure 3.12 (a) Median filtered finite fringe interferogram showing the scan location, (b) the corresponding pixel grey level profile (Exp. 44, image 0).

approximately sinusoidal. So, the measured intensity near the surface can be approximated as follows:

$$I_{fit}(x) = I_{avg} + A_0 \sin\left(P(x - x_1) + \phi\right) \tag{3.14}$$

where I_{avg} (background intensity) is the mean pixel intensity, A_0 (modulation amplitude) is the amplitude, P is the rate of change of phase, ϕ is the phase shift, and x_1 is the location of the first pixel. This nonlinear function was fit to the experimental intensity data in the near wall region. The intensity data for the first complete period closest to the wall was used. I_{avg} was taken to be the average intensity value over the first full period. The three other constants (A_0, P and ϕ) were adjusted iteratively to minimize the sum of squares difference between I_{fit} and the experimental data. Once the least-squares best fit was found, the gradient of the fringe shift order was computed from the converged value of P, as follows:

$$\left.\frac{\partial \varepsilon}{\partial x}\right|_{x=0} = \frac{P}{2\pi} \tag{3.15}$$

The gradient of the fringe shift calculated from Eq. (3.15) is used in Eq. (3.11) to calculate the instantaneous local convective heat flux.

Figure 3.13 shows a sample horizontal intensity scan and the resulting best fit sine curve. This method was found to converge rapidly and was very stable. In part, this method works well because the initial values for A_0, P and ϕ can be closely estimated from the filtered experimental data. The initial value of parameter "A_0" was taken as half of the difference between the maximum and minimum pixel intensities, i.e., $A_0 \approx (I_{max}-I_{min})/2$. The initial value of P can be estimated from the locations of the mean intensity crossings, i.e., $P \approx 2\pi/(x_n-x_1)$. In a similar fashion, ϕ can be estimated from the slope of the measured pixel intensity curve. If the slope at $x-x_1=0$ is positive slope, then the initial value is taken as $\phi=0$. If the slope is negative, then $\phi=\pi$ will be a close starting guess. The detailed computer code is given in Appendix A (regression.m file).

It should be mentioned that initially, a simpler approach was attempted. Rather than using nonlinear regression, the fringe gradient was estimated by measuring the spacing between adjacent constructive or destructive fringe peaks, using only the locations of the extremum pixel values. This method was compared with the regression method discussed above. Table 3.2 and Figures 3.14 and 3.15 show the scattering reduction in the instantaneous local heat flux and fringe spacing data that was achieved using regression, compared to using only the fringe peak values. As can be seen in Table 3.2, the regression technique reduced the standard deviation by 8.1% and the percent scatter by 48.4%. The effect of regression on the time-averaged heat flux was smaller, approximately 0.7%. In this table, scattering refers to the range of the value (heat transfer

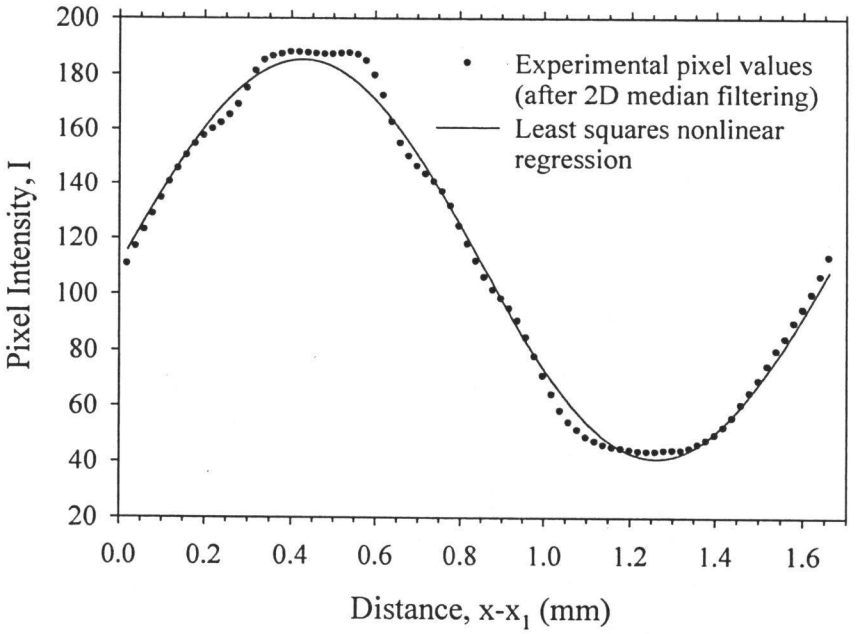

Figure 3.13 Comparisons of nonlinear regression and median filtered image values (Ra = 261240, A = 17.4, y/H = 0.12, Exp. 88).

rate or Nusselt number) to the time-average of that value multiplied by 100. The coefficient of variation (COV) is the standard deviation divided by the mean value of heat flux ($\cong \overline{q_y^{"}}$) multiplied by 100. The COV of the data with using regression is 0.182, which is lower than the COV of the data without using regression (0.197). That means regression gives the more precise data.

Table 3.2 Effect of regression on the scattering in the measured instantaneous local heat flux, $q_y^{"}$ (Ra = 261240, A = 17.4, y/H = 0.12, Exp. 88).

	Without regression	With regression
Time-averaged local heat flux $\overline{q_y^{"}}$ (W/m^2)	6.90	6.85
Standard deviation of $q_y^{"}$(W/m^2)	1.36	1.25
Scattering (%)	220.9	113.9
Coefficient of variation, COV (%)	0.197	0.182

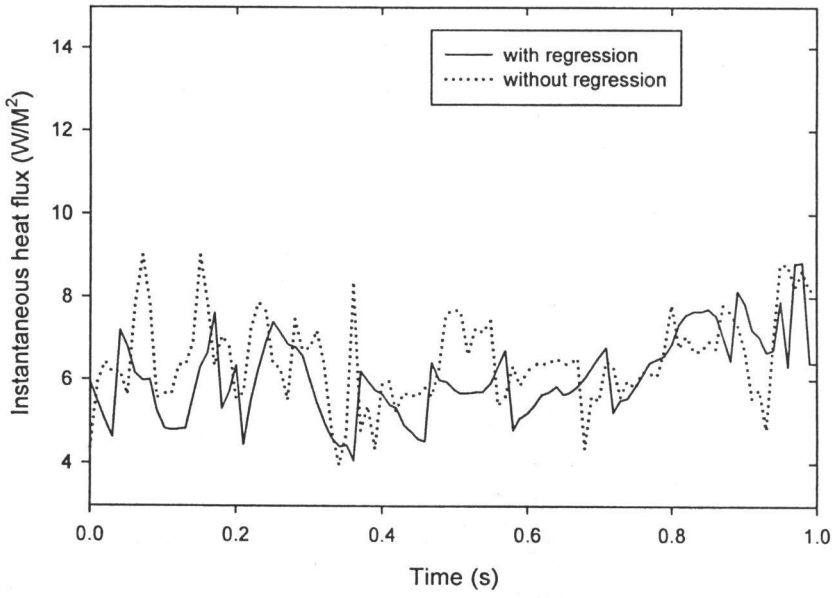

Figure 3.14 Measured instantaneous local heat flux with and without regression (Ra = 261240, A = 17.4, y/H = 0.12, Exp. 88).

Prior to conducting any experiments, the noise level of the measurement technique was measured. This was done by measuring the spacing of a finite fringe pattern in an unheated enclosure ($\Delta T = 0$). In this case, there was no fluid motion, so the measured time variations in the fringe spacing were caused only by inherent noise in the experimental technique. Figure 3.15 shows the results of these measurements. When regression was used, the typical peak-to-peak noise level was about 3.5%. For interest, the data was also processed using the initial method which used the fringe extremum values to obtain the spacing. Again, it can be seen that the regression technique greatly reduces the noise level in the measurements.

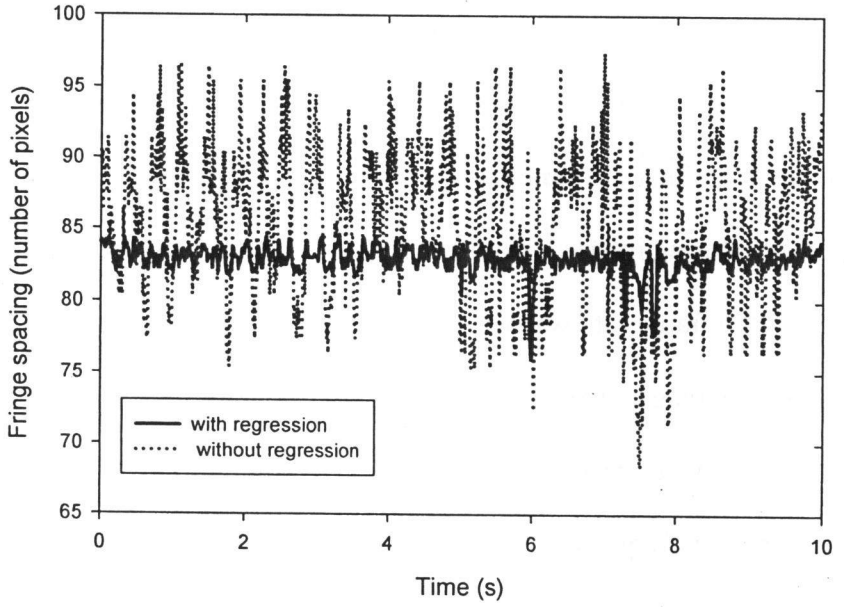

Figure 3.15 Measurements of the fringe spacing in an unheated enclosure, with and without regression ($\Delta T = 0$, Ra=0, A = 30.4, y/H = 0.5, Exp. 27).

3.6 Image Capture Parameters

Once the set up of interferometer was done and the camera was at the proper height and at the right distance from the small mirror (item 8 in Fig. 2.1), the images were captured. It was part of the design of the experiment to decide the frame rate and the duration used to capture the images. This section aims to describe how those parameters were selected.

3.6.1 Effect of Frame Rate

As mentioned in Chapter 2, the shortest possible exposure time, and hence the highest possible frame rate, depends upon the intensity of the light striking the camera

sensor. Even though the lens was removed from the camera in the present experiment, the maximum possible frame rate for the present experiment was about 500 Hz. Experiments started with a 500 Hz frame rate, and then the time-averaged Nusselt number was calculated. To evaluate the effect of frame rate on the time-averaged Nusselt number, all parameters (e.g., total capturing interval, exposure time and intensity of incident beam) were held constant and the frame rate was varied. To lower the effective frame rate under the same conditions, some images were skipped in the 500 Hz data set. The software assigned numbers to the images successively as they were captured, i.e., 0, 1, 2, 3... when they were captured at a frequency of 500 Hz. Thus, for an analysis that simulated a frequency of 250 Hz, the images numbered 0, 2, 4, 6 ... were selected for analysis. Similarly, images with numbers 0, 4, 8, 12,... were selected for analysis with a frame rate 125 Hz, and so forth. The time-averaged Nusselt number calculated using the 500 Hz data set was considered to be the most accurate and the percent difference with respect to other frequencies was calculated based on this value.

The effect of varying the frame rate on the time-averaged local Nusselt number is shown in Figures 3.16 and 3.17. Figure 3.16 shows the results calculated using the fringe centre values. The results in Figure 3.17 were calculated using regression to obtain the fringe sift gradient. Both results are for a high Rayleigh number, well into the turbulent regime. These figures show that the Nusselt number is insensitive to the frame rate used to capture the images. Except at a frame rate of 10Hz, the maximum change in the Nusselt number, compared to the value at 500Hz, was less than 0.1%. To a large degree, the low sensitivity to the frame rate is caused by the beam averaging of the temperature fluctuations. The high frequency local fluctuations are smoothed out by the laser beam,

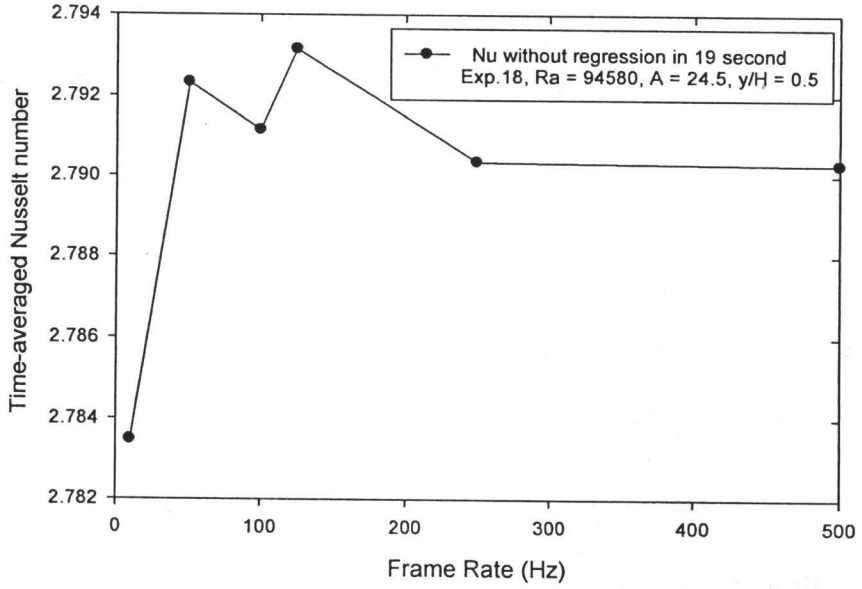

Figure 3.16 Plot of $\overline{Nu_y}$ versus frequency (without regression) on cold wall.

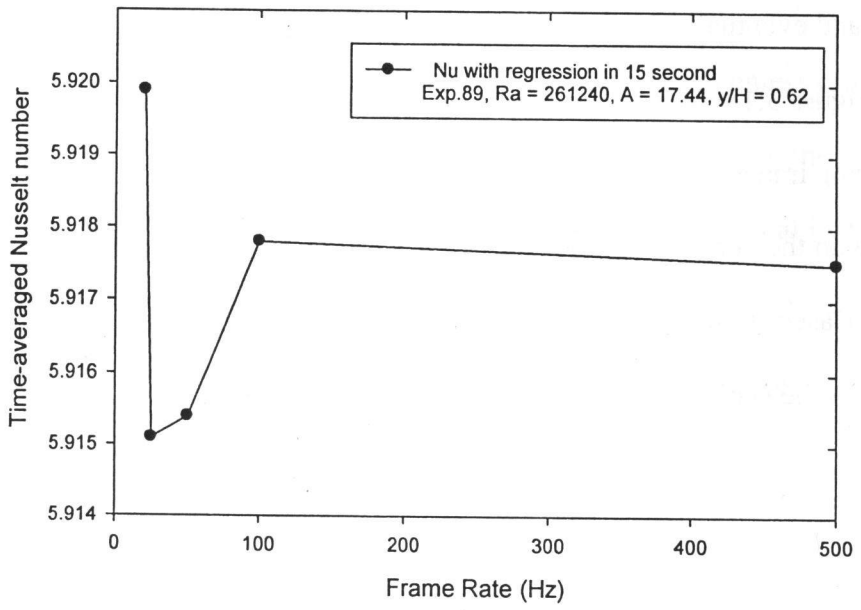

Figure 3.17 Plot of frequency versus $\overline{Nu_y}$ (with regression) on hot wall.

as it passes along the length of the model. This is a fortunate result. Clearly, high frame rates are not required in order to make accurate measurements of turbulent free

convection. However, to be conservative, a frame rate of 100 Hz was used in all subsequent experiments since there were ample computing resources available.

3.6.2 Effect of Total Capturing Time

The time interval (t) is referred to the span of the time within which the camera captures images continuously. This time is important to calculate the running time-averaged heat transfer rate. In the current work, the running time-average is the integral of either $\overline{Nu_y}$ or $\overline{q_y^{"}}$ from zero to time, t. Figure 3.18 illustrates the result of running time-averaged up to 15 seconds at 500 Hz frame rate. These are sample results, at a high Rayleigh number. It can be seen that the running time-averaged value fluctuates greatly with time at first, and eventually the fluctuation reduces appreciably when t reaches its optimum value. Figure 3.18 shows that the fluctuation has almost stopped by about 9 second. So, capturing images for longer than 9 second would not be useful. However, to be on the safe side, in the current experiments, it was decided to use a total capture time (t) of ten seconds. Based on several tests, after ten seconds, the time-averaged local heat flux was estimated to be stationary with better than ±1.0 percent.

3.7 Calculations

So far, it has been shown that a capture frequency of 100 Hz and total capture time interval of 10 seconds were sufficient to obtain accurate measurements. All images

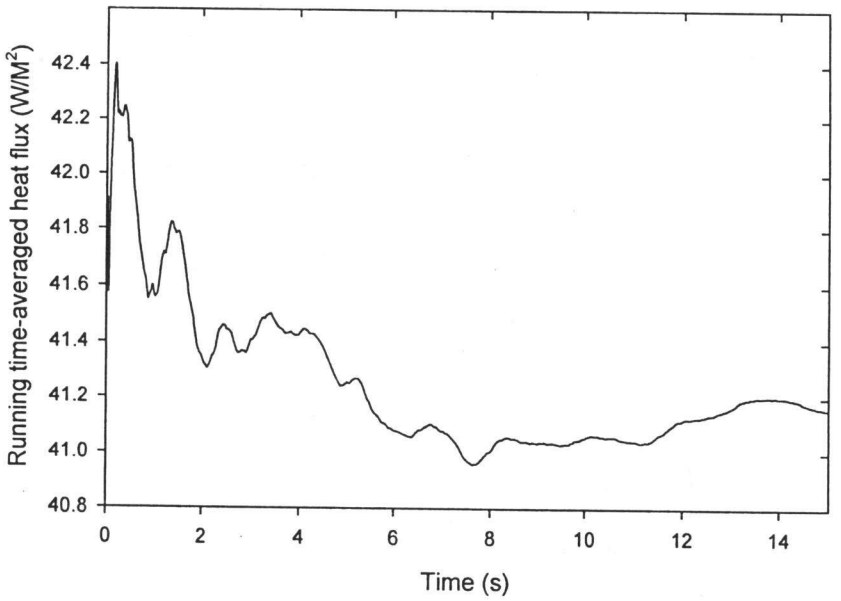

Figure 3.18 Plot of time (t) versus running time-averaged of q''_y, (Ra = 2.6×10^5, A = 17.4, y/H = 0.62, Exp. 89).

were captured using these settings (i.e. fps = 100 Hz and t = 10 s) unless otherwise specified. These values were combined with the physical constants for the experimental model, the laser wavelength, and the air properties to calculate the local instantaneous convective heat flux. All these data were entered into a matrix called the ExperimentData input file (see Appendix A). This matrix was used to automatically calculate the convective heat transfer values using Equations (3.11) to (3.14).

3.7.1 Filtering the Calculated Data

Because of noise in the fringe data, at some time steps, the instantaneous heat transfer results were calculated to be unjustifiably large or small. These data could not

represent the actual heat transfer fluctuations and needed to be removed from the results, prior to the calculation of the time-averaged heat flux. These data were removed using the following procedure: Once the Table.m program was run, it extracts and tabulates the absolute value of the contents of the HTResult tables from all image directories in a table called Table1. Each row of Table1 is filled with the HTResult contents in chronological order, i.e., the n^{th} row contains the data captured at t=n/fps. The contents of Table1 were then filtered to delete the unacceptable data, if any existed. To filter the contents of Table1, the mean value of each column was calculated, i.e., $\frac{\sum_1^n f_i}{n}$, where f is the value in each column and n is the number of rows in the column. (Conveniently, n=1000 in the present experiments). Also, the standard deviation of the data of that column was calculated. Then a factor, m, was defined as four times the standard deviation. Knowing that all data were positive in Table1, any data that were either bigger than (1+m) or less than (1-m) times the mean value were replaced by the mean. Automatically, the real time of the captured image is added to first column of the Table1, i.e., 0, 1/fps, 2/fps... n/fps where n is the number of images minus one. Table 3.3 shows the first five rows of Table1 for a typical experiment (experiment 28). The results are for "wall A", which was the cold wall. This table is a matrix with dimensions 1000x5.

Table 3.3 First five rows of matrix Table1 (shaded area is not part of the table (Exp. 28)).

Time (s)	q_y''(W/m^2)	h_y	Nu_y	Fringe Spacing (Pixels)
0.00	31.03	2.06	1.01	65.24
0.01	29.34	1.94	0.96	69.00
0.02	29.24	1.94	0.95	69.25
0.03	28.91	1.92	0.94	70.03
0.04	28.91	1.92	0.94	70.03

3.7.2 Plotting the Calculated Data

As soon as Table1 is filtered, it is possible to plot the image processing results. The last step in Figure 3.2 shows the available code used to plot the results. Table 3.4 shows the type of the plot and application of different programs.

Table 3.4 Types and applications of the plots.

Code name	Type of the plot	Application	Example
MakePlot.m	Time versus instantaneous heat transfer rate, fringe spacing and Nusselt number in three separate plots	Watching the noise and fluctuation of the results	Figs.3.12 and 3.13
fpsStep.m	Time versus time-averaged of heat transfer up to that time	Deciding the adequacy of the time interval	Fig.3.16
Stat.m	Mean value of heat flux plus/minus the standard deviation versus probability function	Observing the distribution of the data	Fig.3.19

A typical plot obtained as a result of running stat.m is given in Figure 3.19. It shows statistics about local transient heat transfer rate complied in column two of Table1. To find the probability, the number of data in each interval was divided by number of data in column two of Table1. Actually, Figure 3.19 is a histogram with the width of 0.25σ and length of probability of having a measurement in that interval. The plot only shows the line connecting the middle of each histogram column. It shows the statistics of experiment 89, for which 7438 out of 7500 data (99.2%) were found in the mean $\pm$ 2.5σ interval. The standard deviation of data in each column (σ_j) is defined as $\left(\frac{\sum_{i=1}^{n}(x_{ij}-\mu_j)^2}{n-1}\right)^{1/2}$ where n is the number of data, x_i is the value in i^{th} row of Table1 and μ_j

is the mean value of the related j^{th} column. Statistical analysis is beyond the scope of this thesis and could be the subject of other research.

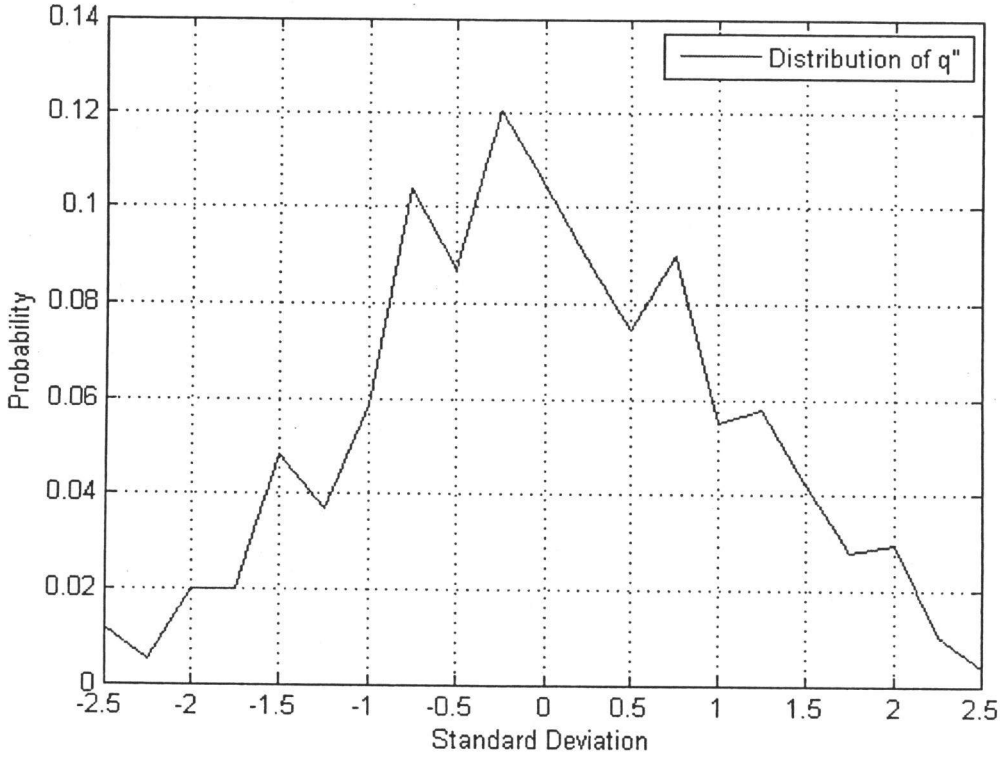

Figure 3.19 Distributions of data for experiment 89, ($Ra = 2.6x10^5$, A = 17, y/H = 0.12, hot wall).

CHAPTER 4: PRESENTATION AND DISCUSSION OF RESULTS

4.1 Introduction

Free convection heat transfer in an air-filled vertical tall enclosure was measured. Finite fringe interferograms were obtained using a Mach-Zehnder interferometer. Four cavity spacings (distance between the isothermal plates) were considered:

L = 12.7mm, 32.3mm, 40mm, and 56.2mm.

The corresponding enclosure aspect ratios were H/L=76, 30, 25, and 17. The corresponding mean Rayleigh numbers were 3.05×10^3, 5×10^4, 1.01×10^5, and 2.67×10^5. These Rayleigh numbers covered the full range, from steady two-dimensional laminar flow to strongly three-dimensional turbulent flow.

It should be noted that the temperature difference between the two isothermal plates varied slightly as the images were captured. The Rayleigh number varied by not more than ±3% from location to location, at fixed plate spacing. The mean value of Rayleigh number (Ra_m) for all experiments with the same plate spacing is reported in this chapter. The exact value of Ra for each experiment is reported on the bottom row of the Experimental data table (See Appendix D). The differential temperature between the cold (A) and hot (B) walls was kept at about 15 K during the measurements. As discussed in Chapter 3, the pictures were captured at a frequency of 100 Hz for duration of ten second. Local time-averaged and spatial average heat flux, as well as Nusselt numbers, were measured using the following equations:

$$f_{\text{Time-Averaged}} = \frac{1}{10}\int_0^{10} f_{(y,t)}\, dt \qquad (4.1)$$

$$f_{\text{Spatial-Averaged}} = \frac{1}{10H}\int_0^H \int_0^{10} f_{(y,t)}\, dtdy \qquad (4.2)$$

where H is the height of the cavity and $f_{(y,t)}$ could represent either the local Nusselt number (Nu_y) or the local heat flux (q''_y) value. $f_{(y,t)}$ is a function of elevation at which image is taken (y) and time. Time starts from the moment of capturing the first image (t=0s) and ends at t=10s. As shown in Figure 1.1, the y-coordinate starts from zero (at the bottom of the enclosure) and ends at y=H. For the experiments performed at L=12.7mm, the total height of the enclosure was H =960 mm. For all other experiments, H=980mm. There was a slight variation in H because of variations in the thickness of the edge spacers. The integration in Eq. (4.1) and (4.2) was performed numerically using the trapezoidal rule.

Over one hundred and sixty thousand images at four different cavity spacings were analyzed for this thesis. Each image showed the area of about 15mm by 20mm of the cavity. As discussed in Chapter 3, these images were taken in finite fringe mode, with about 12 horizontal fringes in the view.

It should be noted that only a small set of experimental results are presented in this chapter. The bulk of the effort (and contribution) involved the development of the image processing software, described in Chapter 3.

4.2 Laminar Flow Measurements

The measurement of time varying heat transfer rates are the focus of this thesis. However, measurements were initially made under laminar flow conditions. Under these

conditions the local heat flux should be steady. So, fluctuations in the measured heat flux gave an indication of the inherent noise in the measurement system.

The mean value of the Rayleigh number (Ra_m) was 3049 for the laminar flow experiment. Thirteen experiments were conducted to measure the local convective heat transfer in the bottom half of the cavity. These experiments were numbered as: 28, 29, and 32 to 42 inclusive.

4.2.1 Instantaneous Values

Figure 4.1 shows the time variation of the local Nusselt number near the centre of the enclosure, under steady, laminar flow conditions. Under these flow conditions, the actual convective heat transfer rate should not vary with time. However, it can be seen in Figure 4.1 that the results show some fluctuations. In these results, the instantaneous local Nusselt number fluctuates within about $\pm 2.8\%$ of mean value. The standard deviation ($SD = \sqrt{\sum_{i=1}^{n}(u - x_i)^2/(n-1)}$, where u was the mean value and n was the number of data) was found to be 0.01. This noise is due to digitization, imperfections in the optics, and/or vibration (due to location and setup). These fluctuations are always present in the current experimental setup. Table 4.1 shows the time-average heat transfer results for this experiment at various values of the y-coordinate. The mean scattering value for laminar flow is about 6.3%. It should be noted that, in turbulent flow, this high frequency noise will be superimposed upon the actual fluctuations in heat flux.

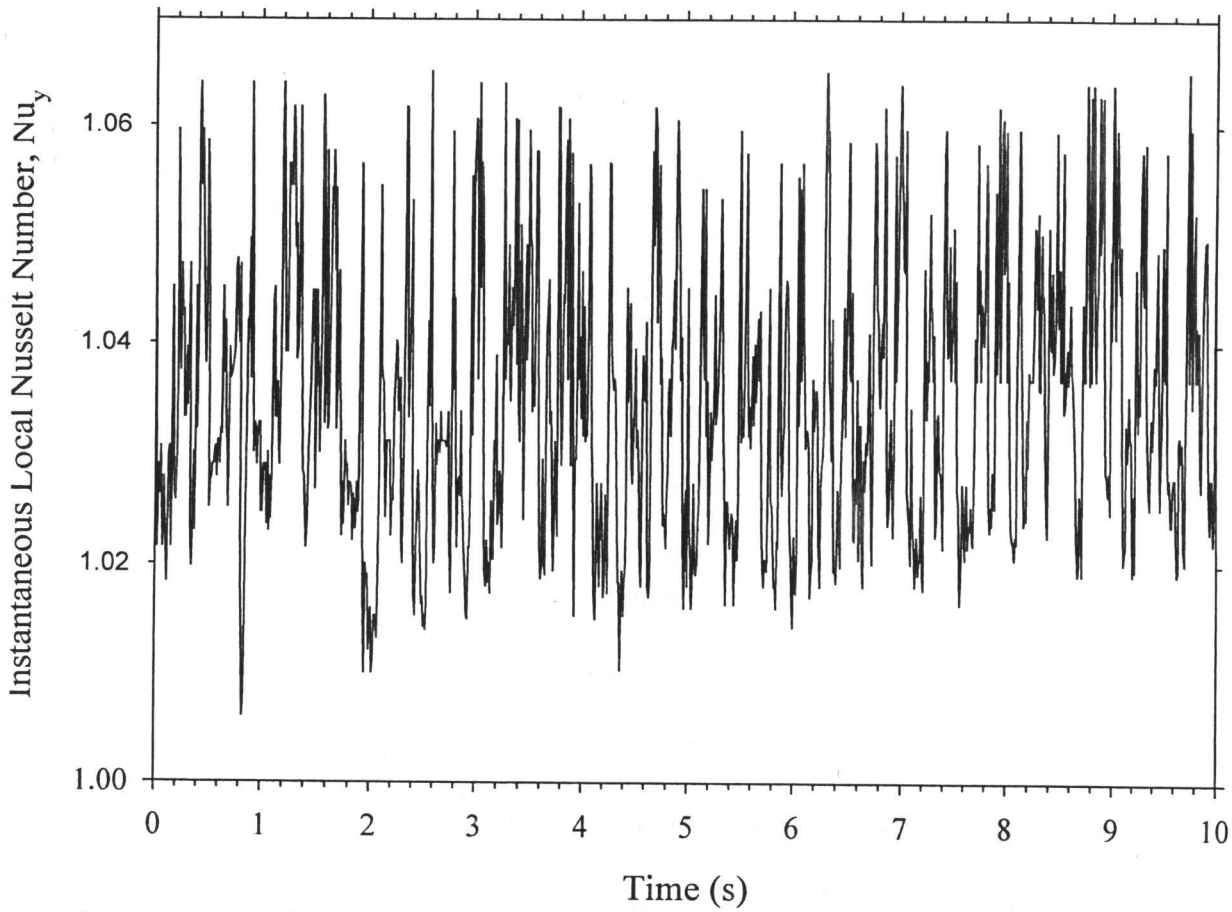

Figure 4.1 Instantaneous local Nu_y under steady laminar flow conditions (Exp. 28, Ra =3139, A =75.6, y/H = 0.49, wall B).

4.2.2 Time-Averaged Values

Table 4.1 presents the results of calculations of all experiments for laminar flow. The gap width for this set of experiments was 12.7 mm. The camera captured a view with about 15 mm in the x direction. So, in this case, it was possible to capture the interferogram of both walls simultaneously. For this reason, the two series of data share

the same experiment number in Table 4.1. In this thesis, SD stands for standard deviation of heat flux. Therefore, SD and $\overline{q_y^{"}}$ have the same units, W/m^2.

Table 4.1 Time-average local heat transfer results for laminar steady flow at various values of the y-coordinate (A = 75.6, Ra_m = 3049).

Y (mm)	$\overline{Nu_y}$	$\overline{q_y^{"}}$(W/m^2)	SD (W/m^2)	Scattering (%)	Exp. #	Wall
5	0.50	15.2	0.41	14.48	40	A
15	0.88	26.72	0.38	8.27	41	A
30	0.85	25.85	0.22	4.28	42	A
35	0.81	24.88	0.47	7.63	37	A
65	0.93	28.28	0.41	7.31	36	A
95	0.97	29.7	0.31	5.35	35	A
124	0.99	30.06	0.34	7.12	34	A
189	0.98	29.83	0.32	4.09	33	A
252	0.97	29.56	0.32	6.07	32	A
287	0.94	28.67	0.17	3.16	39	A
352	1.06	32.34	0.55	8.86	38	A
416	0.98	29.98	0.36	7.7	29	A
470	0.98	30.09	0.83	9.08	28	A
470	1.04	31.78	0.38	5.71	28	B
416	1.04	32.03	0.17	3.54	29	B
352	1.08	33.07	0.93	10.58	38	B
287	0.97	29.71	0.4	6.99	39	B
252	1.07	32.66	0.18	2.69	32	B
189	1.02	31.16	0.35	3.87	33	B
124	1.00	30.54	0.34	5.79	34	B
95	1.00	30.44	0.33	4.5	35	B
65	0.96	29.37	0.16	3.56	36	B
35	1.00	30.7	0.28	5.56	37	B
30	1.07	32.77	0.22	4.836	42	B
15	1.05	32	0.38	6.64	41	B
5	2.02	61.4	0.87	5.69	40	B

Figures 4.2 illustrates the data in Table 4.1. It can be seen that over the centre region of the enclosure, the heat transfer is conduction dominated, because the local Nusselt number is about 1.0. However, at the bottom of the hot wall, the local Nusselt number is about two times the value for pure conduction. Also, at the bottom of the cold

wall, the heat transfer rate is much lower than for pure conduction. In these regions, convection plays an important role. Air rises on the hot wall and descends on the cold wall, producing a recirculation due to buoyancy effects. The high local heat flux at the bottom of the hot wall is caused by the impingement of the cold air, as it turns the corner to travel upward. That is why the convective heat transfer has its highest value at the bottom of the hot wall. The hot wall transferred some of its heat to the cold air at this point. The air is heated, becomes lighter, and moves upward. On the other hand, at the bottom of the cold plate the heat flux is very low. The region of low heat flux corresponds to the region where the air flows away from the cold wall. The convective heat transfer on both wall are almost equal in the centre region, approximately $y/H > 0.1$.

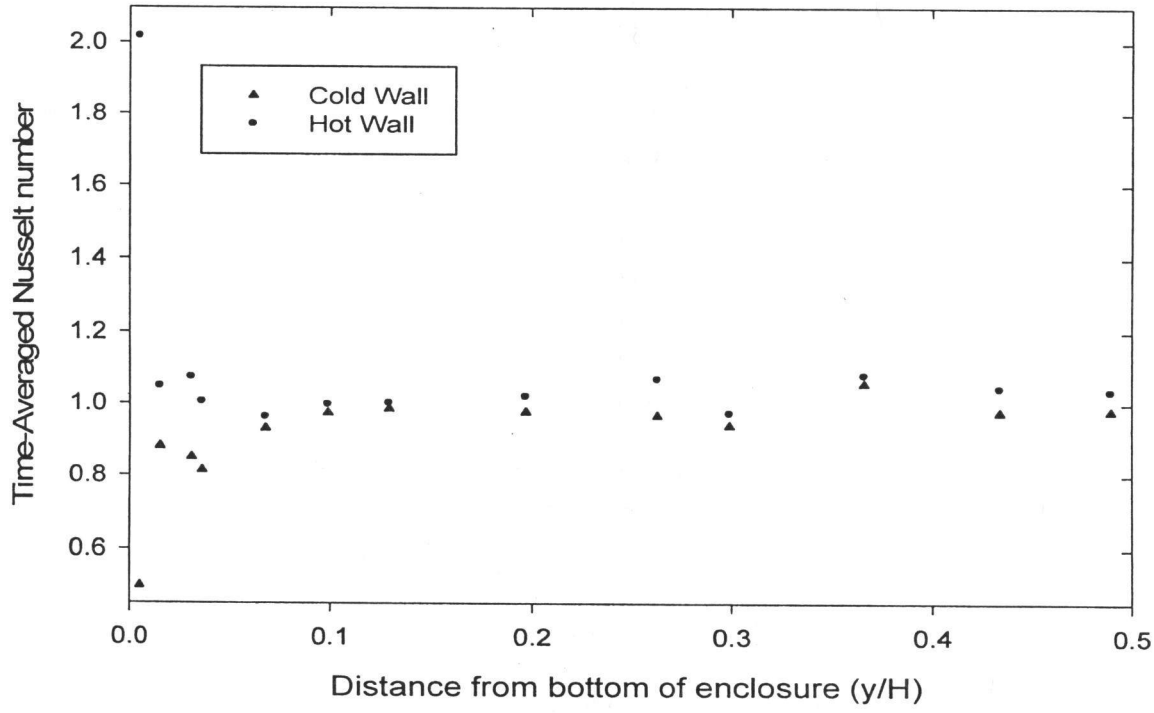

Figure 4.2 Time-averaged local Nusselt number $\overline{Nu}_y$ on the hot and cold walls in the conductive regime ($Ra_m = 3049$).

4.2.3 Comparison with Numerical Values

The experimental calculations for local time-averaged heat flux were compared with a numerical solution using the FLUENT software. In the numerical solution, the flow was assumed to be steady, laminar and two-dimensional. The comparison is shown in Figure 4.3. To be consistent with the numerical calculations, the negative sign was used for the heat flux on the cold wall.

It can be seen in Figure 4.3 that the results are in good agreement in the centre portion of the cavity. However, there are significant differences, as much as 36%, in the region of the end walls. The end walls were considered adiabatic in the numerical solution. Practically, these walls were not adiabatic. This may be the reason that the numerical solution predicted a higher heat flux at top of the plate than was found experimentally. Another source of error was the uncertainty of the fringe spacing measurements at the top corner. Due to high heat transfer flux at the top, the fringes were fine and hard to resolve. This could be another source of error that caused some of the departure of the experimental and analytical results.

4.2.4 Comparison with Empirical Correlations

Table 4.2 summarizes the average heat transfer results ($\overline{Nu}_{avg}$) of the experiments in laminar flow. The present measurements were compared with the empirical correlations of ElSherbiny (1980) and Wright (1996). These correlations are widely used in the literature and are considered to be the most accurate. At this Rayleigh number, the

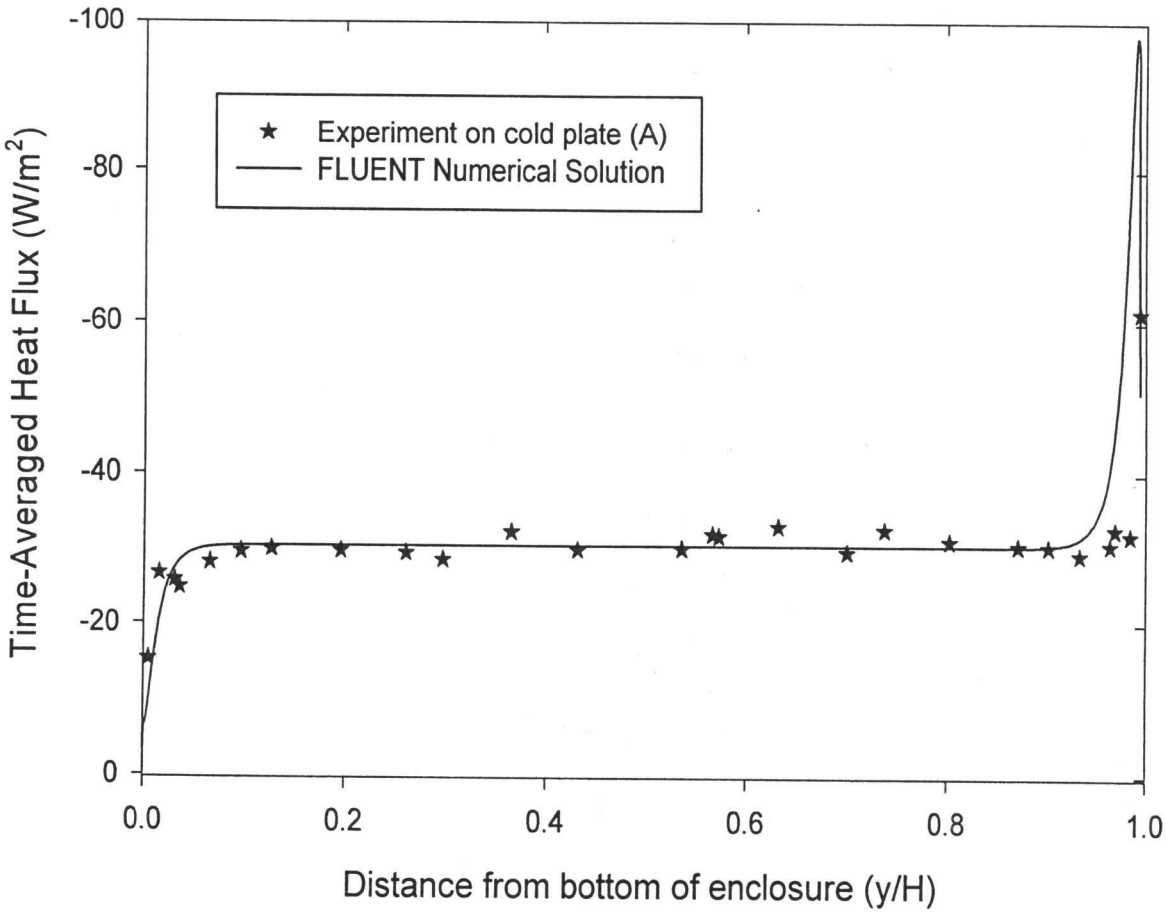

Figure 4.3 Comparison of experimental and numerical local heat flux distribution on the cold wall for laminar flow $Ra_m = 3049$.

empirical correlations predict a Nusselt number slightly higher than that for pure conduction. It can be seen in Table 4.2 that the difference between the ElSherbiny correlation and present work is 1.16%. In the experiment, the measured value was slightly less than for pure conduction. (Of course, since convection is present within enclosure, the actual average Nusselt number cannot be less than 1.0.)

Table 4.2 Comparison of spatial-averaged heat transfer results ($\overline{Nu}_{avg}$) with empirical correlations from the literature.

Reference	A	$\overline{Nu}_{avg}$	Ra_m
ElSherbiny Experiment	40	1.030	3293
ElSherbiny Experiment	110	1.010	3303
ElSherbiny Experiment	80	1.000	3238
ElSherbiny Correlation	75.6	1.009	3049
Wright Correlation	75.6	1.018	3049
Present Work	75.6	0.998	3049

4.3 Turbulent Flow Measurements

Successful experimental results in laminar flow were a good motivation to measure convective heat transfer under turbulent conditions. Measurements were made for three different cavity widths (and aspect ratios). The sizes, number of experiments at each size and corresponding Ra_m are summarized in Table 4.3. Each experiment corresponds to a single local heat flux measurement at a specific y/H location, except near the corners. The Rayleigh number range of these measurements is well into the turbulent regime. As mentioned in the literature review, Wright et al. (2006) have shown experimentally that unsteady secondary flows exist in a tall enclosure for $Ra>9.6x10^3$.

Table 4.3 Size, aspect ratio, mean Rayleigh number and number of experiments used for turbulent flow conditions.

L (mm)	Aspect Ratio	Ra_m	Number of Experiments
32.3	30. 34	$5x10^4$	26
40	24.5	$1.0x10^5$	20
56.2	17.44	$2.7x10^5$	24

It should be noted that the number of local coefficients is more than the number of experiments because two measurements were made from each image near the corners of

the enclosure. At each camera position, the height of the "window" seen by the camera was about 20 mm. In the corner region of the enclosure, two local heat transfer coefficients were calculated from one sequence of images. In this way, measurements were made at a location of 5 mm and 15 mm from the bottom of the enclosure.

4.3.1 Instantaneous Local Heat Transfer Results

Figures 4.5 and 4.4 show the transient value of the local Nusselt number in the middle of the cavity. Figure 4.4 shows the results at Ra=5.04×10^4 and Figure 4.5 shows the results at Ra = 9.80×10^4. It can be seen that the local heat transfer fluctuates by as much as 25.5 and 30 percent of the mean value of Nusselt number, respectively. In general, it was found that the range of the fluctuation increased as the Rayleigh number increased. This is consistent with the development of stronger turbulent eddies that higher Rayleigh numbers.

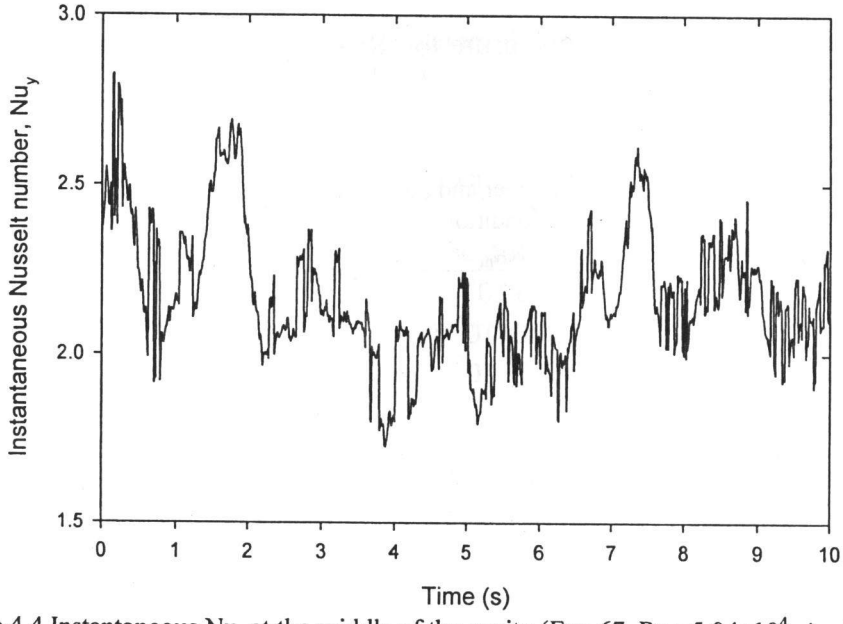

Figure 4.4 Instantaneous Nu_y at the middle of the cavity (Exp 67, Ra =5.04×10^4, A =30.3, y/H = 0.5).

As shown in Figure 4.6 the convective heat transfer is higher at the top of the cold plate than the middle of the plate. It is interesting to note the level of turbulent fluctuation in these results. Near the corner, the range of the turbulent fluctuations is lower and of higher frequency than in the middle of the enclosure. The proximity of the enclosure wall reduces the level of turbulence in this region.

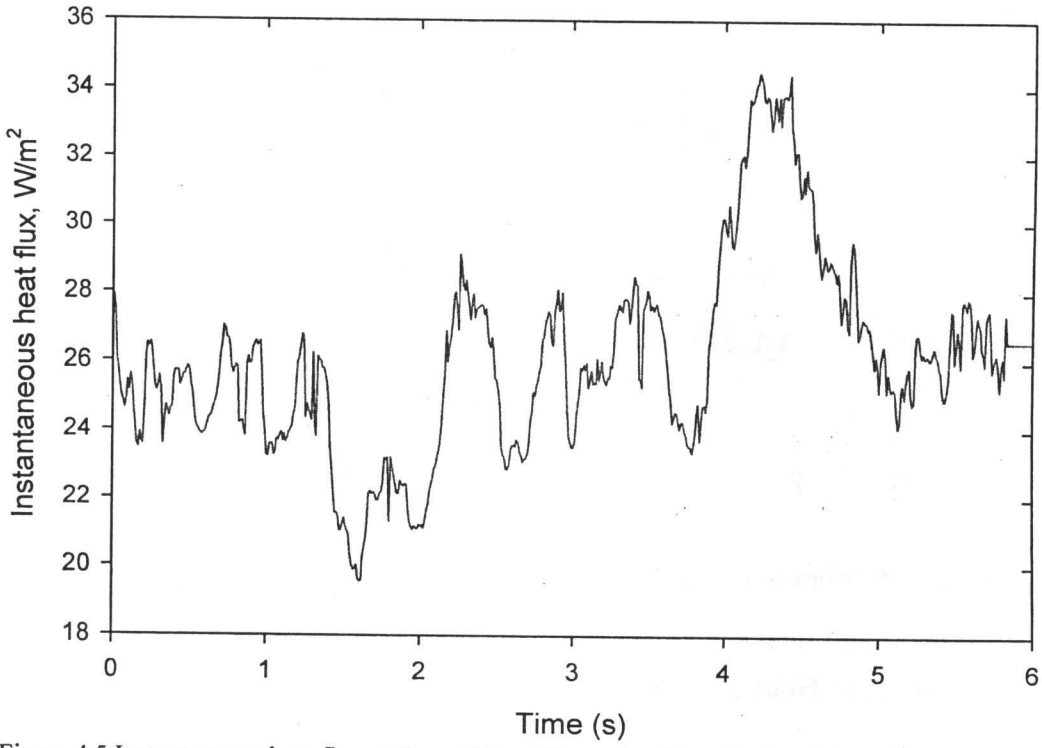

Figure 4.5 Instantaneous heat flux at the middle of the cavity (Exp 68, Ra =9.80x10^4, A =24.5, y/H = 0.49).

In rare cases, the image processing algorithm failed, and it was not possible to process the entire ten seconds of data. An example is shown in Figure 4.7. It can be seen that the convective heat flux became unjustifiably high after three seconds. One possible

reason was excessive vibration, which was intermittent. This case was rarely found, and, whenever it was found, the analysis was manually terminated. In these cases, the time averaged heat flux was calculated using the data up the time of failure.

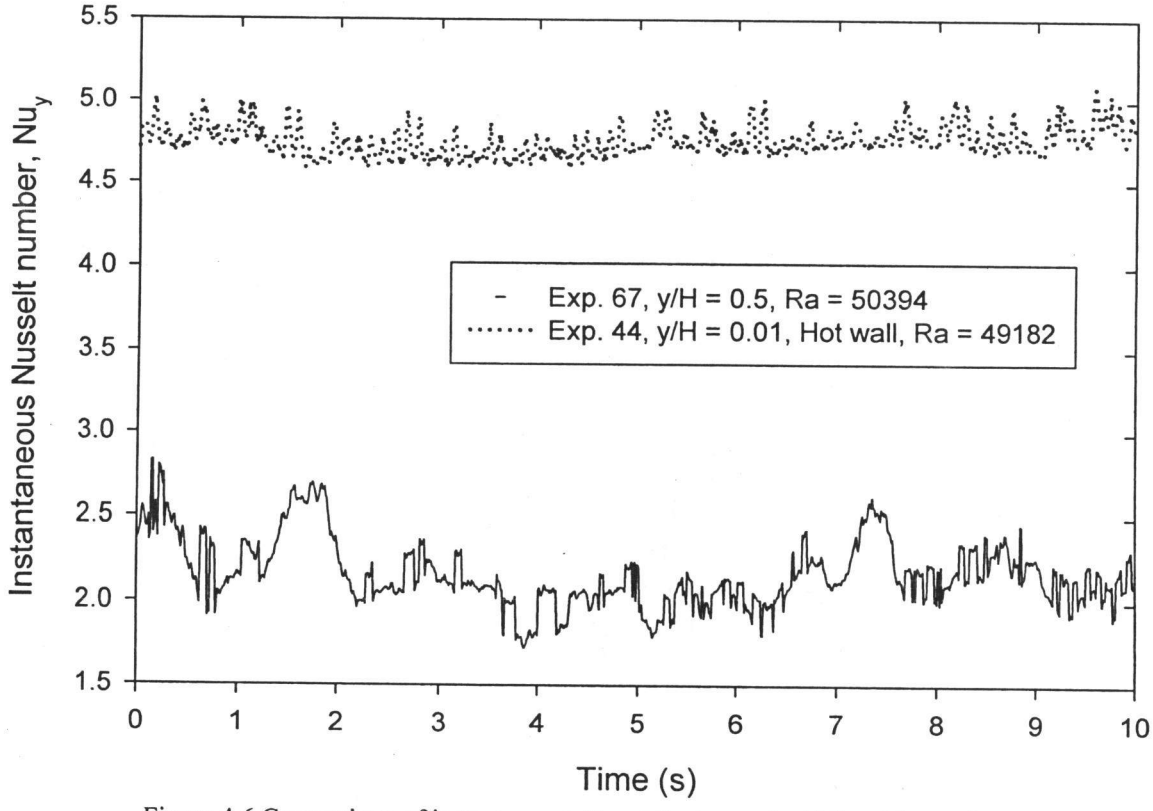

Figure 4.6 Comparison of instantaneous Nu_y at the top and middle of the cavity.

4.3.2 Time-Averaged Heat Transfer Results

Figures 4.8 to 4.10show the time-averaged local Nusselt number distributions on the enclosure walls. These figures show that the local heat flux increases as the y increases on cold wall. On the hot wall, the convective heat flux has a maximum value near the lower edge and decreases up the wall. Near the middle of the cavity, both walls have approximately the same convective heat transfer. This is expected, because of the

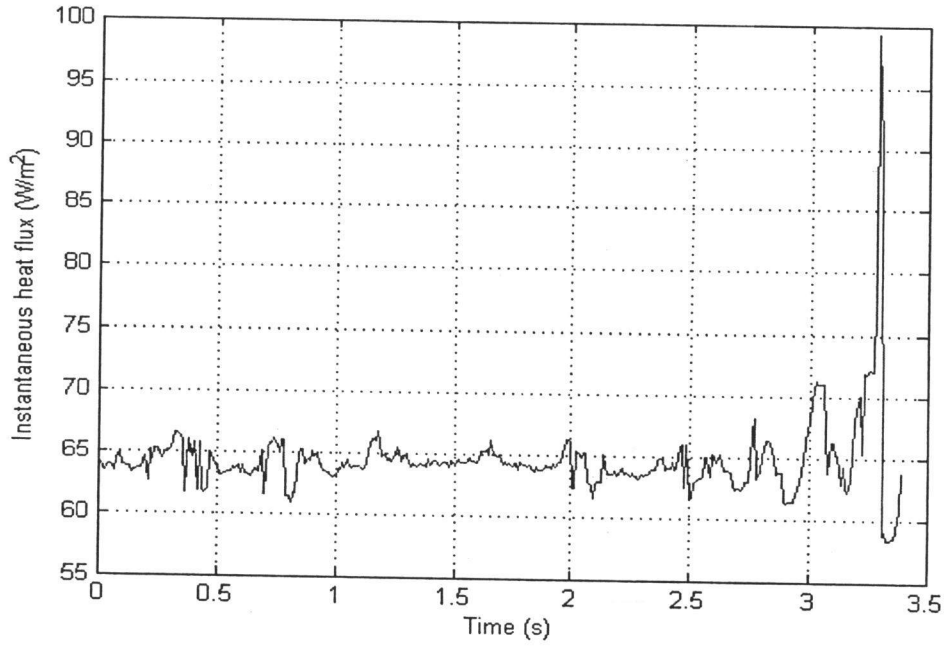

Figure 4.7 Instantaneous heat flux (Exp. 86, Ra =97226, A =24.5, y/H = 0.99).

"diagonal symmetry" of the temperature field. This trend was the same as for the laminar flow convective heat transfer. The local convective heat flux (q''_y) is very low at the bottom of the cold plate. The full results are tabulated in Appendix D.

The spatial average values of Nusselt numbers were compared with the ElSherbiny correlation, as shown in Table 4.4. The largest difference between present measurements and the ElSherbiny correlation was about 13.8%. The current measurements are consistently lower than the predictions from the correlation.

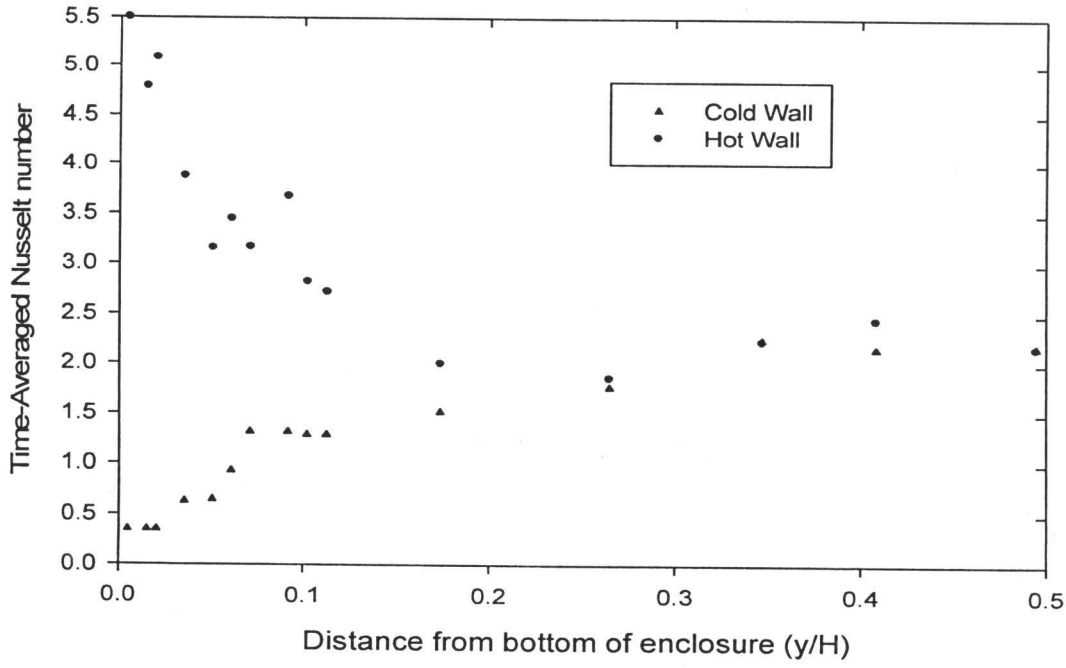

Figure 4.8 Time-averaged local Nusselt number ($\overline{Nu}_y$) distribution on the enclosure walls ($Ra_m = 5x10^4$).

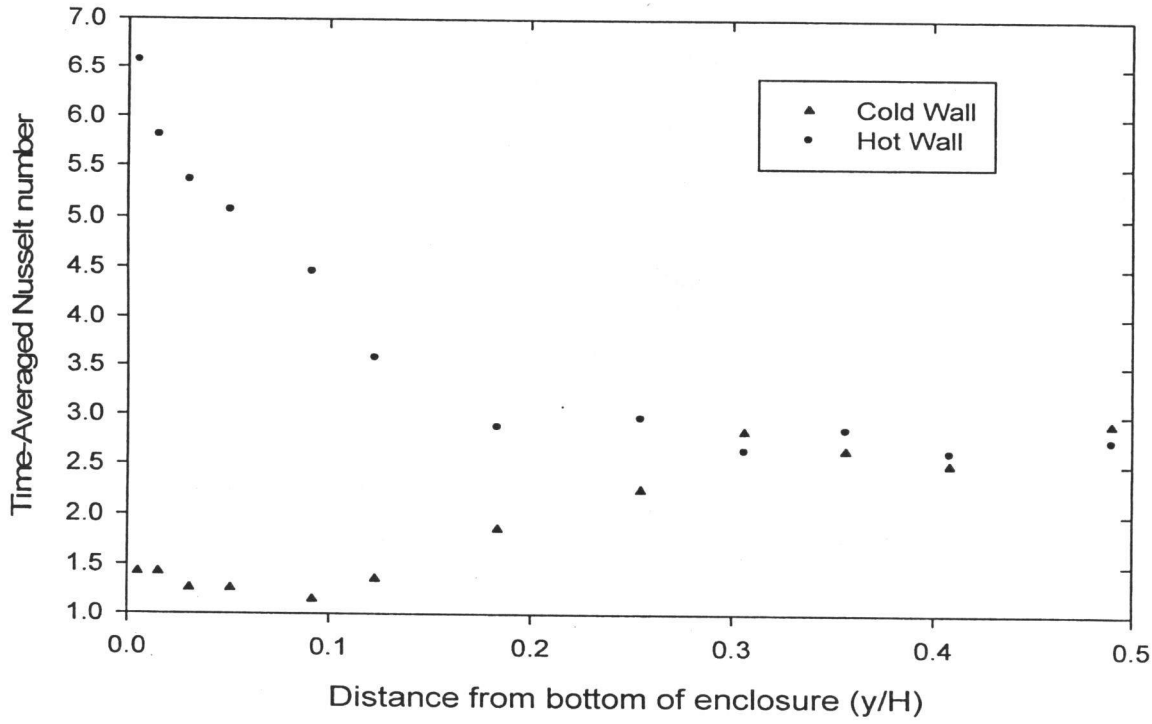

Figure 4.9 Time-averaged local Nusselt number ($\overline{Nu}_y$) distribution on the enclosure walls ($Ra_m = 10^5$).

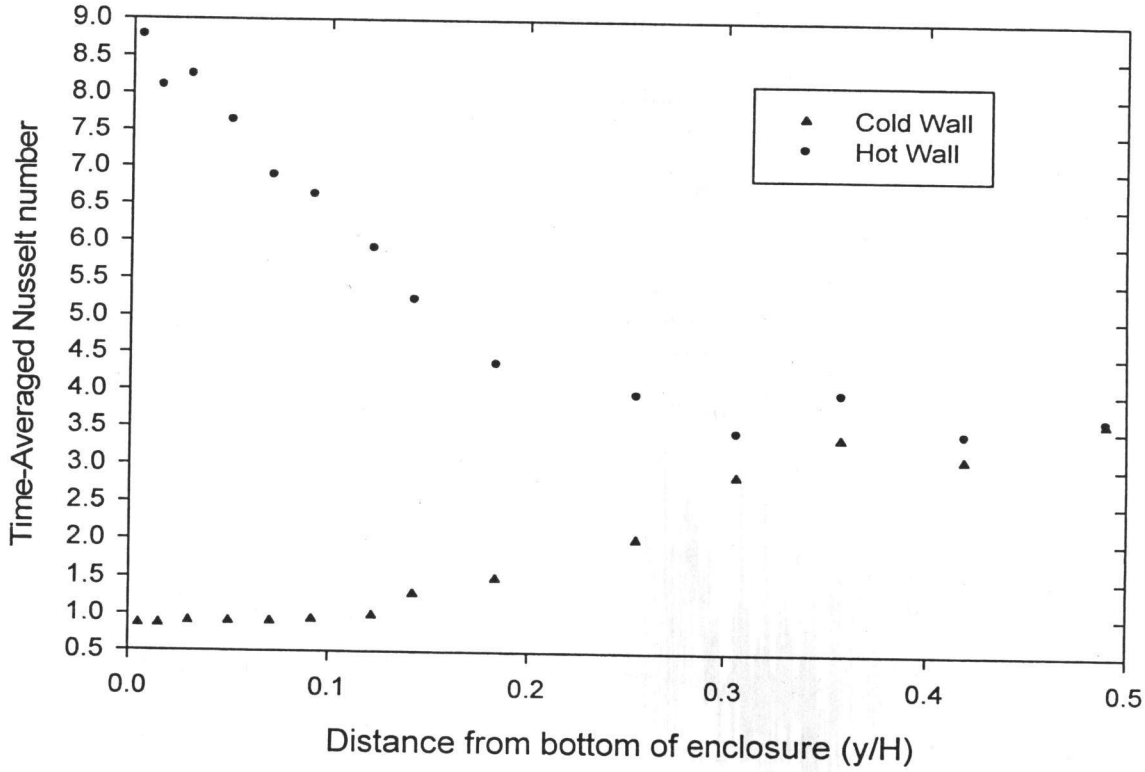

Figure 4.10 Time-averaged local Nusselt number ($\overline{Nu}_y$) distribution on the enclosure walls ($Ra_m = 2.7x10^5$)

Table 4.4 Comparison of spatial-averaged Nusselt number with the ElSherbiny correlation (1980).

		$\overline{Nu}_{avg}$		
Ra_m	A	Present Work	ElSherbiny correlation	%difference
$5x10^4$	30.3	2.09	2.38	12.2
10^5	24.5	2.72	2.98	8.7
$2.7x10^5$	17.4	3.46	4.02	13.8

4.3.3 Running Time-Averaged Heat Transfer Results

In any fluctuating phenomena, a time-averaging technique is used to report the average value of the fluctuating identity over the time. This technique was also used here to report the convective heat transfer values over time. Figure 4.11 shows the instantaneous and running time-averaged values of instantaneous local heat transfer on

the same graph. The running time average value at time t is the average value from time zero to t. Despite transient fluctuation, it can be seen in Figure 4.11 that the time-averaged plot is almost a horizontal line after five second.

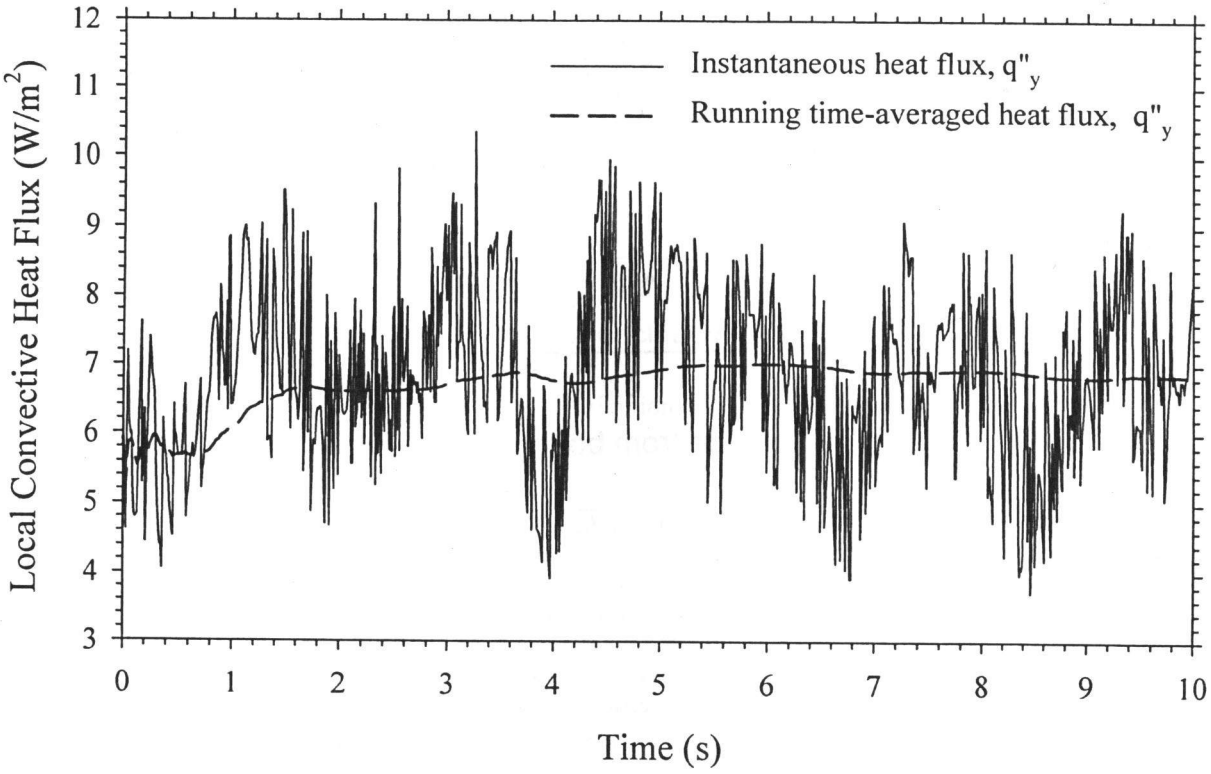

Figure 4.11 Instantaneous and Running time-averaged heat flux (Exp. 88, Ra =2.6x10^5, A =17.4, y/H = 0.12).

To get the idea of uncertainty due to the running time averaging after ten seconds, three experiments were conducted, each with a duration of 20 seconds. Three sets of measurements were made at precisely the same location (experiments 144, 145 and 146). Then each experiment was divided into two experiments (the first 10 seconds were called 144a, 145a and 146a and the last 10 seconds were called 144b, 145b and 146b. The running time-averaged heat fluxes of these six experiments were calculated. The results,

as tabulated on Table 4.5, showed about ±2.2% (±0.4 W/m^2) uncertainty (Taylor and Kuyatt (1994)).

Table 4.5. The running time-averaged heat flux, which was measured at the same location with capturing time intervals of 10 and 20 seconds.

	Heat flux (W/m^2) for t = 10 seconds	Heat flux (W/m^2) for t = 20 seconds
Running time-averaged heat flux	20.43, 19.70, 19.60 20.16, 20.49, 20.31	20.29, 20.10, 19.95
The mean heat flux	20.11	20.11
Standard deviation	0.38	0.17

Figures 4.13 and 4.12 show the graph of running time average measurements. For better clarification, in Figure 4.13, the interval between 2 and 18 was broken off. It can be seen in Figure 4.13 that, had the experiments been conducted with a 20 second capture interval, this source of uncertainty could have been reduced to about ±0.8%.

4.4 Final Results

Figure 4.14 shows the comparison of the spatial average Nusselt number from the present work with the experimental data of ElSherbiny (1980). The ElSherbiny correlation is shown as a solid line. For laminar flow in the conduction regime, the present work is in good agreement with the ElSherbiny results. In turbulent flow, the present technique produced slightly lower Nusselt numbers than ElSherbiny's results.

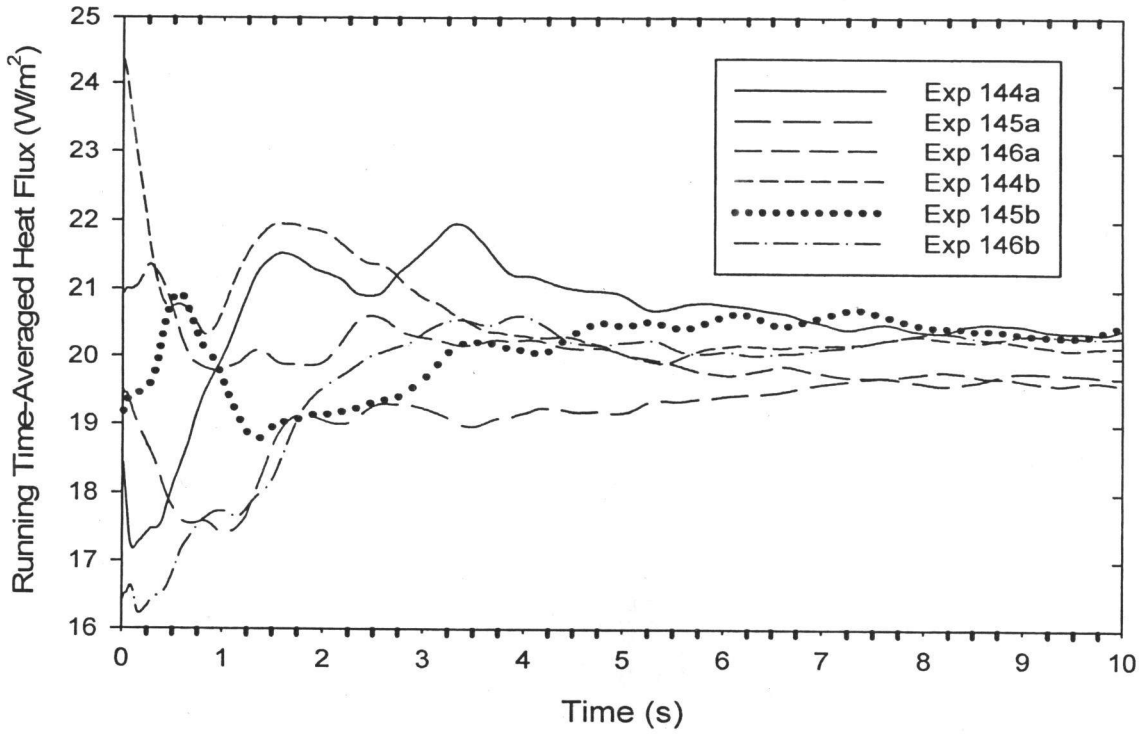

Figure 4.12 Six times measurements of running time-averaged heat flux of the same location for t = 10s ($Ra = 2.8 \times 10^5$, A =17.3, y/H = 0.27).

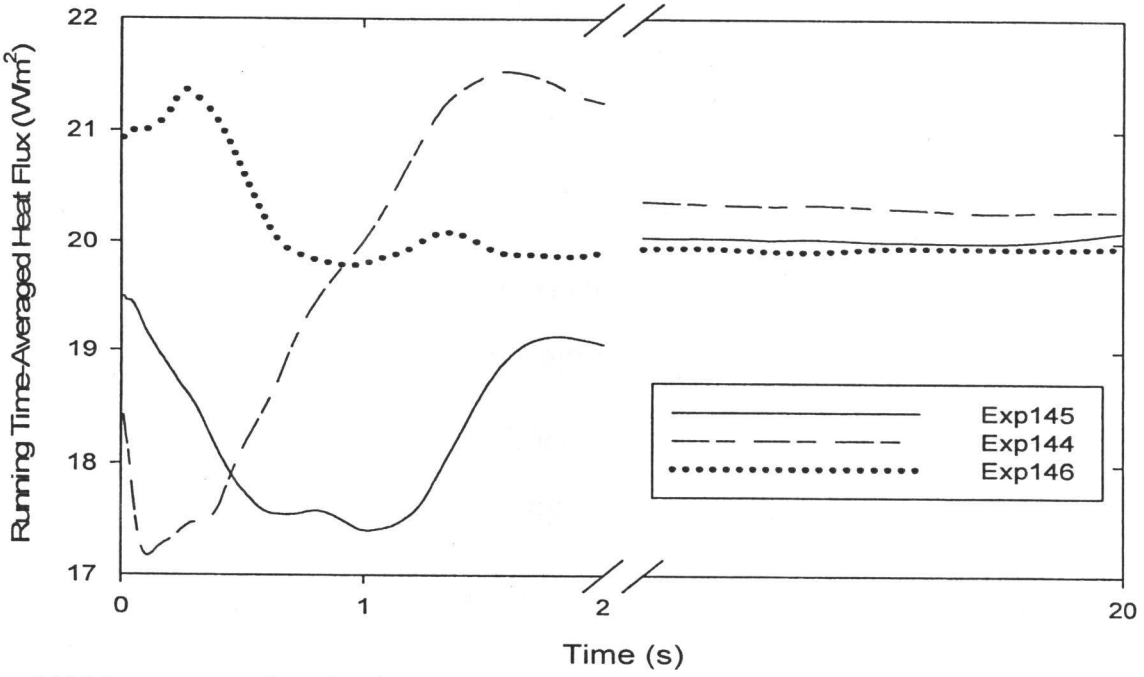

Figure 4.13 Measurements of running time-averaged heat flux of the same location for t = 20s. the interval between 2 and 18 second is broken off. ($Ra = 2.8 \times 10^5$, A =17.3, y/H = 0.27).

One possible reason for the slightly low results has been identified. To measure convective heat transfer in this thesis, the fringe spacing was measured. It was the basis for calculating the heat flux and Nusselt number. Near the surface, the fringe intensity data tends to be noisy, in part because of diffraction fringes caused by the surface. So, to have less noisy fringe intensity data, the measurements were not done at the surface. Measurements were taken bit further from the wall. In this region, the convection heat transfer is slightly lower than at the surface. In the future, to rectify this problem, the measurements should be done as close as possible to the walls. However, to get closer to the wall, better regression and image enhancement techniques will be needed to reduce the noise effectively.

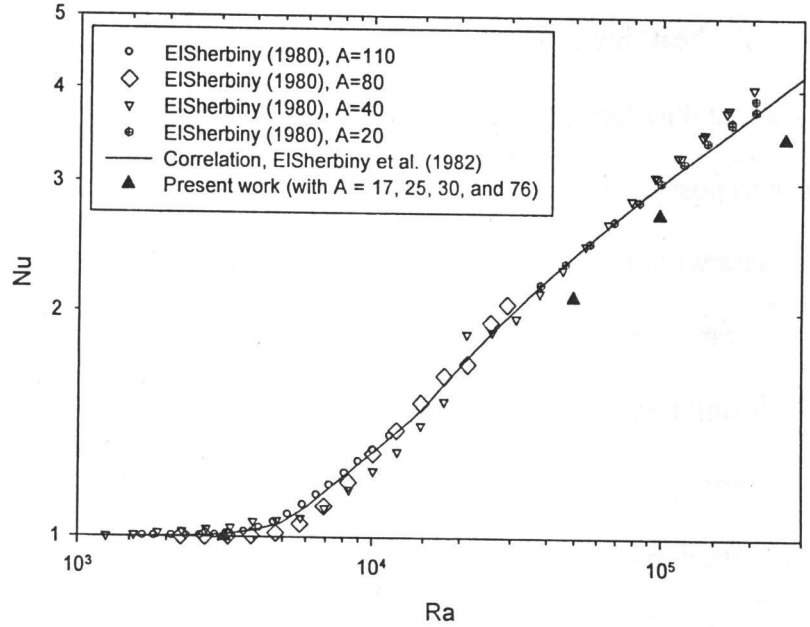

Figure 4.14 Comparison of present work results with ElSherbiny experiments and his design correlation.

4.5 Recent Improvements to the Experimental Method

Over the course of the research done for this thesis, the experimental procedure and the image analysis methods were constantly being improved. This section describes some very recent improvements, and presents a small sample of improved results. Because of time constraints, it was not practical to repeat all of the experiments with these improved methods.

Another set of experiments was conducted for the most turbulent conditions inside the cavity (the highest Rayleigh number). To improve the implementation of the experiments the following changes were made:

1. Two new regressions were developed: i) reglow.m was developed to measure the heat flux in low heat transfer locations (i.e., lower regions of the cold wall) and ii) regression8.m was developed to measure the heat transfer as close as possible to the walls.
2. The camera was mounted on a precision x-y-z positioning, shown in Figure 4.15. The camera could be translated in all three axes with resolution of 0.1 mm. This unit allowed the y-location of the measurements to be determined more accurately.
3. The data filtering of the calculated instantaneous heat flux values (Section 3.6.1) was changed. In the new filtering method, the time-average of the previous measurements was calculated. The next measurement was checked with the previous time-averaged measurements. If the current measurement

was either bigger than 1.5 or lower than 0.5 times of the average it was replaced with the average.

4. The method used to filter the images (Section 3.5.1) was changed. Rather than using a constant kernel for the median filter of 15x15, the size of the median filter varied with the fringe spacing. It was found that the suitable size for the median filter kernel was the fringe spacing (expressed in number of pixels) divided by 6. This number was then rounded to the nearest odd integer.
5. Prior to heating the model, the optics were adjusted to give four finite fringes in the output. This was reduced from ten fringes in order to decrease the uncertainty of the measurements, as will be discussed in Appendix B.
6. The fluorescent lights were turned off during the image capturing. It was found, after running most of the tests that darkening the test room significantly reduced the noise in the images. Also, the noise in the image caused by the electrical interference seemed to be reduced.

Figure 4.16 shows the running time-averaged and instantaneous heat flux for one set of improved results. As a result of the improvements, the instantaneous plots have much lower noise levels. Compared Figure 4.17 with the old results given in Figure 4.12, it can be seen that the high frequency noise has been greatly reduced. The new plot is much smoother. Most of the fluctuations are due to the actual heat flux changes caused by turbulence.

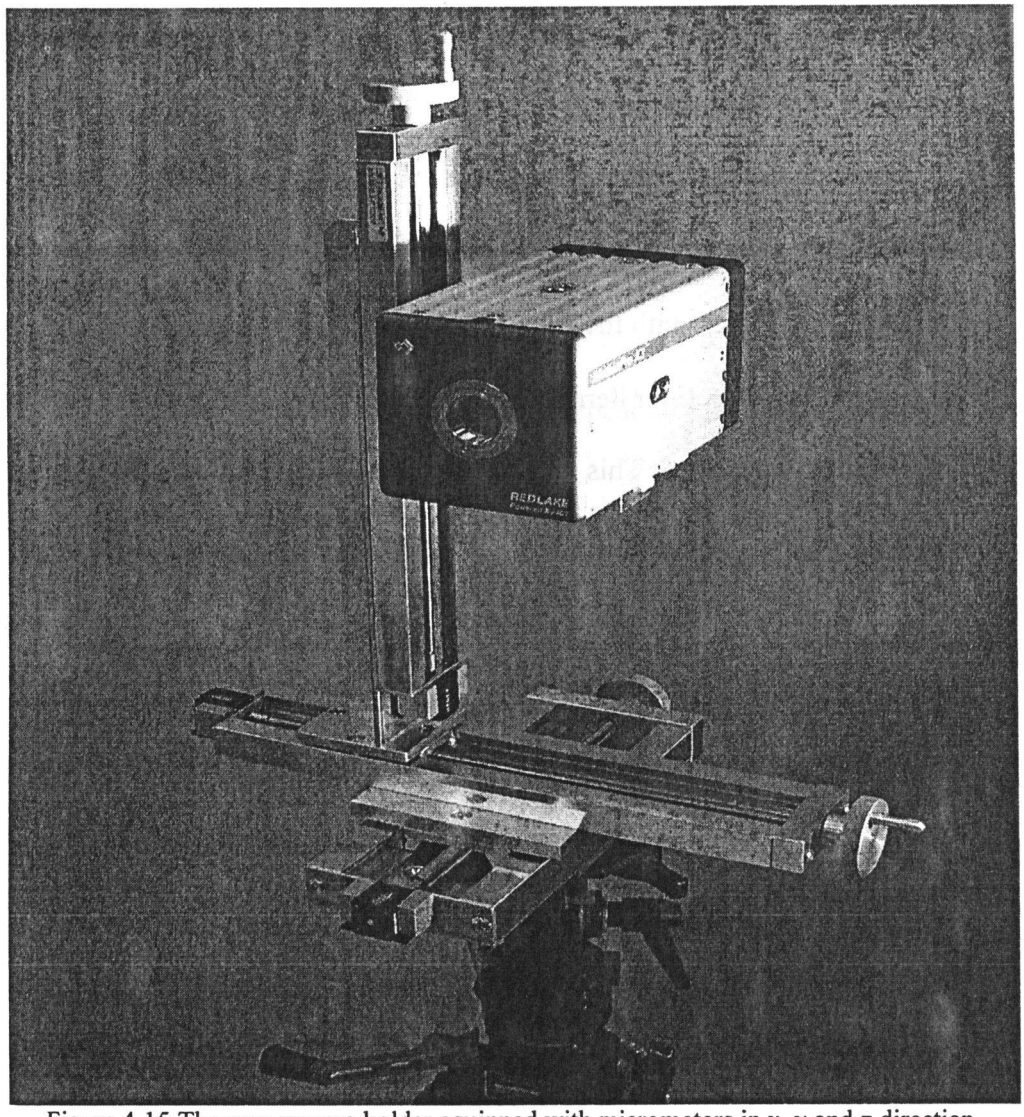

Figure 4.15 The new camera holder equipped with micrometers in x, y and z direction.

Figure 4.17 shows the time-averaged Nusselt number variation over the hot and cold wall surfaces. These improved results are much closer to the experimental data in the literature. The spatial averaging of these data produces $\overline{Nu}_{avg}$ = 3.92, which is only 2.3% lower than the prediction from the ElSherbiny correlation.

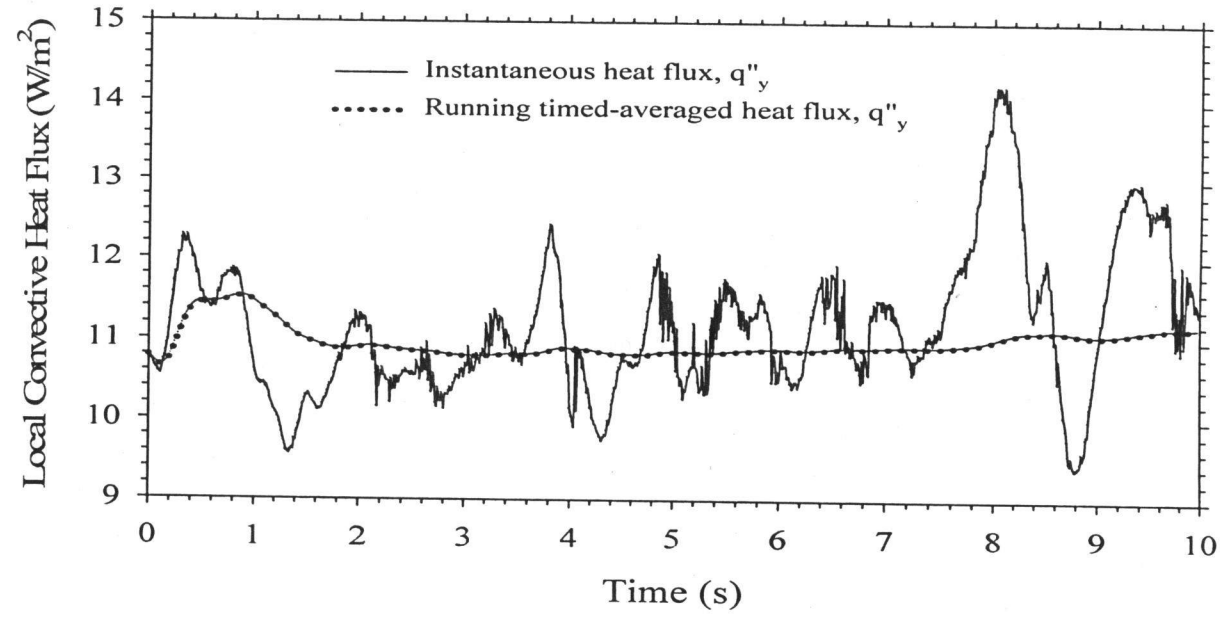

Figure 4.16 Instantaneous and Running time-averaged heat flux (Exp. 135, Ra =2.9x10^5, A =17.3, y/H = 0.14).

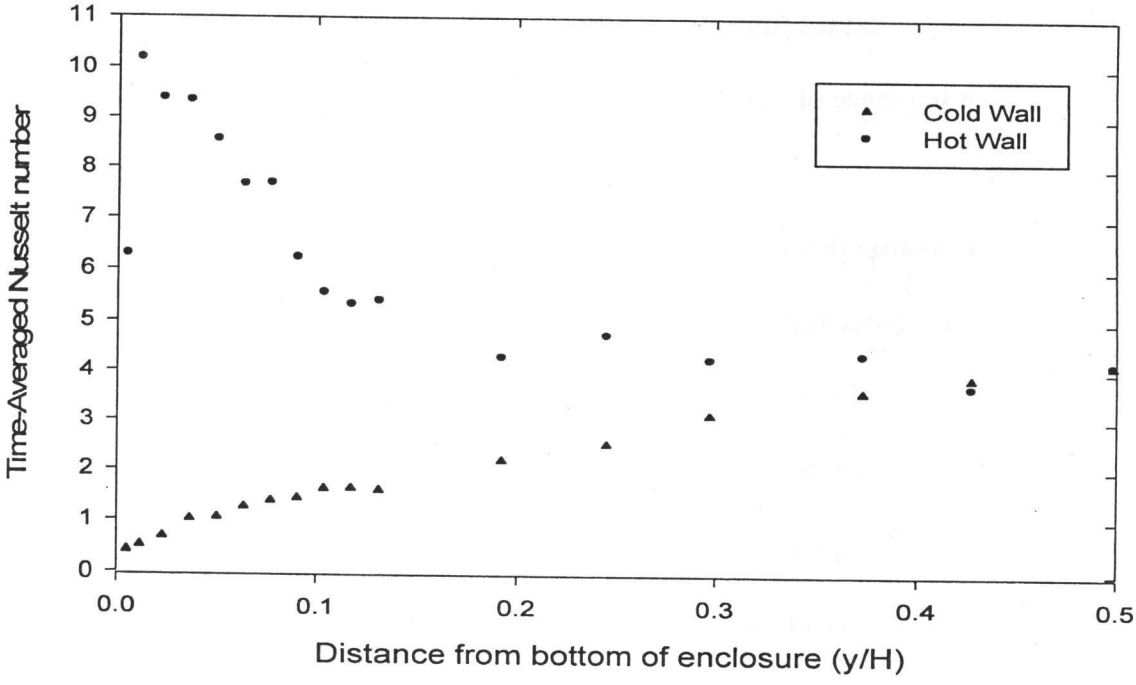

Figure 4.17 Time-averaged local Nusselt number ($\overline{Nu}_y$) distribution on the enclosure walls (Ra$_m$ = 2.85x10^5).

CHAPTER 5: CONCLUSIONS AND RECOMMENDATIONS

5.1 Conclusions

A time-averaging technique was used to measure the turbulent convective heat transfer rates in a tall vertical cavity. The local heat transfer rates were measured at four wall spacings. More than 146 sets of experiments were conducted. Each set of experiments was composed of at least 1000 interferograms. The main conclusions of this research are summarized below:

- A high speed camera can be used in conjunction with a Mach-Zehnder interferometer to successfully measure turbulent free convective heat transfer. It has been shown that the time-averaged heat transfer rate can be measured by analyzing a sequence of interferograms using an automated image processing technique.
- For the convection problem considered in this thesis, it has been shown that an image capture frequency of 100Hz with a total capture time of about ten seconds is sufficient to obtain an accurate time-averaged heat flux. Of course, for different test geometries and experimental conditions this requirement will likely change.
- Measurements of the spatial average Nusselt number in the enclosure were found to compare well with results from the literature. However, in general, measurements using the current technique were slightly lower than the accepted

values in the literature. Some of the reasons for these low measurements have been identified and corrected.

- To get accurate local heat transfer coefficients in turbulent conditions, it is important that the fringe gradient measurement be made as close to the surface as possible. This is more critical than in laminar flow, because, in turbulent conditions, the temperature gradient decreases faster with increasing distance from the surface.

5.2 Recommendations

The following recommendations are made for future research:

- For any new application, it is recommended that the first step be the determination of the required capture frequency and time interval. The procedures for doing this are outlines in this thesis.
- In future work, a stepping motor or micrometer should be used to measure the exact y-value of each experiment. This could be automated and automatically fed to the experiment data file. This improvement has already been partly implemented.
- To have better accuracy, the finite fringe spacing (d) in the unheated model should be adjusted as large as possible e.g., 4 or 5 fringes in each image.
- Care should be taken to turn off any electrical lights that produce noise on the captured images. The test room should be dark during the capturing.

- This project could be carried out by a team. Besides the mechanical engineer, the expertise of a statistician and image processing specialist is needed.

APPENDIX A: DEVELOPED COMPUTER PROGRAMS

A1 Introduction

All of the MATLAB routines that were developed as part of this thesis, along with instructions, are gathered in this appendix. They are categorized as: (i) image processing, and (ii) calculation codes. Most of the image processing codes were reserved words in MATLAB software, but calculation codes use the equations derived or extracted from textbooks or references. These codes were combined together to measure free convective heat transfer in the cavity.

A2 Images Processing and Calculation Codes

A2.1 Pressure.m

Application: This file gets the room pressure and temperature in mmHg and degree centigrade respectively, and calculates corrected pressure. Corrections are based on Toronto latitude and mercury expansion due to the room temperature.

Code:

```
function [Pcorr] = Pressure(P,T)
Plat = -0.000234;
PMult(18) = -0.002932;
PMult(19) = -0.003094;
PMult(20) = -0.003256;
PMult(21) = -0.003418;
PMult(22) = -0.003580;
PMult(23) = -0.003743;
PMult(24) = -0.003905;
PMult(25) = -0.004012;
T1 = round(T);
T2 = T1 +1;

Ptemp = P+(T - T2)/(T1 - T2)*(PMult(T1)-PMult(T2))+PMult(T2)+Plat;
```

```
Pcorr = Ptemp*133.32239;
end
```

Process:

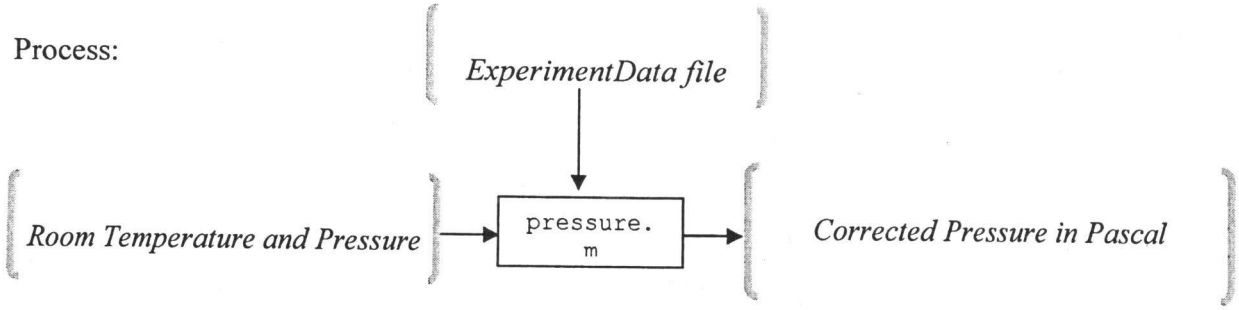

A2.2 regression.m

Application: This file gets the line scan profile and calculates spacing between fringes in pixel.

Code:

```
function spacing = regression(cx,cy,c)
ln=[cx,cy,c];
N=length(ln);
% Extracts the average intensity for entire scan length
avI=mean(c);
% Find the mean intensity crossings
% Initialize counters
xings=0;
xi=[];
for i=1:N-1
    if ln(i,3)<avI && ln(i+1,3)>avI
        xings=xings+1;
        xi(xings)=i;
    end
    if ln(i,3)>avI && ln(i+1,3)<avI
        xings=xings+1;
        xi(xings)=i;
    end
end
%Extract data for one period
for i=xi(1):xi(3)
    j=i-xi(1)+1;
    period(j,1)=ln(i,1);
    period(j,2)=ln(i,3);
end
% Compute revised mean intensity based on one period of fringe data
Avgnew=mean(period);
% Extracts the average intensity -- the mean value of column 2
avI=Avgnew(2);
% Initial guesses for regression parameters
P=(2*pi)/(xi(3)-xi(1));
P1=P;
Pold=0.0;
% phase angle
```

```
if period(1,2)<period(2,2)
    phi=0.0;
end
if period(1,2)>period(2,2)
    phi=3.1415;
end
% Estimate Amplitude
Imax=max(period);
Imin=min(period);
A=(Imax(2)-Imin(2))/2.0;
M=length(period);
%Outer/Outer Regression Loop (P and phi)
count3=0;
stop3=0;
while stop3==0 && count3<100
    % This is the outer for loop for phi regression
    stop=0;
    count1=0;
    dEold=0;
    while stop==0 && count1<7000
        % Compute the baseline sum square error (Ebase)
        Ebase=0.0;
        for k=1:M
            Ifit=avI+A*sin(P*(period(k,1)-period(1,1))+phi);
            Diff2=(Ifit-period(k,2))^2.;
            Ebase=Ebase+Diff2;
        end
        % Increment the phase angle and recompute the sum sq. error
(Ephi)
        dphi=0.0005;
        phi2=phi+dphi;
        Ephi=0.0;
        for k=1:M
            Ifit=avI+A*sin(P*(period(k,1)-period(1,1))+phi2);
            Diff2=(Ifit-period(k,2))^2.;
            Ephi=Ephi+Diff2;
        end
        % Store the old value of dEdphi (for sign change test)
        dEdphi=(Ephi-Ebase)/dphi;

        if dEdphi > 0
            phi=phi-dphi;
        end
        if dEdphi < 0
            phi=phi+dphi;
        end
        if dEold<0 && dEdphi>0
            stop=1;
        end
        if dEold>0 && dEdphi<0
            stop=1;
        end
        count1=count1+1;
        dEold=dEdphi;
    end
    % end of outer for loop for regression of phi
    % start of outer loop for regression of P
```

```
    stop=0;
    count2=0;
    dEold=0;
    while stop==0 && count2<1500
        %   Compute the baseline sum square error (Ebase)
        Ebase=0.0;
        for k=1:M
            Ifit=avI+A*sin(P*(period(k,1)-period(1,1))+phi);
            Diff2=(Ifit-period(k,2))^2.;
            Ebase=Ebase+Diff2;
        end
        dP=P1/1000.;
        P2=P+dP;
        EP=0.0;
        for k=1:M
            Ifit=avI+A*sin(P2*(period(k,1)-period(1,1))+phi);
            Diff2=(Ifit-period(k,2))^2.;
            EP=EP+Diff2;
        end
        %
        dEdP=(EP-Ebase)/dP;
        if dEdP > 0
            P=P-dP;
        end
        if dEdP < 0
            P=P+dP;
        end
        %
        if dEold<0 && dEdP>0
            stop=1;
        end
        if dEold>0 && dEdP<0
            stop=1;
        end
        count2=count2+1;
        dEold=dEdP;
    end
% end of P regression loop
    count3=count3+1;
    deltaP=abs(P-Pold);
    if deltaP<=dP
        stop3=1;
    end
    Pold=P;
end

spacing=2*3.14159/P;
```

Process:

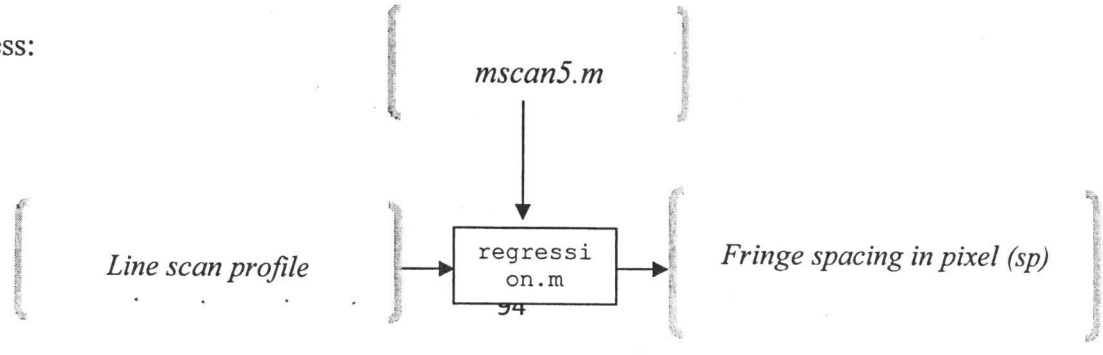

A2.3 read.m

Application: This file brings up the first image to measure the wall, start and end points of scanning, w1, x1 and x2, respectively. The image would be rotated 180 degree if wall B is subjected to measurement. The median filter of 5 is used on this image. Extension of the images is considered as TIF.

Code:

```
clc

clear
tic
load ExperimentData
expnum = input('Enter experiment number [1 2 3 ... ]:  ');
AB = ExperimentData(7,expnum);
if AB==0
    phi = 0;
else
    phi = 180;
end
S = ExperimentData(8,expnum);
N=1;
Pd=.006935;
fps = ExperimentData(2,expnum);
i=0;
s=num2str(i, '%06.0f');
J = imread(['Exp',int2str(fps),'/ImgA',s,'.TIF']);
I=medfilt2(J,[5 5]);
I=imrotate(I,phi,'bilinear');
imtool(I);
toc
```

Process:

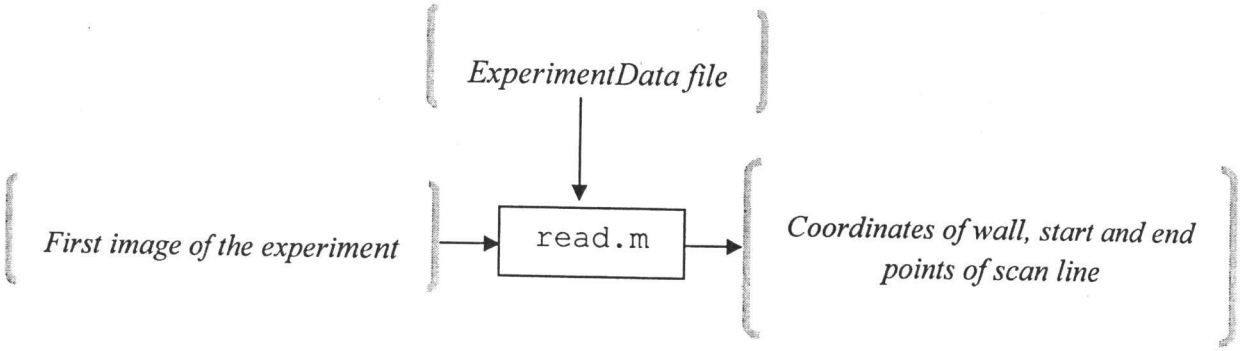

A2.4 Rayleigh.m

Application: This file gets the data from ExperimentData file and calculates Rayleigh number for each experiment. It saves the result in 15th row of the ExperimentData file.

Code:

```
load ExperimentData
for xx = 1:110
    P = ExperimentData(12,xx);
    Tinf = ExperimentData(11,xx);
    Th = ExperimentData(10,xx);
    Tc = ExperimentData(9,xx);
    w = ExperimentData(3,xx);
    %function [Ra] = Rayleigh(P,Tinf,Th,Tc,w)
    R = 287;m=0;n=0;o=0;l = 0;
    dT = Th-Tc;
    Tf = ((Th+Tc)/2)+273.15;
    beta = 1/Tf;
    g = 9.806;
    L = w/1000;
    kf = ThermalConductivity(Tf);
    mu = DynamicViscosity(Tf);
    cp = SpecificHeat(Tf);
    Pcorr = Pressure(P,Tinf);
    rho = Pcorr/(R*Tf);
    ExperimentData(15,xx) = g*beta*(dT)*L^3*rho^2*cp/(mu*kf);
end
```

Process:

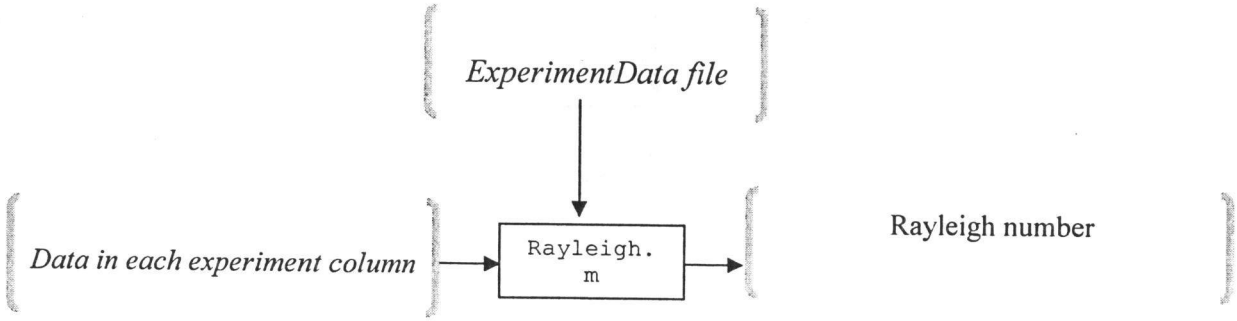

A2.5 Table.m

Application: This file gathers data from HTResult table. Data with the value of bigger than (1+m)*Q and less than (1-m)*Q are filtered. Where, m is defined in Section 3.7. Then all data are arranged in new table (Table1) to be used for further analysis. This table is saved in experiment directory and goes to FTable file for next process.

Code:

```
clc
clear
load ExperimentData
xx= input('Enter experiment number      ');
nn = ExperimentData(6,xx);
fps = ExperimentData(2,xx);
t = 1/fps;
for i =0:nn-1
    load(['Exp',int2str(fps),'/',int2str(i),'/HTResult']);
    Table1(i+1,1) = t*i;
    Table1(i+1,2) = abs(HTResult(1,2));
    Table1(i+1,4) = abs(HTResult(1,4));
    Table1(i+1,3) = abs(HTResult(1,3));
    Table1(i+1,5) = abs(HTResult(1,1));
    %Table1(i+1,5) = HTResult(1,9);
end
Q = mean(Table1(:,2));
H = mean(Table1(:,3));
NU = mean(Table1(:,4));
m = 4*std(Table1(:,2));
nm = 4*std(Table1(:,4));
hm = 4*std(Table1(:,3));
for kk=1:nn
    if (Table1(kk,2)>(1+m)*Q || Table1(kk,2)<(1-m)*Q)
        Table1(kk,2)= Q ;save(['Exp',int2str(fps), '/ImNu+1'],'kk');end
    if (Table1(kk,3)>(1+hm)*H || Table1(kk,3)<(1-hm)*H)
        Table1(kk,3) = H;end
    if (Table1(kk,4)>(1+nm)*NU || Table1(kk,4)<(1-nm)*NU)
        Table1(kk,4) = NU;
    end
end
save(['Exp',int2str(fps), '/Table1'],'Table1')
FTable;
```

Process:

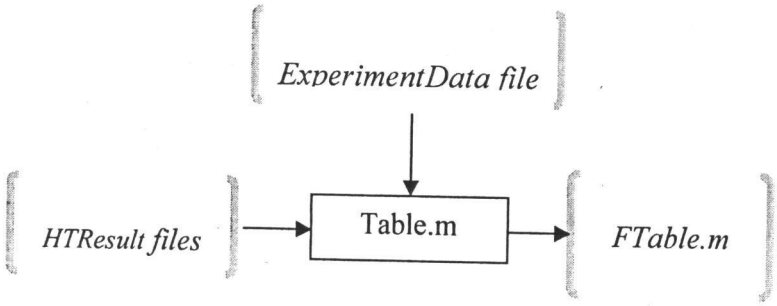

A2.6 MakePlots.m

Application: This file gets data from tables Table1and FTable1 to plot the time versus heat flux, Nusselt number and fringe spacing in three different plots.

Code:

```
load ExperimentData
expnum = input('Enter experiment number [1 2 3 ... ]:  ');
fps = ExperimentData(2,expnum);AB = ExperimentData(7,expnum);
load(['Exp',int2str(fps), '/Table1'])
load(['Exp',int2str(fps), '/FTable1'])
x = FTable1(1,2);
y = FTable1(1,4);
z = FTable1(3,2);
sd = FTable1(2,2);
[nn mm] = size (Table1);
time = Table1(:,1);
qflux = Table1(:,2);
Nu = Table1(:,4);
h = Table1(:,3);
sp = Table1(:,5);
Pt = plot(time,qflux,'-');
set(Pt,'LineWidth',1)
xlabel('Time in Second')
ylabel('Heat Flux (W/M^2)')
title(sprintf(' Number of the pictures =%g, experiment # %g, average
value of q"=%g, The average Nu = %g,Scattering =%g percent, SD=%g;Wall
%g', nn, expnum,x,y,z,sd,AB))
legend('q"');figure
plot(time,Nu,'-o')
xlabel('Time in Second')
ylabel('Nu')
legend('Nusselt Number');figure
Pt = plot(time,sp,'-');
set(Pt,'LineWidth',1)
xlabel('Time in Second')
ylabel('Peak to peak (in pixel)')
legend('Spacing');
```

Process:

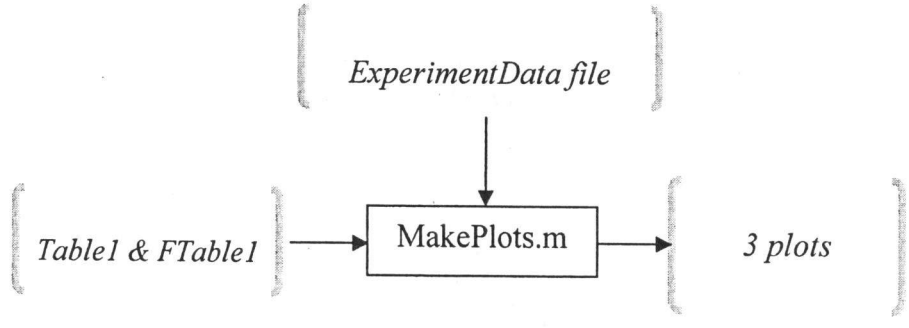

A2.7 fpsStep.m

Application: This file takes the running time average of data in Table1 using trapezoidal rule. Each time step is the reciprocal of frequency of capturing pictures (t = 1/fps). The average of each run is saved in XTable1 table and average of each column in XTable1 is saved in SXTable. Both tables are saved in experiment directory.

Code:

```
clc
clear
tic
load ExperimentData
xx= input('Enter experiment number      ');
nn = ExperimentData(6,xx);
fps = ExperimentData(2,xx);
load(['Exp',int2str(fps),'/Table1']);
for mm = 2:nn
    for i =1:mm
        XTable1(i,1) = Table1(i,1);
        XTable1(i,2) = Table1(i,2);
        XTable1(i,4) = Table1(i,4);
        XTable1(i,3) = Table1(i,3);
    end
    [Nht Mht]=size(XTable1);
    t = XTable1(:,1);
    q = XTable1(:,2);
    h = XTable1(:,3);
    Nu = XTable1(:,4);
    qf = trapz(t,q)/(XTable1(Nht,1));
    hf = trapz(t,h)/(XTable1(Nht,1));
    Nuf = trapz(t,Nu)/(XTable1(Nht,1));
    SXTable(mm-1,1) = XTable1(Nht,1);
    SXTable(mm-1,2) = qf;
    SXTable(mm-1,3) = hf;
    SXTable(mm-1,4) = Nuf;
end
save(['Exp',int2str(fps), '/SXTable'],'SXTable')
save(['Exp',int2str(fps), '/XTable1'],'XTable1')
```

Process:

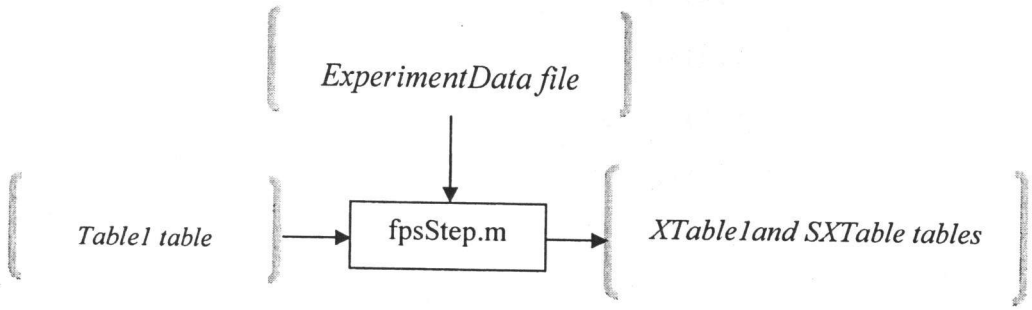

A2.8 stat.m

A.2.8 Filename: stat.m

Application: This file takes the data from Table1 and count the number of data between mean value and $\pm 2.5\sigma$ in each interval of 0.25σ. Standard deviation is $\sigma = \frac{\sum_{i=1}^{1000}(x_m - x_i)^2}{1000}$ where x_m is the mean value of instantaneous calculations. Finally it plots standard deviation versus number of data

Code:

```
load ExperimentData
xx= input('Enter experiment number      ');
nn = ExperimentData(6,xx);
fps = ExperimentData(2,xx);AB = ExperimentData(7,xx);
load(['Exp',int2str(fps), '/Table1'],'Table1')
n = 0;m=0;l=0;o=0;z=0;nm=0; mm=0;lm=0;om=0;zm=0;
n1 = 0;m1=0;l1=0;o1=0;z1=0;nm1=0; mm1=0;lm1=0;om1=0;zm1=0;
q = mean(Table1(:,2));
zig = std(Table1(:,2));
for iii = 1:nn
    if Table1(iii,2)<q+.25*zig && Table1(iii,2)>q
        n = n+1;
    elseif Table1(iii,2)<q+.5*zig && Table1(iii,2)>q+.25*zig
        m = m +1;
    elseif Table1(iii,2)<q+.75*zig && Table1(iii,2)>q+.5*zig
        l = l+1;
    elseif Table1(iii,2)<q+zig && Table1(iii,2)>q+.75*zig
        o = o+1;
    elseif Table1(iii,2)<q+1.25*zig && Table1(iii,2)>q+zig
        z = z+1;
    elseif Table1(iii,2)<q+1.5*zig && Table1(iii,2)>q+1.25*zig
        nm = nm+1;
    elseif Table1(iii,2)<q+1.75*zig && Table1(iii,2)>q+1.5*zig
        mm = mm+1;
    elseif Table1(iii,2)<q+2*zig && Table1(iii,2)>q+1.75*zig
        lm = lm+1;
    elseif Table1(iii,2)<q+2.25*zig && Table1(iii,2)>q+2*zig
        om = om+1;
    elseif Table1(iii,2)<q+2.5*zig && Table1(iii,2)>q+2.25*zig
        zm = zm+1;
    elseif Table1(iii,2)<q && Table1(iii,2)>q-.25*zig
        n1 = n1+1;
    elseif Table1(iii,2)<q-.25*zig && Table1(iii,2)>q-.5*zig
        m1 = m1 +1;
    elseif Table1(iii,2)<q-.5*zig && Table1(iii,2)>q-.75*zig
        l1 = l1+1;
    elseif Table1(iii,2)<q-.75*zig && Table1(iii,2)>q-zig
        o1 = o1+1;
    elseif Table1(iii,2)<q-zig && Table1(iii,2)>q-1.25*zig
        z1 = z1+1;
    elseif Table1(iii,2)<q-1.25*zig && Table1(iii,2)>q-1.5*zig
        nm1 = nm1+1;
    elseif Table1(iii,2)<q-1.5*zig && Table1(iii,2)>q-1.75*zig
```

```
        mm1 = mm1+1;
    elseif Table1(iii,2)<q-1.75*zig && Table1(iii,2)>q-2*zig
        lm1 = lm1+1;
    elseif Table1(iii,2)<q-2*zig && Table1(iii,2)>q-2.25*zig
        om1 = om1+1;
    elseif Table1(iii,2)<q-2.25*zig && Table1(iii,2)>q-2.5*zig
        zm1 = zm1+1;
    end
end
 time = [-2.5 -2.25 -2 -1.75 -1.5 -1.25 -1 -.75 -.5 -.25 .25 .5 .75 1
1.25 1.5 1.75 2 2.25 2.5];
 qflux= [zm1 om1 lm1 mm1 nm1 z1 o1 l1 m1 n1 n m l o z nm mm lm om zm];
%time = [-2.5 -2 -1 1 2 2.5];
%qflux= [om1+zm1 z1+nm1+mm1+lm1 n1+m1+l1+o1 n+m+l+o z+nm+mm+lm om+zm];
Pt = plot(time,qflux,'-');
set(Pt,'LineWidth',1)
grid
xlabel('Standard Deviation')
ylabel('Number of data')
X = n+m+l+o+z+nm+mm+lm+om+zm+n1+m1+l1+o1+z1+nm1+mm1+lm1+om1+zm1;
title(sprintf('The distribution of q-value for %g pictures out of %g
specimens for experiment #%g;Wall %g', X,nn,xx,AB))
%axis([0,20,-33,-32])
legend('Distribution of q"');
```

Process:

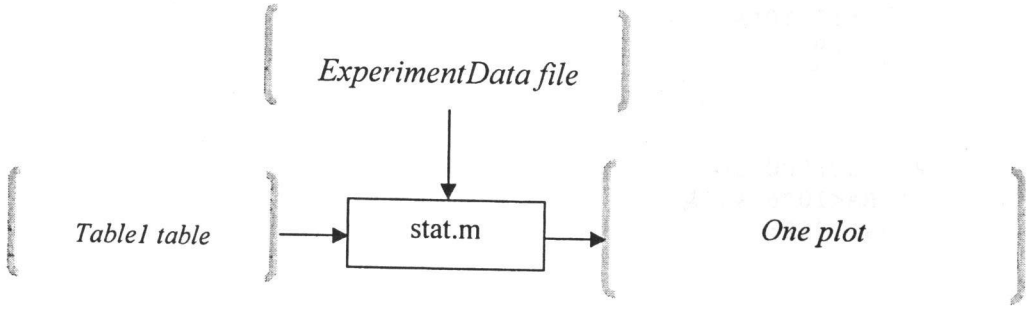

A2.9 Nusselt.m

Application: This is a function that takes Ra and A and calculate ElSherbiny correlation, 1980, (Nu); Bairi correlation, 2008, (Nu1); Nader (Nu2) and Wright, 1996, (Nu3) correlation.

Code:

```
function [Nu Nu1 Nu2 Nu3] = Nusselt(Ra,A)
if (A == 5 && Ra<10^8)
    aa = .193*Ra^.25;
    bb = 1+(1800/Ra)^1.289;
    Nu = max([(1+(aa/bb)^3)^.33333,.0605*Ra^.33333]);
elseif (A == 10 && Ra<9.7*10^6)
    Nu = max([ (1+(.125*Ra^.28)^9)^(1/9),.061*Ra^.33333]);
elseif (A == 20 && Ra<2*10^6)
    Nu = (1+(.064*Ra^.33333)^6.5)^(1/6.5);
elseif (A == 40 && Ra<2*10^5)
    Nu = (1+(.0303*Ra^.402)^11)^(1/11);
elseif (A == 80 && Ra<3*10^4)
    Nu = (1+(.0227*Ra^.438)^18)^(1/18);
elseif (A == 110 && Ra<1.2*10^4)
    Nu = (1+(.0607*Ra^.33333)^18)^(1/18);
else
    Nu1 = .0605* Ra^.33333;
    a = .104*Ra^.293;
    b = 1 + (6310/Ra)^1.36;
    Nu2 = (1+(a/b)^3)^.33333;
    Nu3 = .242*(Ra/A)^.272;
    Nu = max([Nu1,Nu2,Nu3]);
end
%for Ra between 1000 and 10^10 Ref.9 (Bairi)
if (Ra>1000 && Ra<10^10&& A==1)
    Nu1 = .15*Ra^.29;
else
    Nu1 = 0;
end
% for Ra between 50,000 and 10^6 Ref.11 (Nader)
if (Ra>50000 && Ra<10^6 && A==9)
    Nu2 = .178*Ra^.252;
else
    Nu2 = 0;
end
% Wright new correlation [76]
if (Ra<10^6&& A>=40)
    if Ra>50000
        Nu3 = 0.0673838*Ra^.3333;
    elseif (Ra>10000 && Ra<= 50000)
        Nu3 = 0.028154*Ra^.4134;
    else
        Nu3 = 1+ (1.75967*10^(-10))*Ra^2.2984755;
    end
else
    Nu3 = 0;
end
```

A2.10 iterate.m

Application: This is the main file that brings up all images from each directory to measure the q", Nu and h. This file feeds mscan.m with median filtered (using 15 by 15 matrix) images and save measured parameters in SaveScale file. If images were taken on wall B they would be rotated 180 degree before being fed to mscan5 too.

Code:

```
tic
load ExperimentData
fps = ExperimentData(2,expnum);
SaveScale
nm = input('Would you like to see the scan?(enter 1 or any) Yes=1 &
No=any number   ');
if nm == 1
    n = input('How many (less than 20) directories would you like to
make?');
else
    n = ExperimentData(6,expnum);
end
n=n-1;
for imgnum=0:n
    s=num2str(imgnum, '%06.0f');
    J=imread(['Exp',int2str(fps),'/',int2str(imgnum),'/imgA',s,
'.TIF']);
    I=medfilt2(J,[15 15]);
    I=imrotate(I,phi,'bilinear');
    mscan5
end
toc
```

Process:

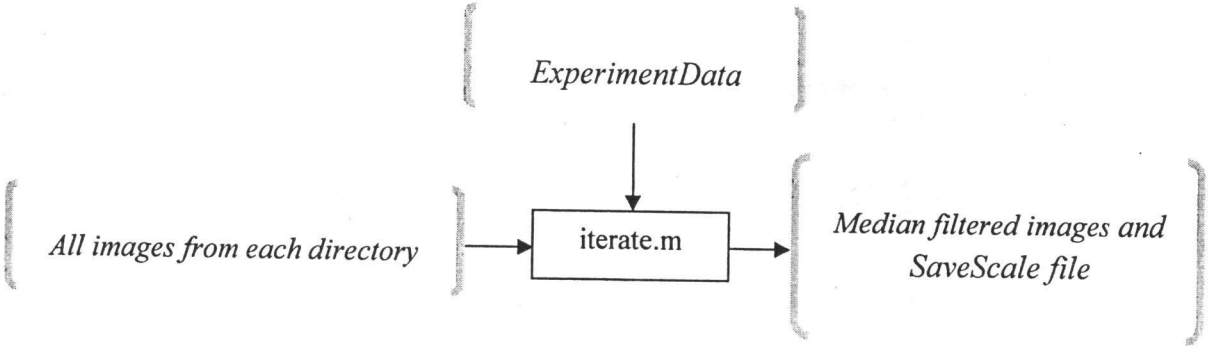

A2.11 regression8.m

Application: This function acts the same as the regression.m does. This version of the routine is improved in the way that it selects the closest possible points to the wall each time.

Code:

```
% This function receives the line intensity matrix [cx,cy,c]
% and fits a sine curve to the data using nonlinear regression.
% The function returns the unscaled fringe spacing, corresponding to a
% shift of one fringe order (e.g. constructive peak to constructive
peak
% OR destructive peak to destructive peak).
%
%This function is an improvement over regression5, in that the average
%intensity is adjusted (avI) to get the best fit. This turns out to
%make no difference to the calculated value of P, in most cases.
%
function spacing = regression8(cx,cy,c)
ln=[cx,cy,c];
N=length(ln);
% Extracts the average intensity for entire scan length
avI=mean(c);
% Find the mean intensity crossings
% Initialize counters
xings=0;
xi=[];
%
for i=1:N-1
    if ln(i,3)<avI && ln(i+1,3)>avI
        xings=xings+1;
        xi(xings)=i;
    end
    if ln(i,3)>avI && ln(i+1,3)<avI
        xings=xings+1;
        xi(xings)=i;
    end
end
%Extract data for one period
xend=xi(3)-xi(1)+3;
for i=1:xend
    period(i,1)=ln(i,1);
    period(i,2)=ln(i,3);
end
%
% Compute revised mean intensity based on one period of fringe data
Avgnew=mean(period);
% Extracts the average intensity -- the mean value of column 2
avI=Avgnew(2);
% Initial guesses for regression parameters
P=(2*pi)/(xi(3)-xi(1));
P1=P;
Pold=0.0;
% Initial Phase Angle
c1=xi(1);
c1p1=xi(1)+1;
```

```
    if period(c1,2)<period(c1p1,2)
    phi=0.0;
    end
    if period(c1,2)>period(c1p1,2)
    phi=3.1415;
    end
% Initial Estimate of Amplitude
Imax=max(period);
Imin=min(period);
A=(Imax(2)-Imin(2))/2.0;
M=length(period);
%
%Outer/Outer Regression Loop (P and phi)
count3=0;
stop3=0;
        while stop3==0 && count3<100
% This is the outer for loop for phi regression
stop=0;
count1=0;
dEold=0;
while stop==0 && count1<7000
% Compute the baseline sum square error (Ebase)
    Ebase=0.0;
        for k=1:M
        Ifit=avI+A*sin(P*(period(k,1)-period(1,1))+phi);
        Diff2=(Ifit-period(k,2))^2.;
        Ebase=Ebase+Diff2;
        end
%
% Increment the phase angle and recompute the sum sq. error (Ephi)
dphi=0.0005;
phi2=phi+dphi;
Ephi=0.0;
        for k=1:M
        Ifit=avI+A*sin(P*(period(k,1)-period(1,1))+phi2);
        Diff2=(Ifit-period(k,2))^2.;
        Ephi=Ephi+Diff2;
        end

% Store the old value of dEdphi (for sign change test)
dEdphi=(Ephi-Ebase)/dphi;

    if dEdphi > 0
       phi=phi-dphi;
    end
    if dEdphi < 0
       phi=phi+dphi;
    end
        if dEold<0 && dEdphi>0
        stop=1;
        end
        if dEold>0 && dEdphi<0
        stop=1;
        end
count1=count1+1;
dEold=dEdphi;
end
```

```
% end of outer for loop for regression of phi
%
% start of outer loop for regression of P
stop=0;
count2=0;
dEold=0;
while stop==0 && count2<1500
%    Compute the baseline sum square error (Ebase)
     Ebase=0.0;
     for k=1:M
     Ifit=avI+A*sin(P*(period(k,1)-period(1,1))+phi);
     Diff2=(Ifit-period(k,2))^2.;
     Ebase=Ebase+Diff2;
     end

%
% Increment the phase angle and recompute the sum sq. error (Ephi)
dP=P1/1000.;
P2=P+dP;
EP=0.0;
     for k=1:M
     Ifit=avI+A*sin(P2*(period(k,1)-period(1,1))+phi);
     Diff2=(Ifit-period(k,2))^2.;
     EP=EP+Diff2;
     end
%
dEdP=(EP-Ebase)/dP;
     if dEdP > 0
        P=P-dP;
     end
     if dEdP < 0
        P=P+dP;
     end
%
     if dEold<0 && dEdP>0
         stop=1;
         end
         if dEold>0 && dEdP<0
         stop=1;
         end
         count2=count2+1;
         dEold=dEdP;
end
% end of P regression loop
% Start of loop for regression of Iav
stop=0;
countavI=0;
dEold=0;
while stop==0 && countavI<50
%    Compute the baseline sum square error (Ebase)
     Ebase=0.0;
     for k=1:M
     Ifit=avI+A*sin(P*(period(k,1)-period(1,1))+phi);
     Diff2=(Ifit-period(k,2))^2.;
     Ebase=Ebase+Diff2;
     end
%
```

```
% Increment the avI and recompute the sum sq. error (EavI)
davI=A/500.;
avI2=avI+davI;
EavI=0.0;
    for k=1:M
    Ifit=avI2+A*sin(P*(period(k,1)-period(1,1))+phi);
    Diff2=(Ifit-period(k,2))^2.;
    EavI=EavI+Diff2;
    end
%
dEdavI=(EavI-Ebase)/davI;
    if dEdavI > 0
       avI=avI-davI;
    end
    if dEdavI < 0
       avI=avI+davI;
    end
%
        if dEold<0 && dEdavI>0
        stop=1;
        end
        if dEold>0 && dEdavI<0
        stop=1;
        end
        countavI=countavI+1;
        dEold=dEdavI;
  end
% end of avI regression loop
count3=count3+1;
deltaP=abs(P-Pold);
        if deltaP<=dP
           stop3=1;
        end
Pold=P;
% outer "while" end statement
                    end
spacing=2*3.14159/P;
end
```

A2.12 reglow.m

Application: This function acts the same as the regression.m does. This version of the routine was improved to measure the low heat transfer region.

Code:

```
% This function receives the line intensity matrix [cx,cy,c]
% and fits a sine curve to the data using nonlinear regression.
% The function returns the unscaled fringe spacing, corresponding to a
% shift of one fringe order (e.g. constructive peak to constructive
peak
% OR destructive peak to destructive peak).
%
% This function is an improvement over regression and regression8,
% in that the average intensity is adjusted (avI) and amplitude (A)
% get adjusted for the best fit. This turns out to
% make no difference to the calculated value of P, in most cases.
%
% THIS FUNCTION IS FOR LOW HEAT TRANSFER REGIONS.
% The entire line scan from p1 to p2 is used. (This is because there is
% not enough pixel data to get the three mean crossings and estimate
% the fringe pitch automatically.) So pick it carefully!
% The scan, p1 to p2, should cover about one period of
% intensity data. The approx fringe Pitch SP, in pixels, in an input.
% SP is needed for a first guess for P in the regression.
% Before running these function you need to enter e.g. SP=512
% in the command window, where approx SP is the fringe spacing in
pixels.

%
function spacing = reglow(cx,cy,c,SP)
P=2*3.14/SP;
ln=[cx,cy,c];
N=length(ln);
% Extracts the average intensity for entire scan length
avI=mean(c);
% Find the mean intensity crossings
% Initialize counters
xings=0;
xi=[];
%
for i=1:N-1
    if ln(i,3)<avI && ln(i+1,3)>avI
        xings=xings+1;
        xi(xings)=i;
    end
    if ln(i,3)>avI && ln(i+1,3)<avI
        xings=xings+1;
        xi(xings)=i;
    end
end
% Use all the data from the scan
for i=1:N
    period(i,1)=ln(i,1);
    period(i,2)=ln(i,3);
```

```
end
%
% Compute revised mean intensity based on one period of fringe data
Avgnew=mean(period);
% Extracts the average intensity -- the mean value of column 2
avI=Avgnew(2);
P1=P;
Pold=0.0;
c1=xi(1);
c1p1=xi(1)+1;
phi=3.14/2.0;
% Initial Phase Angle
    if period(1,2)<period(3,2)
    phi=0.0;
    end
    if period(1,2)>period(3,2)
    phi=3.1415;
    end
% Initial Estimate of Amplitude
Imax=max(period);
Imin=min(period);
A=(Imax(2)-Imin(2))/2.0;
M=length(period);
%
%Outer/Outer Regression Loop (P and phi)
count3=0;
stop3=0;
        while stop3==0 && count3<100
% This is the outer for loop for phi regression
stop=0;
count1=0;
dEold=0;
while stop==0 && count1<7000
% Compute the baseline sum square error (Ebase)
    Ebase=0.0;
        for k=1:M
        Ifit=avI+A*sin(P*(period(k,1)-period(1,1))+phi);
        Diff2=(Ifit-period(k,2))^2.;
        Ebase=Ebase+Diff2;
        end
%
% Increment the phase angle and recompute the sum sq. error (Ephi)
dphi=0.0005;
phi2=phi+dphi;
Ephi=0.0;
        for k=1:M
        Ifit=avI+A*sin(P*(period(k,1)-period(1,1))+phi2);
        Diff2=(Ifit-period(k,2))^2.;
        Ephi=Ephi+Diff2;
        end

% Store the old value of dEdphi (for sign change test)
dEdphi=(Ephi-Ebase)/dphi;

    if dEdphi > 0
       phi=phi-dphi;
    end
```

```
    if dEdphi < 0
       phi=phi+dphi;
    end
        if dEold<0 && dEdphi>0
        stop=1;
        end
        if dEold>0 && dEdphi<0
        stop=1;
        end
count1=count1+1;
dEold=dEdphi;
end
% end of outer for loop for regression of phi
%
% start of outer loop for regression of P
stop=0;
count2=0;
dEold=0;
while stop==0 && count2<1500
%   Compute the baseline sum square error (Ebase)
    Ebase=0.0;
    for k=1:M
    Ifit=avI+A*sin(P*(period(k,1)-period(1,1))+phi);
    Diff2=(Ifit-period(k,2))^2.;
    Ebase=Ebase+Diff2;
    end

%
% Increment the phase angle and recompute the sum sq. error (Ephi)
dP=P1/1000.;
P2=P+dP;
EP=0.0;
    for k=1:M
    Ifit=avI+A*sin(P2*(period(k,1)-period(1,1))+phi);
    Diff2=(Ifit-period(k,2))^2.;
    EP=EP+Diff2;
    end
%
dEdP=(EP-Ebase)/dP;
    if dEdP > 0
       P=P-dP;
    end
    if dEdP < 0
       P=P+dP;
    end
%
    if dEold<0 && dEdP>0
        stop=1;
        end
        if dEold>0 && dEdP<0
        stop=1;
        end
        count2=count2+1;
        dEold=dEdP;
end
% end of P regression loop
% Start of loop for regression of Iav
```

```
stop=0;
countavI=0;
dEold=0;
while stop==0 && countavI<50
%    Compute the baseline sum square error (Ebase)
     Ebase=0.0;
     for k=1:M
     Ifit=avI+A*sin(P*(period(k,1)-period(1,1))+phi);
     Diff2=(Ifit-period(k,2))^2.;
     Ebase=Ebase+Diff2;
     end
%
% Increment the avI and recompute the sum sq. error (EavI)
davI=A/500.;
avI2=avI+davI;
EavI=0.0;
     for k=1:M
     Ifit=avI2+A*sin(P*(period(k,1)-period(1,1))+phi);
     Diff2=(Ifit-period(k,2))^2.;
     EavI=EavI+Diff2;
     end
%
dEdavI=(EavI-Ebase)/davI;
     if dEdavI > 0
        avI=avI-davI;
     end
     if dEdavI < 0
        avI=avI+davI;
     end
%
         if dEold<0 && dEdavI>0
         stop=1;
         end
         if dEold>0 && dEdavI<0
         stop=1;
         end
         countavI=countavI+1;
         dEold=dEdavI;
  end
% end of avI regression loop
%
% Start of loop for regression of A
stop=0;
countA=0;
dEold=0;
while stop==0 && countA<50
%    Compute the baseline sum square error (Ebase)
     Ebase=0.0;
     for k=1:M
     Ifit=avI+A*sin(P*(period(k,1)-period(1,1))+phi);
     Diff2=(Ifit-period(k,2))^2.;
     Ebase=Ebase+Diff2;
     end
%
% Increment the A and recompute the sum sq. error (EA)
dA=A/250.;
A2=A+dA;
```

```
EA=0.0;
     for k=1:M
     Ifit=avI+A2*sin(P*(period(k,1)-period(1,1))+phi);
     Diff2=(Ifit-period(k,2))^2.;
     EA=EA+Diff2;
     end
%
dEdA=(EA-Ebase)/dA;
     if dEdA > 0
        A=A-dA;
     end
     if dEdA < 0
        A=A+dA;
     end
%
         if dEold<0 && dEdA>0
         stop=1;
         end
         if dEold>0 && dEdA<0
         stop=1;
         end
         countA=countA+1;
         dEold=dEdA;
  end
% end of A regression loop
%
count3=count3+1;
deltaP=abs(P-Pold);
         if deltaP<=dP
            stop3=1;
         end
Pold=P;
% outer "while" end statement
                    end
spacing=2*3.14159/P;
end
```

APPENDIX B: EXPERIMENTAL UNCERTAINTY ANALYSIS

B1 Introduction

Like all measurements, the current time-averaging technique has a degree of uncertainty. It includes uncertainty due to digitization and the optics of the Mach-Zehnder Interferometry (MZI). Digitization is related to pixel size of the high speed camera, which is 12 micron in the present work. The MZI has a degree of uncertainty from a variety of sources too. A detailed description of probable sources of error can be found in Machin's thesis (1997).

All uncertainty results were done on the finite fringe mode for the experiment number 69. This experiment was done in the middle of the cavity with a plate spacing of L = 40 mm, a plate-to-plate temperature difference of ΔT = 15 K, and a pressure P = 755 mmHg, and a mean fringe spacing (d) of 107 pixel (1.6 mm). This case was chosen because it represents a typical set of experimental parameters and offers a range of variables to investigate the errors of the measurements.

As mentioned in Chapter 3, the fringes were set in a horizontal position and in finite mode while the model was unheated and the plates were at room temperature. When the plates were heated/cooled, these fringes bent upward in the region close to hot plate and bent downward in areas close to cold plate. The accuracy of these fringe shifts can be affected by any misalignment of the optics. This misalignment, as shown in

Figure 3.1, would create an artificial fringe gradient in the x-direction, resulting in a fringe shift error. Figure B.1 shows a sketch of the fringe misalignment. The degree of misalignment has been exaggerated for illustration purposes.

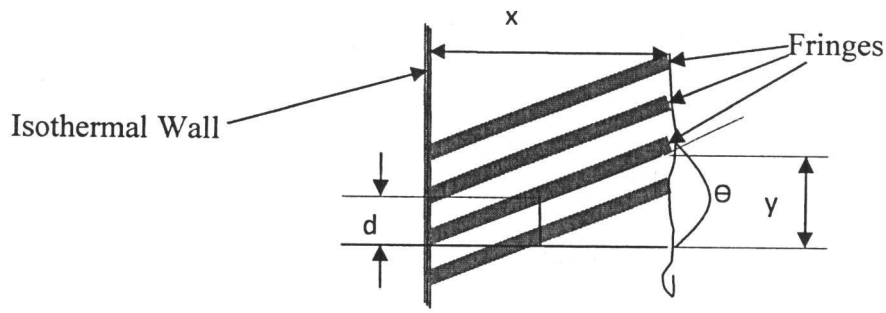

Figure B1 Sketch of the misaligned finite fringes.

Referring to geometry shown in Figure B1 and recalling that "d" is the finite fringe spacing in the y-direction:

$$y = x\tan\theta \quad \text{and} \quad y/d = \varepsilon \tag{B.1}$$

$$\varepsilon = x\tan(\theta)/d \tag{B.2}$$

where ε is fringe shift, x is the x-coordinate of measuring point, and θ is misalignment. Taking the partial derivative of the Eq. B.2 with respect to x gives:

$$\partial\varepsilon/\partial x = \tan\theta/d \tag{B.3}$$

To simplify the analysis, the fringe shift gradient ($\partial\varepsilon/\partial x$) has been renamed F. So, Eq. B.3 becomes:

$$F = \tan\theta/d \tag{B.4}$$

The experimental uncertainty was determined by using Law of Propagation of Uncertainty or the method of Kline and McClintock (1953). Also, NIST (National Institute of Standard and Technology) guideline (Taylor and Kuyatt, 1994) was used to measure Type A of uncertainty. It is assumed that all the uncertainties have the same probability of occurring. Given the result D is a function of n independent variables, x_1, x_2, x_3,..., x_n then;

$$D = D(x_1, x_2, x_3, \dots, x_n) \tag{B.5}$$

And letting U_D be the uncertainty of D and U_1, U_2, U_3,...,U_n be the uncertainty of the independent variables, then the uncertainty of D can be expressed as follows:

$$U_D = \left[\left(\frac{\partial D}{\partial x_1}U_1\right)^2 + \left(\frac{\partial D}{\partial x_2}U_2\right)^2 + \cdots + \left(\frac{\partial D}{\partial x_n}U_n\right)^2\right]^{1/2} \tag{B.6}$$

Using above equation to find the uncertainty of F:

$$U_F = \left[\left(\frac{\partial F}{\partial(tan\theta)}U_{tan\theta}\right)^2 + \left(\frac{\partial F}{\partial d}U_d\right)^2\right]^{1/2} = \left[\left(\frac{1}{d}U_{tan\theta}\right)^2 + \left(\frac{tan\theta}{d^2}U_d\right)^2\right]^{1/2} \tag{B.7}$$

The uncertainties of d and tanθ were estimated to be $U_d = 0.3$mm and $U_{tan\theta} = 0.04$, respectively. Another sources of uncertainty in F came from the noise and optical imperfections. The noise level was calculated and reported in Section 4.2.1. It was 2.8%, which is 0.84 m^{-1}. The optical imperfection uncertainty was estimated about 5%, which is 1.5 m^{-1}.These values were added to the result of Equation B.7 and the result was found to be $\pm 4.81 m^{-1}$.

B2 Uncertainty in the Local Convective Heat Flux

From Section 3.3, Eq. 3.11 was used to calculate the local instantaneous heat transfer rate:

$$q'' = -k_S \frac{R\,\lambda_o\,T_S^2}{wPG}\frac{\partial \varepsilon}{\partial x}\bigg|_{x=0} = -k_S \frac{R\,\lambda_o\,T_S^2}{wPG} F \tag{B.8}$$

Using the description in section B.1, an expression for the error in the local convective heat flux can be determined. Applying Eq. B.8 and Eq. B.6 gives:

$$U_{q''} = \left[\left(\frac{\partial q''}{\partial P}U_P\right)^2 + \left(\frac{\partial q''}{\partial W}U_W\right)^2 + \left(\frac{\partial q''}{\partial T_s}U_{T_s}\right)^2 + \left(\frac{\partial q''}{\partial F}U_F\right)^2\right]^{1/2} \tag{B.9}$$

The following equations are the expressions for the various partial derivatives in Eq. B.9:

$$\frac{\partial q''}{\partial P} = \frac{k_S T_S^2 R\lambda F}{WP^2G} \tag{B.10}$$

$$\frac{\partial q''}{\partial F} = -\frac{k_S T_S^2 R\lambda}{WPG} \tag{B.11}$$

$$\frac{\partial q''}{\partial T_S} = -\frac{2k_S T_S R\lambda F}{WPG} \tag{B.12}$$

$$\frac{\partial q''}{\partial W} = \frac{k_S T_S^2 R\lambda F}{W^2PG} \tag{B.13}$$

Using Equations B.10 through B.13 with the uncertainties listed in Table B1, and the experimental parameters discussed in Sec. B1, the experimental error was determined. The uncertainty in the local convective heat flux was found to be approximately ±0.75%.

A summary of the uncertainties and the propagated errors are shown in Table B1.

Table B1 The uncertainty of the parameters associated with a typical measurement (for $\overline{q_y''}$ = 22.27 W/m^2).

Measured identity	**Tool used**	**Uncertainty**	$\frac{\partial q''}{\partial x_n} U_n$(W/m^2)
Pressure, U_P	Barometer	±26.6 Pa	±0.000022
Plate Temperature, U_{Ts}	Platinum resistance thermometer	±0.3 K	±0.00017
Optical length of plate U_w	Micrometer	±0.005 m	±0.00078
Fringe shift gradient, U_F	MATLAB	±4.81m^{-1}	±0.17

The uncertainty due to the capturing time (ten seconds) affects the total uncertainty of the experiment independently. Assuming that 67% is the chance that all time-averaged values lay between maximum and minimum values, the uncertainty can be estimated to be 2.2%. Data are provided in Section 4.3.3. Also, experiments 143 and 137 were set up to check the reproducibility. All parameters (e.g., location, temperatures) were fixed, but time. The time-averaged heat flux from these two experiments was 0.21% different.

Considering 5% uncertainty due to optical imperfection (Type B) and 2.2% statistical uncertainty (Type A), the combined uncertainty was measured using *the law of propagation of uncertainty* (square root of the sum-of-the squares or "RSS" method). Based on the "RSS" method, the uncertainty due to the time averaging was 5.5%.

APPENDIX C: SAMPLE CALCULATIONS

A sample calculation is done for the finite fringe interferogram for the case of the largest wall spacing of L = 56.2 mm and camera distance of 23 inches (Experiment 16), plate to plate temperature difference of $\Delta T = 15.09$ °K. A summary of the parameters used for the calculation is shown in Table C1.

Table C1 Given data

Parameter	Value
Gladstone-Dale constant, G	0.226×10^{-3} m^3/kg
Wavelength of He-Ne laster, λ_0	6.328×10^{-7} m
Gas Constant, R	287 J/kg·K
Ambient pressure, P	101720 Pa
Cold wall temperature (A), T_c	288.67 K
Hot wall temperature (B), T_h	303.76 K
Length of model in light beam direction, W	0.547 m
Average gap between isothermal walls, L	0.0562 m
Pin distance, real size	0.006935 m
Pin distance, on the image	560 pixels

C1 Air Properties

Film temperature, T_f

$$T_f = \frac{1}{2}(T_c + T_h)$$

$$= \frac{1}{2}(288.67 + 303.76) = 296.215 \text{ K}$$

Volumetric expansion coefficient, β

$$\beta = \frac{1}{T_f}$$

$$= \frac{1}{296.215}$$

$$\beta = 0.0034 \, {}^{1}/_{K}$$

Density, ρ

Using the ideal gas law:

$$\rho = \frac{P}{RT_f}$$

$$\rho = \frac{101720}{287 \times 296.215}$$

$$\rho = 1.1965 \, kg/m^3$$

Dynamic viscosity, μ at T_f

Using Touloukian and Makita (1975) evaluated at the film temperature:

$$\mu = 1.835 \times 10^{-5} \, kg/m \cdot s$$

Thermal conductivity using the surface and film temperatures (T_s = 288.67 K & T_f = 296.22 K), k_S & k_f,

Using Touloukian and Makita (1975) evaluated at cold wall temperature:

$$k_S = 0.0253\ W/m \cdot K\ \&\ k_f = 0.0259\ W/m \cdot K$$

Specific heat, c_P

Using Touloukian and Makita (1975) evaluated at the film temperature:

$$c_P = 1006.2\ J/kg \cdot K$$

C2 Cavity Properties

Aspect ratio, A

Using average gap between isothermal surfaces, L:

$$A = H/L = 980/56.2 = 17.44$$

Rayleigh number, Ra:

$$Ra = \frac{\rho^2 L^3 g C_p \Delta T \beta}{\mu k} = 269310$$

C3 Heat Flux

Scale Factor, SF

Following instruction number001,

$$SF = \frac{pin\ distance\ in\ meter}{pin\ distance\ in\ pixel}$$

$$SF = \frac{0.006935}{560} = 1.23 \times 10^{-5}\ m/pixel$$

The image processing software determined the fringe peaks in units of pixel. Mean value of fringe spacing was 180 pixels:

$$dx = 180 * 1.23 \times 10^{-5} = 0.0022 \text{ m}$$

Fringe shift difference, $d\varepsilon = 1$

Fringe gradient, $\partial\varepsilon/\partial x$

The fringe gradient was determined by assuming linear interpolation:

$$\left.\frac{\partial \varepsilon}{\partial x}\right|_{x=0} = \frac{\Delta \varepsilon}{\Delta x}$$

$$\left.\frac{\partial \varepsilon}{\partial x}\right|_{x=0} = \frac{1}{0.0022}$$

$$\left.\frac{\partial \varepsilon}{\partial x}\right|_{x=0} = 454\, m^{-1}$$

Local convective heat flux, $q_y^{"}$

$$q_y^{"} = -\frac{k_s\, R\, \lambda_o\, T_s^2}{wPG} \left.\frac{\partial \varepsilon}{\partial x}\right|_{x=0}$$

$$= -\frac{0.0253 \frac{W}{mK} * 287 \frac{\text{J}}{\text{kgK}} * 6.328 \text{ x } 10^{-7} \text{ m} * (288.67K)^2}{0.547 \text{ m} * 101720 \text{ Pa} * 0.000226 \text{ m}^3/\text{kg}} * 454 m^{-1}$$

$$q_y^{"} = -13.83\, W/m^2$$

C4 Nusselt Number

$$Nu_y = \frac{q''_y L.}{k_f\,(T_h - T_c)} = \frac{-\frac{13.83W}{m^2} * 0.0562\ \text{m}}{0.0259 W/m{\cdot}K\ (15.09)} = -\ 1.99$$

C5: Fringe Shift along Test Model

$$\Delta\varepsilon = \frac{PGw}{R\lambda_o}\left(\frac{1}{T_c} - \frac{1}{T_h}\right) = \frac{10172\ \text{Pa} * 0.000226 \frac{\text{m3}}{\text{kg}} * 0.547\ \text{m}}{287 \frac{\text{J}}{\text{kgK}} * 6.328 \times 10^{-7}\ \text{m}}\left(\frac{1}{288.67\ \text{K}} - \frac{1}{303.76\ \text{K}}\right) = 11.73$$

$\Delta T/\Delta\varepsilon = 15/11.73 = 1.3$ K/fringe

APPENDIX D: SELECTED TABULAR DATA

D1 Introduction

In this appendix, only time-averaged and input tables are listed. It is not possible to present all the tables here, because of space limitations. All instantaneous values were saved on a DVD. It is available in the Thermofluids Research Lab. Wall A and B refer to the cold wall and hot wall respectively. Finally, the content of the ExperimentData file is presented.

D2 Time-Averaged Values

Table D1 Time-averaged value in each level (A = 30.3, $Ra_m = 5x10^4$)

Y (mm)	$\overline{Nu_y}$	$\overline{q_y''}$ (W/m^2)	SD(W/m^2)	Scattering (%)	Exp. #	Wall
5	0.35	4.16	1.6	148	43	A
15	0.35	4.16	1.6	148	43	A
20	0.32	3.8	0.58	64.6	46	A
35	0.63	7.59	0.76	150	47	A
50	0.65	7.88	1.21	73	50	A
60	0.93	11.2	3.86	996	51	A
70	1.32	17	1.46	36.2	54	A
90	1.32	16	1.46	36.2	54	A
100	1.29	16.4	1.1	33.4	57	A
110	1.29	15.4	1.1	33.4	57	A
170	1.52	18.3	1.82	48.3	58	A
260	1.77	21.3	2.47	49.1	61	A
340	2.25	26.7	2.17	44.9	62	A
400	2.16	25.8	2.56	77.9	65	A
485	2.18	26.1	3.13	53.7	66	A
485	2.17	25.8	2.33	51	67	B
400	2.45	29.2	3.27	49	64	B
340	2.23	26.5	3.65	55.2	63	B
260	1.86	22.3	1.33	29.83	60	B
170	2.00	23.9	1.08	20.49	59	B

Y (mm)	$\overline{Nu_y}$	$\overline{q_y^{"}}$ (W/m^2)	SD(W/m^2)	Scattering (%)	Exp. #	Wall
110	2.72	32.7	1	15.82	56	B
100	2.82	33.9	1.57	21.32	55	B
90	3.67	44.3	2.95	33.59	53	B
70	3.17	38.2	0.84	11.25	52	B
60	3.45	41.6	1.12	11.61	52	B
50	3.16	38.1	0.51	7.74	49	B
35	3.87	46.7	0.58	5.68	48	B
20	5.08	61.1	1.27	9.64	45	B
15	4.78	57.3	1.14	10.63	44	B
5	5.50	66.3	0.72	6.6	44	B

Table D2 Time-averaged value in each level (A = 24.5, $Ra_m = 10^5$)

Y (mm)	$\overline{Nu_y}$	$\overline{q_y^{"}}$ (W/m^2)	SD(W/m^2)	Scattering (%)	Exp. #	Wall
5	1.42	13.66	1.05	60	87	A
15	1.42	13.66	1.05	60	87	A
30	1.26	13.28	38.59	31.58	84	A
50	1.26	12.28	38.59	31.58	84	A
90	1.15	11.23	1.05	41.34	83	A
120	1.36	13.26	5.27	513	80	A
180	1.86	18.06	1.6	42.37	79	A
250	2.25	21.91	1.8	37.23	76	A
300	2.83	27.58	9.97	348	75	A
350	2.64	25.77	3.08	54.45	72	A
400	2.50	24.35	2.24	96.75	71	A
480	2.91	28.29	9.98	243	68	A
480	2.74	26.65	2.19	36.84	69	B
400	2.62	25.57	2.59	51.92	70	B
350	2.85	27.81	2.49	41.37	73	B
300	2.64	25.7	2.93	46.19	74	B
250	2.97	28.77	7.3	295	77	B
180	2.88	28.03	1.81	39	78	B
120	3.58	34.97	1.29	38.24	81	B
90	4.46	42.32	6.66	112.7	82	B
50	5.07	49.59	1.11	9.95	85	B
30	5.36	52.42	0.77	8.19	85	B
15	5.81	56.77	0.697	5.97	86	B
5	6.57	64.2	1.16	11.55	86	B

Table D3 Time-averaged value in each level (A = 17.4, $Ra_m = 2.7x10^5$)

Y (mm)	$\overline{Nu_y}$	$\overline{q''_y}$ (W/m^2)	SD(W/m^2)	Scattering (%)	Exp. #	Wall
5	0.86	6.113	7.19	1787	91	A
15	0.86	6.113	7.19	1787	91	A
30	0.9	6.26	4.23	302.4	92	A
50	0.9	6.26	4.23	302.4	92	A
70	0.9	6.26	4.23	302.4	95	A
90	0.93	6.47	2.6	268	96	A
120	0.99	6.85	1.24	114	88	A
140	1.29	8.96	3.98	235	99	A
180	1.50	10.44	2.6	452	15	A
250	2.02	14.09	2.69	376	16	A
300	2.87	19.91	1.69	52.15	102	A
350	3.38	23.52	2.96	71.9	103	A
410	3.11	21.58	3.65	119	106	A
480	3.61	25	1.15	19	107	A
480	3.64	25.19	3.28	70.94	108	B
410	3.44	23.85	2.94	101.8	105	B
350	3.98	27.68	3.54	121.5	104	B
300	3.45	23.95	2.45	50.28	101	B
250	3.96	27.52	1.55	36.17	100	B
180	4.37	30.33	2.09	88.8	14	B
140	5.24	36.38	1.69	22.54	98	B
120	5.92	41.16	1.06	15.54	89	B
90	6.63	46.02	4.65	147.5	97	B
70	6.89	47.82	1.6	13.31	94	B
50	7.64	52.97	1.31	16.73	93	B
30	8.25	57.22	2.188	19.28	93	B
15	8.10	55.91	2.12	17.26	90	B
5	8.78	60.79	3.3	20.11	90	B

Table D4 Time-averaged Nusselt number in different y-coordinate for recent improved experiments (A = 17.3, $Ra_m = 2.9x10^5$)

y/H	$\overline{Nu_y}$	Exp #	Wall
0.005	0.41	127	A
0.01	0.50	127	A
0.02	0.67	128	A
0.04	1.02	129	A
0.05	1.05	130	A
0.06	1.26	131	A
0.08	1.39	132	A
0.09	1.44	133	A
0.10	1.63	134	A
0.12	1.64	135	A
0.13	1.60	136	A
0.19	2.19	140	A
0.24	2.53	141	A
0.30	3.12	142	A
0.37	3.59	115	A
0.43	3.87	114	A
0.50	4.15	111	A
0.005	6.29	126	B
0.01	10.19	126	B
0.02	9.38	125	B
0.04	9.34	124	B
0.05	8.57	123	B
0.06	7.67	122	B
0.08	7.69	121	B
0.09	6.24	120	B
0.10	5.57	119	B
0.12	5.34	118	B
0.13	5.41	117	B
0.19	4.29	139	B
0.24	4.74	138	B
0.30	4.24	137	B
0.37	4.34	116	B
0.43	3.70	113	B
0.50	4.16	112	B

D2 Content of ExperimentData File

Table D5 Contents of ExperimentData file, shaded column is added for more clarification. It is not part of the input file.

Experiment Number	1	2	3	4	5	6	7	8	9	10	11	12	13	14	15	16
Frames/s	200	100	500	100	50	30	50	30	100	200	500	300	30	100	100	100
Spacing (mm)	40	40	40	40	40	40	40	40	40	40	40	40	40	56.2	56.2	56.2
Exposure (μs)	4997	2820	1997	2824	2823	2823	1585	1120	1583	1583	1583	1583	518	4094	4094	4094
Camera Distance (inch)	18	18	18	18	18	18	18	18	18	18	18	18	18	23	23	23
Number of pictures	3272	1200	3272	1200	600	400	1600	1000	2000	4929	6117	5018	50	1000	1000	1000
Walling	0	0	0	0	0	0	0	0	0	0	0	0	0	1	0	0
Pin Distance (pixel)	478	470	470	480	480	480	450	450	470	450	450	450	458	560	560	560
T_c (°C)	15.72	15.72	15.72	15.72	15.72	15.72	11.6	11.6	11.6	11.61	11.63	11.6	15.48	15.52	15.52	15.52
T_h (°C)	30.09	30.09	30.09	30.09	30.09	30.09	31.64	31.64	31.64	31.65	31.66	31.66	30.56	30.61	30.61	30.61
Room Temp. (°C)	21.1	21.1	21.1	21.1	21.1	21.1	21.6	21.6	21.6	21.5	21.6	21.6	23	23	23	23
Pressure (mmHg)	758.1	758.1	758.1	758.1	758.1	758.1	749	749	749	749	749	749	753.6	763	763	763
Date (mm.dd)	6.11	6.11	6.11	6.11	6.11	6.11	6.16	6.16	6.16	6.16	6.16	6.16	6.23	10.1	10.1	10.1
y (mm)	490	490	490	490	490	490	490	490	490	490	490	490	490	800	180	250
y/H	0.50	0.50	0.50	0.50	0.50	0.50	0.50	0.50	0.50	0.50	0.50	0.50	0.50	0.18	0.18	0.26
Ra	91512	91512	91512	91512	91512	91512	127104	127104	127104	127084	126991	127211	94727	269310	269310	269310

Experiment Number	17	18	19	20-NA	21	22	23	24	25	26	27	28	29	30	31	32
Frames/s		500	200	100	100	100	100	100	200	200	100	100	100	100	100	100
Spacing (mm)		40	40	40	40	12.7	12.7	12.7	32.3	32.3	32.3	12.7	12.7	12.7	12.7	12.7
Exposure (μs)		1997	2941	4160	5997	5877	5877	4152	3533	3533	4152	2493	3518	3517	3517	3515
Camera Distance (inch)		26	26	26	26	23	23	18.5	18	18	18	18	18	18	18	18
Number of pictures		9746	9000	4500	3000	2000	2000	2000	2500	2500	1000	1500	1600	1000	1000	1000
Walling		0	0	1	1	0	1	0	1	0	1	5	4	5	4	1
Pin Distance (pixel)		620	640	670	660	576	576	468	458	458	471	464	464	460	460	447
T_c (°C)		15.72	15.73	15.72	15.71	15.37	15.37	15.45	15.48	15.48	21.2	15.38	15.38	15.45	15.45	15.44
T_h (°C)		30.55	30.54	30.52	30.52	30.44	30.44	30.4	30.56	30.56	21.22	30.47	30.47	30.49	30.49	30.46
Room Temp. (°C)		23.1	23	22.7	22.7	22.5	22.5	22.7	23	23	22	23	23	23.4	23.4	22.8
Pressure (mmHg)		760	756.4	749.5	749.2	754.2	754.2	751.8	753.6	753.6	761	766	766	754	753	746
Date (mm.dd)		6.24	6.25	6.28	6.29	7.2	7.2	7.8	7.21	7.21	8.23	9.10	9.10	9.13	9.13	9.14
y (mm)		490	490	490	490	480	480	480	490	490	490	490	490	510	560	610
y/H		0.50	0.50	0.50	0.50	0.50	0.50	0.50	0.50	0.50	0.50	0.49	0.51	0.53	0.58	0.64
Ra		94576	93555	91816	91811	3040	3040	2996	49877	49877	0	3139	3139	3029	3021	2962

Experiment Number	33	34	35	36	37	38	39	40	41	42	43	44	45	46	47	48	49
Frames/s	100	100	100	100	100	100	100	100	100	100	100	100	100	100	100	100	100
Spacing (mm)	12.7	12.7	12.7	12.7	12.7	12.7	12.7	12.7	12.7	12.7	32.3	32.3	32.3	32.3	32.3	32.3	32.3
Exposure (μs)	3515	2458	2458	2458	2458	2458	3993	2899	2899	4099	4096	4096	4096	2896	4096	4096	4096
Camera Distance (inch)	18	18	18	18	18	18	18	18	18	18	19	19	19	19	19	19	19
Number of pictures	1000	1000	1000	1000	1000	1000	1000	1000	1000	1000	13	1000	1000	1000	978	1000	1000
Walling	1	1	1	1	1	1	1	0	2	0	0	1	1	0	0	1	0
Pin Distance (pixel)	447	446	446	446	446	440	449	468	468	468	460	460	470	470	470	470	475
T_c (°C)	15.45	15.47	15.47	15.46	15.45	15.44	15.47	15.51	15.46	15.48	15.53	15.52	15.57	15.57	15.56	15.56	15.56
T_h (°C)	30.46	30.45	30.45	30.46	30.48	30.48	30.48	30.47	30.46	30.48	30.57	30.58	30.6	30.6	30.62	30.62	30.63
Room Temp. (°C)	23	23.3	23.3	23.3	23.3	23	23	23.5	23	23	22.7	22.7	23	23	23	23	23
Pressure (mmHg)	746	761.8	761.8	761.8	761.8	763	763	750	749	749.5	749	749	748.4	748.4	749	749	749
Date (mm.dd)	9.14	9.15	9.15	9.15	9.15	9.19	9.19	9.30	9.30	9.30	10.1	10.1	10.1	10.1	10.1	10.1	10.4
y (mm)	660	760	810	860	910	610	660	5	945	30	5	975	960	20	40	930	60
y/H	0.69	0.79	0.84	0.90	0.95	0.64	0.69	0.01	0.98	0.03	0.01	0.99	0.98	0.02	0.04	0.95	0.06
Ra	2960	3080	3080	3085	3091	3103	3096	2980	2982	2985	49116	49182	48978	48978	49151	49151	49180

Experiment Number	50	51	52	53	54	55	56	57	58	59	60	61	62	63	64	65	66
Frames/s	100	100	100	100	100	100	100	100	100	100	100	100	100	100	100	100	100
Spacing (mm)	32.3	32.3	32.3	32.3	32.3	32.3	32.3	32.3	32.3	32.3	32.3	32.3	32.3	32.3	32.3	32.3	32.3
Exposure (μs)	4096	4096	4096	5792	5792	5792	4094	4094	4094	4094	4094	4094	4094	4094	4094	4094	4094
Camera Distance (inch)	19	19	19	19	19	19	19	19	19	19	19	19	23	23	23	23	23
Number of pictures	1000	1000	1000	1000	1000	1000	1000	1000	1000	1000	1000	1000	1000	1000	1000	1000	1000
Walling	0	0	1	1	0	1	1	0	0	1	1	0	0	1	1	0	0
Pin Distance (pixels)	475	470	470	480	480	480	470	470	470	470	470	470	560	560	560	560	560
T_c (°C)	15.56	15.58	15.58	15.59	15.59	15.6	15.64	15.63	15.61	15.61	15.61	15.61	15.73	15.73	15.71	15.71	15.62
T_h (°C)	30.63	30.63	30.63	30.64	30.64	30.62	30.62	30.62	30.59	30.59	30.59	30.59	30.59	30.59	30.6	30.6	30.58
Room Temp. (°C)	23	23	23	23.2	23.2	23.2	23.5	23.5	23	23	23	23	23	23	23	23	22.7
Pressure (mmHg)	749	749	749	756	756	756	758	758	762.5	762.5	762.5	762.5	768	768	768	768	761
Date (mm.dd)	10.4	10.4	10.4	10.5	10.5	10.5	10.5	10.5	10.6	10.6	10.6	10.6	10.11	10.11	10.11	10.11	10.14
y (mm)	60	70	910	900	90	890	880	100	170	810	720	260	310	670	600	380	490
y/H	0.06	0.07	0.93	0.92	0.09	0.91	0.90	0.10	0.17	0.83	0.73	0.27	0.32	0.68	0.61	0.32	0.50
Ra	**49180**	**49107**	**49107**	**50021**	**50021**	**49925**	**50041**	**50078**	**50660**	**50660**	**50660**	**50660**	**50934**	**50934**	**51041**	**51041**	**50394**

Experiment Number	67	68	69	70	71	72	73	74	75	76	77	78	79	80	81	82
Frames/s	100	100	100	100	100	100	100	100	100	100	100	100	100	100	100	100
Spacing (mm)	32.3	40	40	40	40	40	40	40	40	40	40	40	40	40	40	40
Exposure (μs)	4094	4094	4094	4094	4094	4094	4094	4094	4094	4094	4094	4094	4094	4094	4094	4094
Camera Distance (inch)	23	19	19	19	19	19	19	19	19	19	19	19	19	19	19	19
Number of pictures	1000	1000	1000	1000	1000	1000	1000	1000	1000	1000	1000	1000	1000	1000	1000	1000
Walling	1	0	1	1	0	0	1	1	0	0	1	1	0	0	1	1
Pin Distance (pixel)	560	473	473	475	475	475	475	475	475	475	475	475	475	475	475	475
T_c (°C)	15.62	15.57	15.57	15.59	15.58	15.58	15.58	15.58	15.58	15.59	15.59	15.59	15.59	15.55	15.55	15.55
T_h (°C)	30.58	30.6	30.6	30.67	30.66	30.66	30.66	30.66	30.66	30.63	30.63	30.63	30.63	30.67	30.67	30.67
Room Temp. (°C)	22.7	23	23	23.5	23.5	23.5	23.5	23.5	23.5	23.8	23.8	23.8	23.8	23.5	23.5	23.5
Pressure (mmHg)	761	768	768	768	768	768	768	768	768	768	768	768	768	763	763	763
Date (mm.dd)	10.14	10.7	10.7	10.6	10.6	10.6	10.6	10.6	10.6	10.7	10.7	10.7	10.7	10.7	10.7	10.7
y (mm)	490	485	495	580	400	350	630	680	300	250	730	800	180	120	860	890
y/H	0.50	0.49	0.51	0.59	0.41	0.36	0.64	0.69	0.31	0.26	0.74	0.82	0.18	0.12	0.88	0.91
Ra	**50394**	**97956**	**97956**	**98213**	**98228**	**98228**	**98228**	**98228**	**98228**	**97983**	**97983**	**97983**	**97983**	**97226**	**97226**	**97226**

Experiment Number	83	84	85	86	87	88	89	90	91	92	93	94	95	96	97
Frames/s	100	100	100	100	100	100	500	100	100	100	100	100	100	100	100
Spacing (mm)	40	40	40	40	40	56.2	56.2	56.2	56.2	56.2	56.2	56.2	56.2	56.2	56.2
Exposure (μs)	4094	4094	4094	4094	4094	4094	4094	4094	4094	4094	4094	4094	4094	4094	4094
Camera Distance (inch)	19	19	19	19	19	19	19	23	23	23	23	23	23	23	23
Number of pictures	478	1000	1000	300	1000	1000	7500	1000	1000	1000	1000	1000	1000	1000	1000
Walling	0	0	1	1	0	0	1	1	0	0	1	1	0	0	1
Pin Distance (pixel)	475	475	475	475	475	478	478	560	560	560	560	560	560	560	560
T_c (°C)	15.55	15.55	15.55	15.55	15.55	15.55	15.55	15.6	15.6	15.6	15.57	15.57	15.57	15.57	15.57
T_h (°C)	30.67	30.67	30.67	30.67	30.67	30.67	30.67	30.65	30.65	30.65	30.65	30.65	30.65	30.65	30.65
Room Temp. (°C)	23.5	23.5	23.5	23.5	23.5	23.8	23.8	23.5	23.5	23.5	23.5	23.5	23.5	23.5	23.5
Pressure (mmHg)	763	763	763	763	763	751	751	755	755	755	755	755	755	755	755
Date (mm.dd)	10.7	10.7	10.7	10.7	10.7	10.8	10.8	10.9	10.9	10.9	10.9	10.9	10.1	10.1	10.1
y (mm)	90	50	930	970	10	120	610	505	15	40	530	550	60	90	580
y/H	0.09	0.05	0.95	0.99	0.01	0.12	0.62	0.52	0.02	0.04	0.54	0.56	0.06	0.09	0.59
Ra	**97226**	**97226**	**97226**	**97226**	**97226**	**261240**	**261240**	**262747**	**262747**	**262747**	**263332**	**263332**	**263332**	**263332**	**263332**

Experiment Number	98	99	100	101	102	103	104	105	106	107	108	109	110
Frames/s	100	100	100	100	100	100	100	100	100	100	100	100	100
Spacing (mm)	56.2	56.2	56.2	56.2	56.2	56.2	56.2	56.2	56.2	56.2	56.2	56.2	56.2
Exposure (μs)	4094	4094	4094	4094	4094	4094	4094	4094	4094	4094	4094	4094	4094
Camera Distance (inch)	23	23	23	23	23	23	23	19	19	19	19	23	23
Number of pictures	1000	1000	1000	1000	1000	1000	1000	1000	1000	1000	1000	1000	1000
Walling	1	0	1	1	0	0	1	1	0	0	1	1	0
Pin Distance (pixel)	560	560	560	560	560	560	560	465	465	465	465	560	560
T_c (°C)	15.57	15.57	15.52	15.51	15.51	15.51	15.51	15.54	15.54	15.54	15.54	15.55	15.55
T_h (°C)	30.65	30.65	30.61	30.62	30.62	30.62	30.62	30.6	30.6	30.6	30.6	30.61	30.61
Room Temp. (°C)	23.5	23.5	23	23.5	23.5	23.5	23.5	23	23	23	23	23	23
Pressure (mmHg)	755	755	763	763	763	763	763	769	769	769	769	768	768
Date (mm.dd)	10.1	10.1	10.1	10.11	10.11	10.11	10.1	10.11	10.11	10.11	10.11	10.11	10.11
Y (mm)	630	140	740	790	300	360	850	900	410	470	470	470	470
y/H	0.64	0.14	0.76	0.81	0.31	0.37	0.87	0.92	0.42	0.48	0.48	0.48	0.48
Ra	**263332**	263332	269310	269667	269667	269667	269667	272997	272997	272997	272997	272245	272245

APPENDIX E: INSTRUCTIONS

The following instructions are helpful to conduct the safe and effective experiments.

E1 Interferometer Set up Procedure

Instruction: Experimental Procedure for interferometer (see figure 2.1)

Scope: Thermo fluid Research Lab. (EPH 440)

- ☐ Level table
- ☐ Check laser alignment and collimation
  - ☐ Make sure the reflection of mirror 3 is uniform without any finite fringes (this is done my moving the laser forward or backward).
  - ☐ Check that all the mirrors are alignment relative to the incident laser beam.
- ☐ Prepare model
  - ☐ Adjust and record the level of the cavity that is under investigation
  - ☐ place optical windows
  - ☐ move model close enough to connect thermocouples
  - ☐ record which thermocouples are in use
- ☐ Place unheated model in the test beam (between mirrors 5 and 6)
- ☐ Block the reference beam (between mirrors 2 and 3) and align the test model using the plumb bob and level.
- ☐ Place a white card in front of mirror 7 and adjust mirror 5 by aligning the leveling pins on the output.
- ☐ Unblock reference beam and obtain interference by 'near and far field focusing'.
  - ☐ Place a pointed object between mirrors 4 and 3 (object 1), and another object between mirrors 6 and 7 (object 2).
  - ☐ Adjust mirror 2 until the two shadows of object 1 appear as a single shadow in the output of mirror 7.
  - ☐ Adjust mirror 6 until the two shadows of object 2 appear as a single shadow in the output of mirror 7.
  - ☐ Repeat 6b and 6c until both objects are have solid shadows.
  - ☐ Carefully adjust mirror 6 until interference fringes appear on the output of mirror 7.

- ☐ Adjust mirror 8 so that it appears slightly off center in the output (note: do not want the mirror 8 in the window cavity).
- ☐ Adjust mirror 8 so that the output is parallel to the ground.
  - ☐ Measure height of mirror 8.
  - ☐ Measure height of the mirror 8 shadow on the output on the wall.
  - ☐ Adjust mirror 7 so that the focal point of the mirror 7 output is hitting mirror 8 (should show up as a red point)
  - ☐ Adjust mirror 8 so that the shadow height is equal to the actual height of the mirror.
- ☐ Place camera to be inline of mirror 8 output.
  - ☐ Adjust the camera's height, pitch, yaw, and position on the floor.
- ☐ Connect the camera to the computer.
- ☐ Turn off the laser a place a light source at the midsection of the test model.
- ☐ Focus the camera to the light source (This is done so that the camera is focused at the center of the test model)
- ☐ Turn on the laser, and obtain desired interference pattern on the monitor. Adjust fringes such that they are parallel to the horizontal grid on the monitor (recommended to use approximately 10 -12 fringes).
- ☐ Heat the model to desired settings (adjust constant temperature baths and DC power supply).
- ☐ Follow the calibration instruction to get the scale factor.
- ☐ Take pictures
  - ☐ Adjust the fps, exposure, ROI (if applicable) and record the pictures
  - ☐ NEVER use the full capacity of camera memory
- ☐ Process pictures
  - ☐ Take a back up of the pictures
  - ☐ Process the picture using Matlab codes
    - Run MMFile.m to make directories and move the pictures from back up device to each directory
    - Run the read.m to feed the scan line (x1 and x2), wall location (w1) and pin distance (s1 and s2) if applicable
    - Run iterate.m to find the optimum filtering and then scan all pictures. In the end each picture directory would have a file (HTResult) that contains q", h and Nu of the picture.

E2 Calibration Instruction

Scope: Thermo fluid Research Lab. (EPH 440)

Instruments: MotionPro X3 High speed camera; interferometer system; fixed pins

1. Measure the distance between the fixed pins using any accurate optical devices (as much accurate as possible) and take a note of it (=Pd). It is = 0.006935 m for current tool (Figure 2.5).
2. Start calibration just before capturing the experiment pictures
3. Open ' MotionPro X Studio' software and adjust ROI if applicable
4. Whenever the optimum condition is set up and pin line is perpendicular to beam direction, block the reference beam
5. Change the condition of the camera from 'live' to stop
6. Open the Matlab software and make sure it is in the "C:\Program Files\IDT\MotionProX\Matlab" directory
7. Open up the file "SnapEx.m" and run it
8. The picture would be popped up. Click on "Data Cursor" and then select each pin tip and note the x-value of the points, successively
9. Subtract the x-value pixels (=S), then divide Pd to S (Pd/S) to get scale factor
10. Save the snapshot appropriately (it could have the name of the experiment number and close Matlab and start capturing experiment pictures
11. Transfer scale factor to experiment log or ExperimentData file ASAP

E3 ExperimentData File Preparation

ExperimentData input file contents, which must be entered carefully before experiment starts:
Row 1: experiment number
Row 2: frame per second (fps) of the captured picture in Hz
Row 3: size of the cavity that beam passes through it in mm
Row 4: Exposure time in micro second
Row 5: camera distance from small mirror in inch
Row 6: Number of pictures
Row 7: walling; 0 means wall A is exposed; otherwise it is wall B
Row 8: pin distance in pixel (it depends on camera distance from small mirror)
Row 9: Temperature of wall A in degree centigrade
Row 10: Temperature of wall B in degree centigrade
Row 11: Ambient Temperature in degree centigrade
Row 12: uncorrected pressure in mmHg
Row 13: Date of the experiment in mm/dd format (the year is 2008)
Row 14: level of the captured image from the bottom of cavity in mm
Row 15: Rayleigh number of the experiment calculated by Rayleigh.m file.

REFERENCES

Almeida, F., 2008, "An Interferometric Study of Free Convection in a Window with a Heated between-Panes," M.A.Sc. Thesis, Ryerson University, Toronto, Ontario, Canada.

Almeida, F., Naylor, D., Oosthuizen, P.H., 2008, "An Interferometric Study of Free Convection in a Window with a Heated between-Panes Blind," *Proceedings, Solar Buildings Research Conf.* Fredericton, N.B.

Atul Srivastava, Atanu Phukan, P.K. Panigrahi, K. Muralidhar, 2004, "Imaging of a Convective Field in a Rectangular Cavity using Interferometry, schlieren and shadowgraph," *Optics and Lasers in Engineering,* vol.42, pp. 469–485.

Bairi, A., 2008, "Nusselt–Rayleigh Correlations for Design of Industrial Elements: Experimental and Numerical Investigation of Natural Convection in Tilted Square Air Filled Enclosures," *Energy Conversion and Management,* vol.49, no. 4, pp. 771–782.

Batchelor, G. K., 1954, "Heat Transfer by Free Convection across a Closed Cavity between Vertical Boundaries at Different Temperatures," *Q. Appl. Math.,* vol. 12, pp. 209–223.

Bergholz, R.F., 1978, "Instability of Steady Natural Convection in a Vertical Fluid Layer," *Journal of Fluid Mech*anics, vol. 84, no. 4, pp. 743–768.

Catton, I., 1978, "Natural Convection in Enclosures," *Proc 6th International Heat Transfer Conf*, vol. 6, Toronto, Canada, pp. 13–43.

Chen, F., Luo, W.D., Petniunas, A., Harward, P., Brown, G.M., 2003, "High-speed ESPI and Related Techniques: Overview and its Application in the Automotive Industry," *Optics and Lasers in Engineering,* vol. 40, pp. 459-485.

Cranz, C., Schardin, H., 1929, "Kinematographie auf Ruhendem Film und mit Extreme hoher Bildfrequenz," *Z. Phys*. Vol. 56, pp. 147-183.

Dukhovski, I.A., Komissaruk, V.A., Kovalev, P.I., Mende, N.P., June 1985, "High Speed Photography of the Interaction of a Water Drop with a Supersonic Sphere," *Optics & Laser Technology,* pp. 148-150.

El Sherbiny, S.M., 1980, "Heat Transfer by Natural Convection across Vertical and Inclined Air Layers," PhD thesis, University of Waterloo, Waterloo, Ontario, Canada.

El Sherbiny, S.M., Raithby, G.D., Holland, K.G.T., Feb. 1982, "Heat Transfer by Natural Convection across Vertical and Inclined Air Layers," *Journal of Heat Transfer*, vol. 104, pp. 96-102.

Ganzorolli, M.M., Milanez, L.F., 1995, "Natural Convection in Rectangular Enclosures Heated From below and Symmetrically Cooled from the Sides," *International Journal of Heat and Mass Transfer*, vol. 38(6), pp. 1063–73.

Gibhart, B., Jaluria, Y., Mahajan, R. L., Sammakia, B., 1988, *Buoyancy-Induced Flows and Transport,* Hemispher Publishing Corp., New York.

Goldstein, R.J., 1970, *Optical Measurement of Temperature*, Chapter 4 in Measurement Techniques in Heat Transfer, eds. E.R.G. Eckert and R.J. Goldstein, Technovision Services, Slough, England, pp. 177-228.

Herman, C., Kang, E., Watzel, M., 1998, "Expanding the Applications of Holographic Interferometry to the Quantitative Visualization of Oscillatory Thermo Fluid Processes using Temperature as Tracer," *Experiments in Fluids,* vol. 24, pp. 431-446.

Herman, C., Kang, E., 2001, "Comparative Evaluation of Three Heat Transfer Enhancement Strategies in a Grooved Channel," *Heat and Mass Transfer*, vol. 37, pp. 563-575.

Hollands, K.G.T., Raithby, G.D., Konicek, L., 1975, "Correlation Equations for Free Convection Heat Transfer in Horizontal Layers of Air and Water," *International Journal of Heat & Mass Transfer,* Vol. 18, pp. 879-884.

Hunter, J., Collins, M.W., 1987, "Holographic Interferometry and Digital Fringe Processing," *Journal of Physics,* vol. 20, pp. 683-691.

Hunter J. & Collins, M.W., 1986, "Problems in using Holographic Interferometry to Resolve the Four-Dimensional Character of Turbulence. Part II: Image and Data Processing," *Journal of Optical Sensors*, vol. 1, no.3, pp. 277-234.

Jin, H., 2000, "Flow Visualization of Natural Convection in a Vertical Cavity," M.A.Sc. Thesis. University of Waterloo, Waterloo, Ontario, Canada.

Ju, Seong, Hun, Hee Cheon No, Franz Mayinger, 2000, "Measurement of Heat Transfer Coefficients for Direct Contact Condensation in Core Makeup Tanks using Holographic Interferometer," *Nuclear Engineering and Design,* vol. 199, pp. 75–83.

Kline, S.J., McClintock, F.A., 1953, "Describing Experimental Uncertainties in Single-Sample Experiments," *Mechanical Engineering*, vol. 75, pp. 3 -8.

Korpela, S. A., Lee, Y., Drummond, J. E., 1982, "Heat Transfer Through a Double Pane Window," *Journal of Heat Transfer,* vol. 104, pp. 539-544.

Kovalev, P.I., Komissaruk, V.A., Mende, N.P., June 1983, "A System Combining Several Interferometers to Investigate Spatial Gas-Dynamic Phenomena and High-Speed Photography of Axisymmetric Processes," *Optics & Laser Technology*, pp. 141-144.

Kuehn, T.H., Goldstein, R.J., 1978, "An Experimental Study of Natural Convection Heat Transfer in Concentric and Eccentric Horizontal Annuli," *Journal of Heat Transfer*, vol. 100, pp. 635-640.

Lee, Y., Korpela, S., 1983, "Multicellular Natural Convection in a Vertical Slot", *Journal of Fluid Mechanics*, vol. 126, pp. 91-121.

Lewis, RW, Morgan, K, Thomas, H.R, Seetharamu, K.N., 1996, *The Finite Element Method in Heat Transfer Analysis*, John Wiley & Sons Ltd., New York.

Liou, T.M., Hwang, J.H. Chen, S.H., 1993, "Simulation and Measurement of Enhanced Turbulent Heat Transfer in a Channel with Periodic Ribs on one Principal Wall," *International Journal of heat and mass transfer*, vol. 36, no.2.

Liu, D., Feng, H., 2006, "In-Cylinder Temperature Field Measurement with Laser Shearing Interferometry for Spark Ignition Engines," *Optics and Lasers in Engineering*, vol. 44, pp. 1258-1269.

Lockett, J.F., Collins, M.W., 1986a, "Problems in using Holographic Interferometry to Resolve the Four-Dimensional Character of Turbulence. Part I: Theory and Experiment", *Journal of Optical Sensors*, vol. 1, no. 3, pp. 211-224.

Lockett, J.F., Collins, M.W., 1986b. "Holographic Interferometry and its Application to Turbulent Convective Heat Transfer", *Journal of Optical Sensors*, vol. 1, no. 3, pp. 191-208.

Lockett, J.F., Hunter, J.C., Voke, P.R., Collins, M.W., 1985, "Investigation of Convective Heat Transfer Enhancement using Real Time Holographic Interferometry," *Optical Measurements in Fluid Mechanics,* pp. 129-134.

Lucic, A., Emans, M., Mayinger, F., Zenger, C., 2004, "Interferometric and Numerical Study of the Temperature Field in the Boundary Layer and Heat Transfer in Sub Cooled Flow Boiling," *International Journal of Heat and Fluid Flow*, vol. 25, pp. 180–195.

Machin, A.D., 1997, "An Experimental Study of Free Convective Heat Transfer from a Vertical Flat Plate in the Presence of Louvers," M. A. Sc. Thesis, University of Western, Ontario, Canada.

Machin, A. D., Naylor, D., Harrison, S. J., Oosthuizen, P. H., 1998, "Experimental Study of Free Convection at an Indoor Glazing Surface with a Venetian Blind," *HVAC and Research,* vol. 4, no. 2, pp. 153-166.

Naylor, D., Tarasuk, J.D., 1993, "Digital Image Processing of Interferograms for Local Convective Heat Transfer Measurements", *Experimental Heat Transfer, Fluid Mechanics and Thermodynamics*, pp. 1609-1614.

Naylor, D., Duarte, N., 1999, "Direct Temperature Gradient Measurement Using Interferometry," *Experimental Heat Transfer*, vol.12, pp. 279- 294.

Naylor, D., Machin, A. D., 2001, "The Accuracy of Beam-Averaged Interferometric Temperature Measurements in a Three-Dimensional Field," *Experimental Heat Transfer*, Vol. 14, pp. 217–228.

Naylor, D., 2003, "Recent Developments in the Measurement of Convective Heat Transfer Rates by Laser Interferometry," *International Journal of Heat and Fluid Flow*, vol.24, pp. 345–355.

Naylor, D., 2008, "Laser Interferometry," chapter in the book *Heat Flux Measurement*, Developments in Heat Transfer Series, vol.12, Wessex Institute of Technology Press.

Nobis, D., Vest, C. M., 15 July 1978, "Statistical Analysis of Errors in Holographic Interferometry", *Applied Optics,* vol. 17, no. 14, pp. 2198-2205.

Nugent, K.A., 15 September 1985, "Interferogram Analysis using an Accurate Fully Automatic Algorithm", *Applied Optics*, vol. 24, no. 18, pp. 3101-3105.

Poulad, M.E., Naylor, D., 2009, "Measurement of Time-Averaged Turbulent Free Convective Heat Transfer in a Tall Vertical Cavity using Laser Interferometry," *Proceedings. CANCAM Conference*, Halifax, Canada.

Posner, J.D., 2001, "Resonant and Nonresonant Holographic Interferometry in Axisymmetric Flames," Ph.D Thesis. University of California. Irvine. USA.

Robinson, D.W., Reid, G.T., 1993, *Interferogram Analysis, Digital Fringe Pattern Measurement Techniques,* IOP Publishing Ltd.

Raithby, G.D., Hollands, K.G.T., Unny, T.E., 1977, "Analysis of Heat Transfer by Natural Convection Across Vertical Fluid Layers", *Journal of Heat Transfer*, vol. 99, pp. 287-293.

Riley, WF., Dally, LW., 1969, "Recording Dynamic Fringe Patterns with a Granz-Schardin Camera," *Exp. Mech.,* vol. 8, pp. 27-33.

Schemm, J.B., Vest, C.M., 15 September 1983, "Fringe Pattern Recognition and Interpolation using Nonlinear Regression Analysis", *Applied Optics*, vol. 22, no. 18, pp. 2850-53.

Shewen, E.C., 1986, "A Peltier Effect Technique for Natural Convection Heat Flux Measurement Applied to the Rectangular Open Cavity," Ph.D. thesis, University of Waterloo, Waterloo, Canada.

Shewen, E.C., Holland, K.G.T., Raithby, G.D., Nov.1996, "Heat Transfer by Natural Convection Across a Vertical Air Cavity of Large Aspect Ratio," *Journal of heat transfer*, vol. 118, pp. 993-995.

Singh, S. K., Panigrahi, P. K. Muralidhar, K., 2007, "Effect of Buoyancy on the Wakes of Circular and Square Cylinders: a Schlieren-Interferometric Study," *Exp Fluids,* vol. 43, pp. 101–123.

Slepicka, James S., Cha, Soyoung S., August 1995, "Stabilized Nonlinear Regression for Interferogram Analysis," *Applied Optics*, vol. 34, no. 23.

Snyder, J.J., 15 April 1980, "Algorithm for Fast Digital Analysis of Interference Fringes," *Applied Optics*, vol. 19, no 8, pp. 1223-1225.

Sun, C., Chen, J., Lu, H., June 2008, "Improved Phase-Shifted Digital Speckle Shearography for Time-Dependent Deformation Measurement," *Optical Engineering*, vol. 47, no. 6.

Tarasuk, J.D., 1968, "The Theory, Design and Operation of the University of Saskatchewan 8-inch Mirror Mach-Zehnder Interferometer," *Technical Report C-3,* Mechanical Engineering Department, University of Saskatchewen.

Taylor, B.N., Kuyatt, E., 1994, "Guidelines for Evaluating and Expressing the Uncertainty of NIST Measurement Results," *United States Department of Commerce Technology Administration, National Institute of Standards and Technology.*

Trias, F., Xsori, A., M., Oliva, AREZ-SEGARRA., C. D. PE´, 2007, "Direct Numerical Simulations of Two- and Three-Dimensional Turbulent Natural Convection Flows in a Differentially Heated Cavity of Aspect Ratio 4," *Journal of Fluid Mechanics*, vol. 586, pp. 259–293.

Touloukian, Y.S., Makita, T., 1975, "Specific Heat: Nonmetallic Liquids and Gases, Thermophysical Properties of Matter," vol 6, *Thermophysical Properties Research Center (TPRC).* Purdue University, Plenum Publishing Corp.

Wright, J. L., 1996, "A Correlation to Quantify Convective Heat Transfer between Vertical Window Glazings," *ASHRAE Trans*, vol. 102/1, pp. 940-946.

Wright, J.L., Jin, H., Hollands, K.G.T., Naylor, D., 2006, "Flow Visualization of Natural Convection in a Tall, Air-Filled Vertical Cavity," *International Journal of Heat and Mass Transfer,* vol. 49, pp. 889–904.

Wright, M. P., June 1975, "Study of Shockwave Propagation in a Metal bar by High-Speed Interferometry," *Optics and Laser Technology*, pp. 113-115.

Yatagai, T., Nakadate, S., Idesawa, M., Saito, H., May/June 1982, "Automatic Fringe Analysis using Digital Image Processing Techniques", *Optical Engineering*, vol. 21, no. 3, pp. 432-435.